New Approaches to Machine Vision Based Displacement Analysis

Doctoral Thesis

Richard Neumayr

Institute for Automation
Department Product Engineering
Montanuniversitaet Leoben
Leoben, Austria

2011

Supervisors:

O.Univ.-Prof. Dipl.-Ing. Dr.techn. Paul O` Leary B.A., B.A.I., M.E.E.
Institute for Automation, Montanuniversitaet Leoben, Austria

Prof. Paul J. Zsombor-Murray B.Eng., M.Eng., Ph.D., ing., FCSME
Centre of Intelligent Machines, McGill University, Montréal, Canada

I declare in lieu of oath, that I wrote this thesis and performed the associated research myself, using only literature cited in this volume.

Leoben, 2011 Richard Neumayr

In remembrance to my father.

Acknowledgements

First of all I would like to thank Paul O'Leary for the inestimable support during the last years, for the possibility to compose this thesis at the Institute for Automation, and for the fruitful discussions regarding the thesis. I appreciate his critical and supporting comments on this work

Many thanks go also to my co-examiner Paul Zsombor-Murray for his valuable comments and the support which helped a lot to finish this thesis.

During the past years my colleagues at the Institute for Automation have been a great support. Many thanks to Matthew Harker, Amir Badshah, Gerold Probst, Gerhard Rath, Beate Oswald-Tranta, Mario Sorger and last but not least, our secretary Doris Widek who has "saved" my life on numerous occasions.

My Acknowledgements go to GEODATA GmbH who initiated and supported this project. My thanks to Johann Golser.

I would like to thank all my friends, near and far, for their assistance and the all-important non-technical aspects of being a Ph.D. candidate.

I would like to express my gratitude to Eva, the sunshine of my life. I want to thank her for her great mental support and for the trust she places in me.

Finally, I want to express my deepest gratitude to my family. I am thankful to my parents and my brother for their steadfast support and their understanding.

Abstract

This thesis describes new approaches to machine vision based measurement and displacement analysis. It deals with the design and manufacturing of optical components; calibration and evaluation procedures; together with thermally stable housings. All these elements are required for the implementation of accurate optical displacement and orientation sensors.
Printed hexagonal and rectangular dot-patterns on optical glass are investigated with respect to their spatial scattering properties of an incident laser beam, and as a means of implementing semi-transparent windows to image laser spots on two parallel targets. The positions of the laser spots are observed by two cameras. The mapping from pixel coordinates to real world coordinates is implemented via a bivariate tensor polynomial product, whereby the calibration coefficients are determined in a manner such that the distortion associated with the optical component, e.g., lens distortion is compensated. The covariance propagation is explicitly computed for the calibration process and used to optimize the selection of the polynomial degree. This reflects the trade-off minimizing between the systematic and stochastic error.
Two applications that incorporate the results of the theoretical approach are presented: (1) The new technique and methods are demonstrated in the design of and implementation of an active optical laser target for machine guidance control. The unit measures the orientation and position of the machine using an off-vehicle reference laser beam that is projecting its laser spots on two parallel targets. Precise measurements of the spot positions are achieved, yielding a standard deviation of the displacement error of 0.05 [mm] and for yaw and pitch of 0.02 [degree]. (2) The second measurement system is a single, stationary camera setup for direct full pose determination of parallel manipulators. Light Emitting Diodes (LED) mounted on the End Effector are registered in the image to compute the mapping and the displacements. Poses could be quickly registered at sub-millimetre precision. This method simplifies the kinematic calibration structure of parallel manipulators considerably.
Finally, a new viable component called electro-active glass – glass that exhibits selective reflection/transmission properties – is investigated as regards its potential as a laser reference spot target for precision camera based metrology.

Kurzfassung

Diese Arbeit präsentiert neue Verfahrens- und Lösungsansätze in der optischen Messtechnik zur Bestimmung von Orientierung und Position von Objekten. Sie befasst sich mit der Entwicklung, Bewertung und Herstellung von optischen Komponenten und deren Kalibrierung zur Umsetzung und Auslegung von hochgenauen, optischen Orientierungs- und Positionssensoren.
Optische Glasplatten (Zieltafeln), bedruckt mit einem hexagonalen oder orthogonalen Punktemuster, wurden auf ihre räumlichen Streueigenschaften bei einem einfallenden Laserstrahl untersucht. Die dadurch erzielte Halb-Transparenz ermöglicht das Abbilden von zwei Laserpunkten auf zwei zueinander parallelen Zieltafeln. Die Positionen der Laserpunkte werden mit zwei Kameras aufgenommen. Die Transformation von Pixel- auf metrische Koordinaten wird mithilfe von bivariaten Tensor-Polynomen berechnet, wobei die Polynom-Koeffizienten so ermittelt werden, dass die mit den optischen Komponenten verbundenen Verzerrungen, z.B. Linsenfehler, kompensiert werden. Die Kovarianz-Fortpflanzung wird explizit für die Kalibrierung errechnet, um den optimalen Polynomgrad für die Approximierung zu bestimmen. Dieses Verfahren minimiert somit die Diskrepanz zwischen systematischen und stochastischen Fehlern.
Diese neue Methode wurde in zwei Anwendungen implementiert: (1) Die System-Kalibrierung wurde bei der Entwicklung eines optischen Messinstruments zur Bestimmung von Orientierung und Position von Tunnelbohrmaschinen angewendet. Ein Referenz-Laserstrahl, gerichtet auf dieses Messinstrument, trifft auf zwei zueinander parallele Zieltafeln auf, wobei die erste Zieltafel halbdurchlässig ist. Das implementierte Verfahren liefert sehr präzise Messungen von den Positionen der Laserpunkte mit einer Standardabweichung von 0.05 [mm] bzw. einer Standardabweichung von 0.02 [Grad] bei Neigungs- und Gierwinkel. (2) Das zweite Messsystem besteht aus einer digitalen, stationären Kamera, welche die Orientierung und Position des Endeffektors von planaren parallelen Manipulatoren bestimmt. Leuchtdioden am Endeffektor werden im Bild registriert, um die Transformation zu berechnen. Die Messergebnisse zeigen, dass Position und Orientierung des Manipulators schnell, einfach und mit sub-millimeter Genauigkeit gemessen werden können.
Schließlich wird der Einsatz einer neuen Komponente von Glasfenstern mit schaltbarer Transparenz - Glas, das durch elektrische Spannung von durchsichtig zu komplett lichtundurchlässig geschaltet werden kann - als mögliche Verwendung für Zieltafeln in der metrischen Bildverarbeitung untersucht.

Table of Contents

List of Figures

List of Tables

Chapter 1

Introduction

The first introductory part of this thesis describes the implementation, configuration and calibration of vision based measurement systems to enable accurate motion analysis in mechanical systems. Such vision based measurement systems have been successfully employed in robotics to perform accurate pose analysis for robot calibration [8]. A detailed introduction to this research field is found in Chapter 2.4 where a new vision based pose measurement technique is presented and tested on the Planar Double Triangular Parallel Manipulator. A homography [17] method based on the camera pinhole model is used to map the pixel coordinates to real world coordinates. In such approaches the accuracy of the measurement system is limited by the accuracy of the individual optical components. In particular the distortion associated with a real lens has had a dominant effect on the obtainable accuracy. The compensation of such distortion effects is dealt in the second part.
The second and main part deals with the design and production of optical components; calibration and evaluation procedures; together with thermally stable housings as required for the implementation of accurate optical displacement and orientation sensors. Such measurement devices are found in many applications, e.g.,: alignment of large magnets [1]; shooting range simulation [2], position of machines [5]. Whereby, different implementation concepts have been followed: retroflector based [3]; position sensitive detectors, most commonly used in "laser beam riding" [4]; camera imaging systems [5].
The components and methods presented in this part are aimed at implementing devices, which can be used for the guidance of tunneling and mining machines, that require robust systems since they are applied in very harsh environments. The implementation investigated in this paper is based on imaging of a laser point on two parallel targets whereby the first target is a semi-reflective window. Different printing techniques and dot-patterns are investigated for the implementation of semi-transparent targets. The different printing techniques are compared with respect to their mechanical robustness and the different dot-pattern are examined with respect to their statistical scattering of the laser beam. Carbon fibre plates have been used to to construct the inner housing. This ensures a thermally stable baseline, while being light weight and strong.
A significant contribution of this paper lies in a new mathematical approach to calibration and measurement computation. A complete system input to output calibration is performed, whereby the coordinate field is modelled by a bivariate tensor polynomial. In

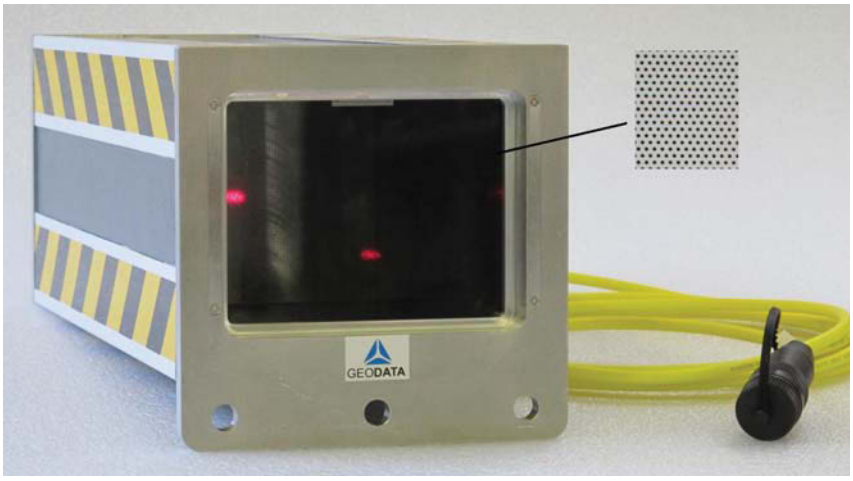

Fig. 1.1: A prototype Active Laser Target. This device was designed for the guidance of tunneling machines. Upper-right: Enlarged dot-pattern on semi-transparent target. (Photograph by Geodata GmbH [11]).

this manner systematic errors in the optics, e.g., fisheye distortion of short focal length lenses, and mechanical construction are compensated to enable the design of compact vision based measurement systems without compromising accuracy. The tensor polynomial approach also enables the computation of covariance propagation. This feature is used to optimize the trade-off between systematic and statistical errors in parameterizing the system. The covariance propagation analysis is verified by Monte Carlo simulation.
The new technique and methods are demonstrated in the implementation of an active optical laser target (ALT), Fig. 1.1, for machine guidance. Extensive experimental testing of the procedure is presented that verifies the performance predicted in the design procedure.
Based on this measurement concept a recently available product called "electro-active glass" – glass that exhibits selective reflection/transmission properties – is investigated as regards its potential as a laser reference spot target for precision camera based metrology. This configuration allows placement of several targets in a row to measure displacements at different locations with respect to a reference beam. Such systems can be an alternative to plumb line systems [16] to monitor, e.g., creeping rock-movements in mine surveying.
The main contributions of this research work are:

1. Formulation of a new efficient mathematical coordinate transformation approach called bivariate polynomial tensor approximation to model nonlinearities of lenses with optical error, e.g., lenses with short focal length;

2. Verification and evaluation of this approach via covariance propagation to optimize the trade-off between systematic and statistical errors of the system finding an optimal parameterization. Verification of covariance propagation analysis with Monte Carlo simulation.

3. Investigation, evaluation and calibration of suitable optical components to design a

compact, vision based measurement system that is applied to develop a prototype of an active laser target measurement instrument for machine guidance control;

4. Presentation of new means to manufacture semi-reflective targets with optimal relection/transmission properties by printing dot-patterns on optical quality glass using screen printing technology. Evaluation of the dot-pattern with respect to its statistical scattering of the laser beam.

5. A complete input to output system calibration of the ALT whereby the coordinate field is modelled by bivariate polynomial tensor approximation that compensates optical errors and systematic errors in mechanical construction; measurement results regarding reproducibility and accuracy of pitch and yaw angle;

6. Prognosis regarding the application of this measurement method in mine surveying introducing "electro-active glass" targets to measure and monitor creeping rock-movements in mining tunnels as an alternative to plumb line measurement systems [16].

This thesis is divided into two parts:

Part I
In Part I the reader is introduced to the principle of operation of vision based measurement systems with their associated problems. It is an introductory overview of vision based displacement measurement taking as an example vision based pose measurement in robotics that is part of the author's earlier research. In this section the following topics and procedural steps are covered:

1. Principle of operation of vision based measurement systems with their associated problems;

2. Various image processing techniques to detect geometric objects in an image using, e.g., Grassmanian manifolds for direct estimation;

3. Workspace analysis of the manipulator employing kinematic mapping to set up a suitable vision measurement system and the required optical components to achieve the desired measurement accuracy;

4. Suitable calibration objects with a marker setup that can be easily detected with the aforementioned image processing techniques. In this application Light Emitting Diodes (LEDs) are used as markers;

5. Camera calibration with lenses of high quality and negligible distortion;

6. Homography computation that assigns pixel coordinates to real world coordinates;

7. Implementation, configuration and calibration of a vision based measurement systems to measure the full pose of the a planar parallel manipulator for robot calibration.

8. Test results of pose measurements and conclusion.

This knowledge and experience is applied to develop and to design a prototype of the previously mentioned measurement unit to perform accurate orientation and position analysis of a tunnel boring machine.

Part II
The second part of this thesis deals with the product development of an optical active laser target measurement unit addressing the main contributions mentioned above and the following procedural steps and technical issues:

1. Specification and requirement analysis, state of the art;
2. Develop a concept and choose the most suitable;
3. Patents research;
4. Applying the methods in Part I to strengthen and verify the concept at first stage and identify the technical risks in the development with a "proof of concept" laboratory experiment;
5. Initiate a feasibility study to evaluate the specified requirements, measurement accuracy, optical components, image processing algorithms and calibration procedure. Improve the laboratory setup.
6. Initiate components research and their technical manufacturability and availability;
7. Formulating a new mathematical approach called bivariate polynomial tensor approximation to compensate optical errors of, e.g., lenses with short focal length;
8. Optimization: Using optics, i.e., lenses with small focal length (micro-lenses) to achieve compact vibration tolerant unit;
9. A complete system calibration and test results of measurements with laboratory setup and prototype;
10. Prognosis regarding the use of "electro-active glass" (AG) as target component to monitor creeping rock-movements in mining tunnels (mine surveying);

Part I

Chapter 2

Vision Based Pose Measurement in Robotics

This chapter describes the development and implementation of a vision based measurement system for planar displacements. It is applied to measure the pose of planar parallel manipulators to enable accurate robot calibration. The design and workspace of the Planar Double Triangular Manipulator (PDTPM) and the steps required to set up a vision based, single camera measurement system are drawn from two of the author's papers.
First of all an introductory overview of vision based measurement is given describing the principle of operation and the associated problems of such systems followed by various image processing techniques presenting mathematical methods on detecting geometric objects in an image. Evaluation of the test results obtained by the implemented techniques are presented at the end of this chapter.

2.1 Principle of Operation

Metric vision comprises the optical measurement of size, shape, position and orientation of geometric objects by means of digital image processing. The principle of operation of metric vision systems is shown in Fig. 2.1.

1. The **Optical Arrangement** provides the basis to create an image of the measurement scene. It is determined by the setup of the optical components (filters, lenses, light sources, etc.) and the cameras with respect to the measured object.

2. **Image Acquisition**: The view provided by the optical setup is projected on a camera chip where the light intensity is transduced to an electric signal yielding a digitized image. The primary measurement errors originate in this process. Vibrations, lens distortion, spatial quantization on the pixel grid of the camera chip and the noise and quantization of the pixel intensity are error sources to be considered.

3. **Feature Extraction and Segmentation**: In order to measure dimensions in an image points of interest from the digitized images have to be extracted. These points

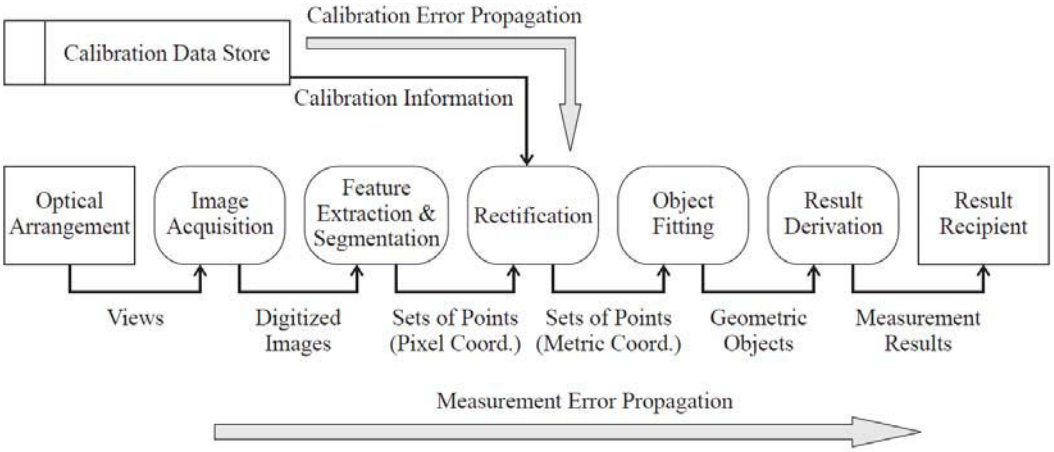

Fig. 2.1: Principle of operation of a metric vision system [30], the grey-shaded arrows indicate the propagation of measurement and calibration errors.

describe, e.g., edges of objects, contours of measurement marks or some other features in the image. Note that the point coordinates are perturbed with noise, since the imaging and acquisition errors are propagated to the extracted points. Various image processing techniques for feature extraction and segmentation are described in the following sections.

4. **Rectification**: In order to assign pixel coordinates to metric coordinates some calibration information is needed. This information could be a simple scaling factor, however, in most applications objects are measured in a projective view, i.e., a collineation between the projective image plane and the required metric coordinate plane need to be derived, e.g., homography computation [17]. A calibration object with a precisely pre-determined marker pattern is commonly used to perform camera calibration.

5. **Object Fitting**: The point sets are abstracted by geometric objects such as lines, circles, general conics, polynomial curves, splines, etc. A geometric object is represented by a set of parameters. These parameters are estimated by minimization of an error function, which may either be based on the algebraic expression of the object or on the geometric distances of the points to the object. The uncertainty in the fit results is influenced by both the error of the input points and the applied fitting algorithm.

From the principle of operation one can conclude two principal types of error associated with a metric vision system [30]:

1. Calibration errors: Inaccurate calibration of the optical components is a systematic deviation and thus leads to a bias in the measurement result. Consequently in most applications high quality components are used to suppress these errors as com-

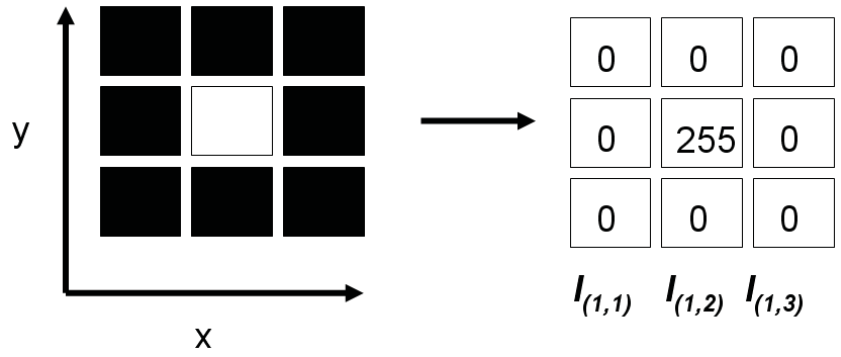

Fig. 2.2: Example of an image of 3×3 [pix] and corresponding 8-bit grey level matrix.

pensation algorithms with image processing techniques are difficult to parameterize [9].

2. Errors in a single measurement: These errors originate in the image acquisition process and are propagated through the measurement and analysis chain.

The work herein focuses mainly on the calibration errors and presents a general mathematical method to model nonlinear optical errors and to perform accurate calibration and mapping.

2.1.1 Image Acquisition and Processing

A matrix is the most common data structure for image representation. Each element entry denotes a certain intensity value $I_{(x,y)}$ of the corresponding pixel of the sampling grid. The matrix size equals the resolution of the image. In this work 8-bit grey-level images are processed, see Fig. 2.2.

Thresholding

The basic process of binarizing a grey level image is described by

$$B_{(x,y)} = \begin{cases} 0, & \text{if } I_{(x,y)} < t \\ 1, & \text{if } I_{(x,y)} > t \end{cases} \tag{2.1}$$

The result is a black and white (binary) image. This method simplifies the image and enables the use of binary morphology. Besides this, stray light effects can be filtered. Finding a suitable threshold t to binarize is one of the major difficulties. The thresholds tend to change with different illumination and from image scene to scene. In general the methods can be grouped into two classes:

1. Global thresholds valid for the complete image.

2. Local thresholds determined from local features.

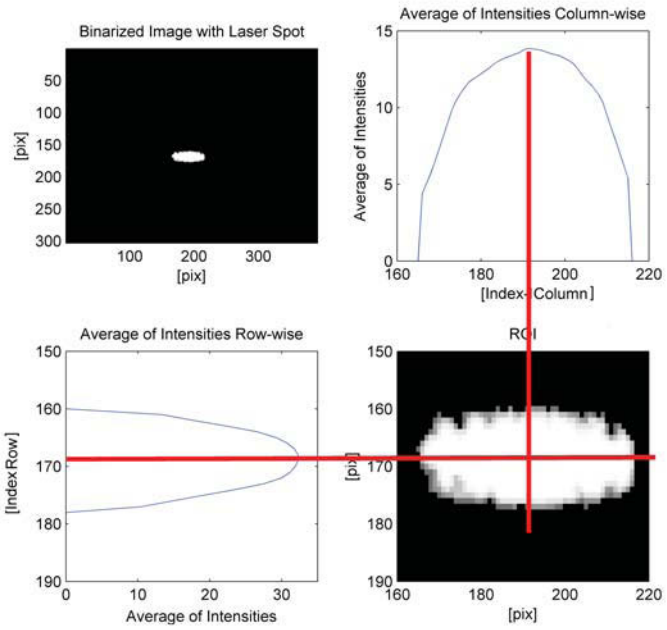

Fig. 2.3: ROI determination, average of intensities. Upper-left: Binarized image of a laser spot on a target. Upper-right: Average of intensities of image column-wise. Bottom-left: Average of intensities of image row-wise. Bottom-right: Extracted ROI window.

The global task is to find a suitable level for t which is valid for the whole image. Methods to compute an optimal threshold are described in [23]. In that work the threshold was set manually as the images were of high quality and taken with an optical band-pass filter that blocked stray ambient.

Region of Interest - Classification

In most cases it is of interest to process only a sub-region of an image, ignoring the other regions,

1. to extract features;
2. to save computation time.

This is commonly referred to as region of interest (ROI) processing. Looking at Fig. 2.3 the region of interest describes the surrounding neighborhood of the laser spot. The ROI can be set manually or feature based:

1. If the object in the image is dominant the average of intensities method will give the approximate position of the ROI-window, see Fig. 2.3.
2. If there are several objects in the image having the same features, e.g., same intensity, a contour algorithm [23] combined with a classification process that, e.g., checks the size or shape of the found contours, will extract the desired object, see Fig. 2.4.

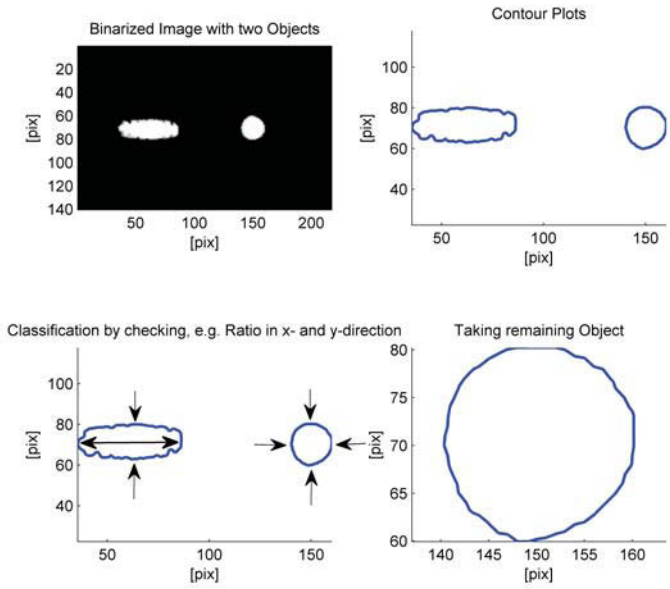

Fig. 2.4: ROI determination, contour classification. Upper-left: Binarized image of two different laser spots on a target. Upper-right: Extracted contours. Bottom-left: Classify contours by their ratio in x and y-directions. Bottom-right: Extracted classified contour.

2.1.2 Feature Extraction and Fitting

Grassmanian Manifolds for Direct Estimation

Grassmanian manifolds describe geometric objects in terms of linear homogeneous equations. Given a distorted data set the object can be estimated by reducing it to a linear least square problem. Such "fittings" are useful to, e.g., track an object in an image, derive the dimensions of an object or simply calibrate data. The method used in this work to fit geometric objects in an image is based on [24].
A geometric object can be defined by the homogeneous implicit equation, such as a conic

$$ax^2 + bxy + cy^2 + dxw + eyw + fw^2 = 0, \tag{2.2}$$

where w is the homogenizing coordinate with $w = 1$ for points in Euclidean space. Given a mean-free data set of points (x_i, y_i) the algebraic distance from a point to the geometric object e_i can be defined

$$e_i \triangleq ax_i^2 + bx_iy_i + cy_i^2 + dx_i + ey_i + f, \tag{2.3}$$

or in matrix form

$$\left[\begin{array}{ccc|cc|c} x_i^2 & y_i^2 & x_iy_i & x_i & y_i & 1 \\ \vdots & \vdots & \vdots & \vdots & \vdots & \vdots \\ x_n^2 & y_n^2 & x_ny_n & x_n & y_n & 1 \end{array}\right] \left[\begin{array}{c} a \\ b \\ c \\ \hline d \\ e \\ \hline f \end{array}\right] = \left[\begin{array}{c} e_1 \\ \vdots \\ e_n \end{array}\right] = \mathsf{D}\boldsymbol{z} \tag{2.4}$$

where w=1, $\boldsymbol{z}$ contains the conic coefficients and D provides the design matrix. The design matrix and coefficient vector can be partitioned into groupings of their quadratic, linear and constant terms, i.e.,

$$\mathsf{D}_2 = \left[\begin{array}{ccc} x_i^2 & y_i^2 & x_iy_i \\ \vdots & \vdots & \vdots \\ x_n^2 & y_n^2 & x_ny_n \end{array}\right], \quad \mathsf{D}_1 = \left[\begin{array}{cc} x_i & y_i \\ \vdots & \vdots \\ x_n & y_n \end{array}\right], \quad \mathsf{D}_0 = \left[\begin{array}{c} 1 \\ \vdots \\ 1 \end{array}\right], \tag{2.5}$$

and therefore

$$\boldsymbol{z}_2 = \left[\begin{array}{c} a \\ b \\ c \end{array}\right], \quad \boldsymbol{z}_1 = \left[\begin{array}{c} d \\ e \end{array}\right], \quad z_0 = f \tag{2.6}$$

The reason behind this partitioning is the fact that the column of ones is statistically invariant, the statistical nature of the quadratic data is different to that of the linear data. Furthermore the imposed constraints $C_1 : b^2 - 4ac = \alpha$ and $C_2 : a^2 + b^2 + c^2 = 1$ apply only to the quadratic data [24]. The algorithm to solve for the conic coefficients in $\boldsymbol{z}_i$ is described in [24] were an orthogonal residualization process is applied to the design matrix D. In that work flat-headed LEDs, see Fig. 2.5, upper left, are used as markers to be detected in the image. Therefore ellipses are expected to provide the best fit.

First Order Moment Computation

Another accurate and robust method to localize objects of arbitrary contour is the calculation of the first order moment of intensities of the object that is defined as follows

$$\boldsymbol{x} = \left[\begin{array}{c} \frac{\sum_{(x,y)\epsilon\Omega} xI^p(x,y)}{\sum_{(x,y)\epsilon\Omega} I^p(x,y)}, \frac{\sum_{(x,y)\epsilon\Omega} yI^p(x,y)}{\sum_{(x,y)\epsilon\Omega} I^p(x,y)} \end{array}\right] \tag{2.7}$$

The variable Ω describes the size of a tile with its intensity entries $I(x, y)$ containing the pixels that are associated with the object to be localized and p is a power factor to emphasize ($p > 1$) bright pixels. The definition of the weighted center of intensities $\boldsymbol{x} = [x_s, y_s]$ represents therefore a unique invariant reference point to describe the position of an extracted object.

Looking at Eq. 2.7, it is obvious that the result of the first order moment calculation is significantly dependent on the choice of the tile size. To achieve accurate results some a-priori knowledge about the object is very helpful such as its expected size and contour.

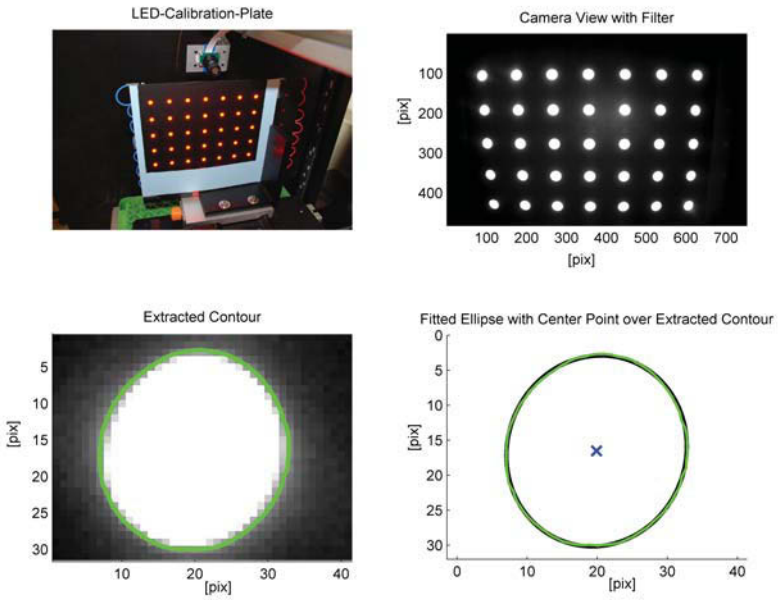

Fig. 2.5: Geometric fitting via linear least squares employing Grassmanian manifolds. The contour of the LED is extracted and fitted with an ellipse.

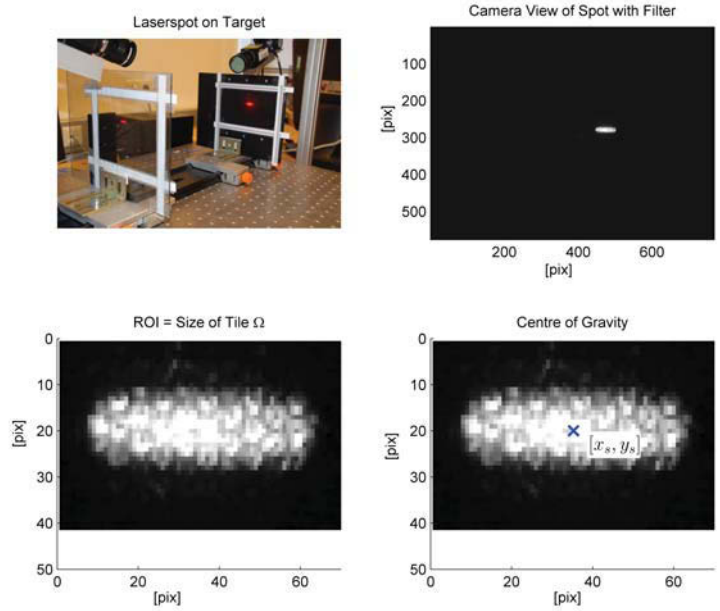

Fig. 2.6: First moment computation of intensities.

2.2 Relevant Papers

In the next sections two of the author's papers, that cover the following topics in vision based pose measurement in robotics, are cited:

1. Workspace and singularity analysis of the planar double triangular parallel manipulator using kinematic mapping [36]. This paper describes the workspace analysis of the PDTPM employing kinematic mapping to set up a suitable vision measurement system and the required optical components to achieve the desired measurement accuracy;

2. Precise pose measurement with single camera calibration for planar parallel manipulators [33]. This paper covers the following relevant topics as mentioned in the introduction of this chapter:

    - Suitable calibration objects;
    - Camera calibration with lenses of high quality and small distortion;
    - Homography computation, rectification;
    - Test results of the pose measurements of the PDTPM.

2.3 Workspace and Singularity Analysis of the Planar Double Triangular Parallel Manipulator Using Kinematic Mapping

Richard Neumayr, Paul Zsombor-Murray[2]

Abstract [1]

Planar kinematic mapping yields an elegant and compact general symbolic univariate polynomial solution to determine the reachable workspace for three legged, three degree of freedom planar parallel manipulators. This paper investigates the algebraic nature of the singularity surfaces of the Planar Double Triangular Parallel Manipulator (PDTPM), a compact design representative of a *PRP* mechanism. The kinematic image of the workspace represents a solid region bounded by the intersection of minimum and maximum joint input singularity surfaces. An important characteristic of these singularity surfaces in the kinematic image space implies that if a solid region can be defined in the workspace of the mechanism such that its faces, edges, and vertices do not contain a singular pose, then there are no singularities inside this solid region. It is believed that this a very useful result considering the design and the kinematic synthesis of such mechanisms.

2.3.1 Introduction

Parallel mechanisms have been successfully employed in numerous industrial applications over the last decades. The advantages are obvious as the end effector of these mechanisms is connected with several kinematic chains to their base and therefore can bear higher loads, at higher speed and often with a higher repeatability [1, 2] compared to serial mechanisms. Such robots can be found in high-speed pick and place operations, flight simulators and machine tools.
However, one of the drawbacks of parallel manipulators is their relatively small workspace. Therefore a careful study of the workspace is very useful to find the optimum design parameters for the manipulator. In this paper kinematic mapping is used to analyze the reachable workspace of the Planar Double Triangular Parallel Manipulator (PDTPM) a compact design representative of *PRP* mechanisms with virtually zero-length legs.

[2]Paul Zsombor-Murray is with McGill University, Centre for Intelligent Machines, Montréal, Canada.

[1]This paper originally appeared as: R. Neumayr, P. J. Zsombor-Murray, "Workspace and singularity analysis of the planar double triangular parallel manipulator using kinematic mapping", Unpublished Manuscript, Institute for Automation, Montanuniversität Leoben, Austria, 2011.

Algebraic methods have been employed successfully to solve problems in mechanism analysis and synthesis mainly because of the advances in solving systems of polynomial equations in combination with the currently available computer power. Nevertheless in mechanism synthesis it is important to find the simplest mathematical model to save computing time [3]. Therefore Husty [3] re-introduced an efficient geometric formulation with equations in terms of variables in the kinematic image space. This method has been originally introduced by [4] and [5] in the early 20th century. A very detailed description may be found in [6].
Based on the work in [7, 8, 9] a method was developed wherein all possible End Effector (EE) positions are defined by surfaces bounding a solid region in the kinematic image space. It is believed that this approach provides a useful design tool because it conveniently defines the reachable workspace. Therefore the mapping of planar displacements to points in this special 3D projective space are introduced in this work. Although the workspace analysis of planar three-legged manipulators is well established [2, 10] it is emphasized here that kinematic mapping is a useful, elegant alternative approach to determine singularity-free zones in the workspace to optimize the design and the kinematic synthesis of manipulators.

2.3.2 Design of the PDPTM

Design and development of the PDPTM were first described by [11]. To overcome the undesired flexibility in long legged platforms, Daniali [11] introduced a novel parallel architecture referred to as double-triangular; consisting of a fixed (FF) and movable (EE) triangle. FF represents fixed frame while EE represents end effector or moving frame. An actuated prismatic or P-joint moves a combination of a passive revolute, R-joint and another, passive, P-joint along each of the fixed triangle sides, thus creating a peculiar three-legged $\underline{P}RP$ planar parallel manipulator (3 DOF) with legs of, effectively, zero length. Its compact architecture is very practical for any applications where space is limited. A prototype was built by [12, 13, 14].

Fixed Triangle – Each leg of the fixed triangle is a recirculating ball screw assembly driven by a stepper motor, all mounted on an aluminum channel as shown in Fig. 2.7. Each leg assembly may be moved independently of the other two legs of the fixed triangle.

Moving Triangle – The three edges of the movable triangle are made of steel rails designed to mount a ball trolley, like a linear bearing that runs on a rail as shown in Fig. 2.7. In operation the three rails are fixed relative to each other. However the vertices can be adjusted to allow the three angles and lengths of the moving triangle to be changed. Hence various moving triangle architectures may be tried out.

***PRP*-Joints** The linear bearing on a rail of the movable triangle is joined to the corresponding ball screw nut of the fixed triangle through a revolute joint formed using a pair of angular contact bearings.

Referring to [11] an isotropic design, i.e., one which enjoys a higher degree of manipula-

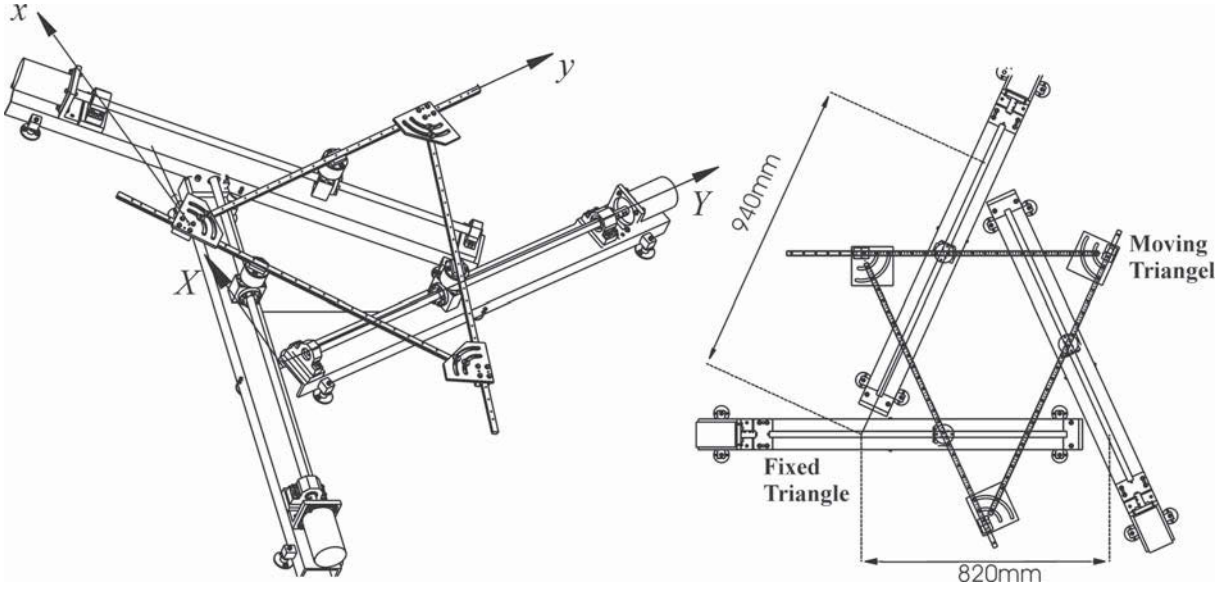

Fig. 2.7: Design of the PDTPM.

bility, is obtained when the movable and fixed triangles are identical isosceles triangles such that the ratio of the longer sides to the shorter side is 6:5.

2.3.3 Theoretical Framework

This paper focuses on the "Singularity Surfaces" and Workspace Analysis of the PDTPM. A detailed description of the Forward and Inverse Kinematics of this manipulator using kinematic mapping may be found in [14, 15].

Planar Kinematic Mapping

This is a brief introduction to planar kinematic mapping. It has been treated thoroughly by [6]. Consider a movable frame EE that can undergo general planar displacements relative to the fixed frame FF. A planar point, given by its homogeneous coordinates $(w : x : y)$ in EE, can be mapped into FF with the following homogeneous linear transformation

$$\begin{bmatrix} W \\ X \\ Y \end{bmatrix} = \begin{bmatrix} 1 & 0 & 0 \\ a & \cos\phi & -\sin\phi \\ b & \sin\phi & \cos\phi \end{bmatrix} \begin{bmatrix} w \\ x \\ y \end{bmatrix} \text{ or } \quad \boldsymbol{X} = \mathsf{A}\boldsymbol{x} \tag{2.8}$$

where $(W : X : Y)$ represent the homogeneous coordinates of the same point in FF. The parameters (a, b, ϕ) describe the general displacement of the origin of EE measured in the fixed frame FF, where (a, b) is the translation part and $\phi \in [0, 2\pi]$ is the rotation angle describing the orientation of EE relative to FF as shown in Fig. 2.8.

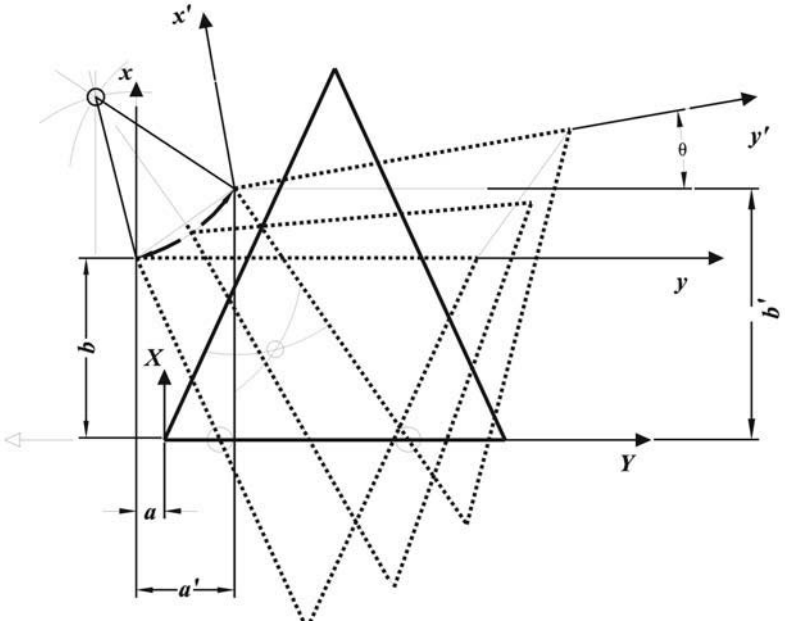

Fig. 2.8: Coordinate frames and displacements parameters of the PDTPM performing a polar rotation.

Grünwald and Blaschke [4, 5] simultaneously and independently developed a mapping Γ where a position in the moving space corresponds to a point in a three dimensional projective *image space*. Introducing the homogeneous coordinates $(X_0 : X_1 : X_2 : X_3) \neq (0 : 0 : 0 : 0)$ of the image space, these coordinates are defined in terms of the point transformation parameters in Eq. 2.9, by Eq. 2.8.

$$(X_0 : X_1 : X_2 : X_3) = ...$$
$$... = \left(2\cos\left(\frac{\phi}{2}\right) : a\sin\left(\frac{\phi}{2}\right) - b\cos\left(\frac{\phi}{2}\right) : a\cos\left(\frac{\phi}{2}\right) + b\sin\left(\frac{\phi}{2}\right) : 2\sin\left(\frac{\phi}{2}\right)\right) \tag{2.9}$$

Since each displacement (a, b, ϕ), $\phi \neq \pi$, has a corresponding point in image space the displacement parameters are

$$\tan\left(\frac{\phi}{2}\right) = \frac{X_3}{X_0} \tag{2.10}$$
$$a = \frac{2(X_1X_3 + X_0X_2)}{(X_0^2 + X_3^2)} \tag{2.11}$$
$$b = \frac{2(X_2X_3 - X_0X_1)}{(X_0^2 + X_3^2)} \tag{2.12}$$

Two special cases are of interest:

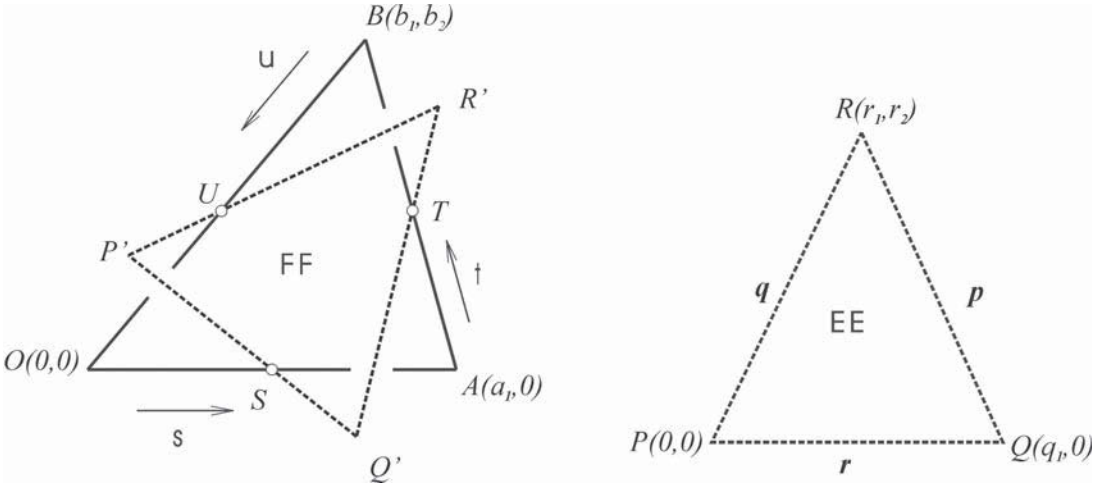

Fig. 2.9: Fixed and moving triangle vertices, sides and actuated R-joint centres.

- $X_3 = 0$, $X_0 \neq 0 :\Rightarrow \phi = 0$, describe pure translations;
- $X_0 = 0$, $X_3 \neq 0 :\Rightarrow \phi = \pi$ describe 180° turns.

Substituting Eqs 2.10- 2.12 into Eq. 2.8 the linear transformation can be expressed in terms of image space coordinates,

$$\begin{bmatrix} W \\ X \\ Y \end{bmatrix} = \begin{bmatrix} X_0^2 - X_3^2 & 0 & 0 \\ 2(X_0X_2 + X_1X_3) & X_0^2 - X_3^2 & -2X_0X_3 \\ -2(X_0X_1 - X_2X_3) & 2X_0X_3 & X_0^2 - X_3^2 \end{bmatrix} \begin{bmatrix} w \\ x \\ y \end{bmatrix} \tag{2.13}$$

for $(W : X : Y) \neq (0 : 0 : 0)$ and $(w : x : y) \neq (0 : 0 : 0)$.

2.3.4 Workspace Analysis of the PDTPM

Constraint Surfaces

This paper applies the method reported in [8] for the special case of the PDTPM a mechanism that is classified as a three legged PRP platform with virtually zero-length legs. As the first P-joint is the active joint it is effectively locked and may be temporarily removed from the chain. The remaining passive RP-subchain is constrained to move on a fixed point in EE. In other words:

- A line with fixed coordinates in the moving frame EE moves on a fixed point in the fixed frame FF.

Generally a line $\boldsymbol{l} = (L_0 : L_1 : L_2)$ goes through a point $P = (W : X : Y)$ when the following condition is fulfilled

$$L_0W + L_1X + L_2Y = 0 \tag{2.14}$$

Given the following lines in the moving frame $\boldsymbol{r}$, $\boldsymbol{p}$, $\boldsymbol{q}$ and the corresponding points S, T, U as shown in Fig. 2.9 the constraint can now be defined

$$\langle \boldsymbol{r}, S\rangle = 0, \quad \langle \boldsymbol{p}, T\rangle = 0, \quad \langle \boldsymbol{q}, U\rangle = 0 \tag{2.15}$$

As the lines are given in EE-coordinates and the points in FF-coordinates we have to find the transformation of lines from EE to FF, i.e. $\boldsymbol{r}$, $\boldsymbol{p}$, $\boldsymbol{q} \rightarrow \boldsymbol{r}'$, $\boldsymbol{p}'$, $\boldsymbol{q}'$. The planar line transformation A^* is simply the adjoint matrix of A [18].

$$\boldsymbol{r}'^T = \mathsf{A}^*\boldsymbol{r}^T, \quad \boldsymbol{p}'^T = \mathsf{A}^*\boldsymbol{p}^T, \quad \boldsymbol{q}'^T = \mathsf{A}^*\boldsymbol{q}^T \tag{2.16}$$

where

$$\mathsf{A}^* = \begin{bmatrix} X_0^2 + X_3^2 & -2(X_0X_2 - X_1X_3) & 2(X_0X_1 + X_2X_3) \\ 0 & X_0^2 - X_3^2 & -2X_0X_3 \\ 0 & 2X_0X_3 & X_0^2 - X_3^2 \end{bmatrix} \tag{2.17}$$

Looking at Fig. 2.9 where an ideal Cartesian coordinate frame has been chosen the actuator coordinates S, T, U in FF are described in terms of actuator parameters $0 \leq s, t, u \leq 1$ that enables us to define minimum and maximum range of each leg

$$S = (s_0 : s_1 : s_2) = (1 : a_1 s : 0) \tag{2.18}$$

$$T = (t_0 : t_1 : t_2) = (1 : a_1 + (b_1 - a_1)t : b_2 t) \tag{2.19}$$

$$U = (u_0 : u_1 : u_2) = (1 : b_1(1-u) : b_2(1-u)) \tag{2.20}$$

The line coordinates of $\boldsymbol{r}$, $\boldsymbol{p}$, $\boldsymbol{q}$ in EE according to Fig. 2.9 are

$$\boldsymbol{r}^T = \begin{bmatrix} R_0 \\ R_1 \\ R_2 \end{bmatrix} = \begin{bmatrix} 0 \\ 0 \\ 1 \end{bmatrix}, \quad \boldsymbol{p}^T = \begin{bmatrix} P_0 \\ P_1 \\ P_2 \end{bmatrix} = \begin{bmatrix} q_1 r_2 \\ -r_2 \\ r_1 - q_1 \end{bmatrix}, \quad \boldsymbol{q}^T = \begin{bmatrix} Q_1 \\ Q_2 \\ Q_3 \end{bmatrix} = \begin{bmatrix} 0 \\ r_2 \\ -r_1 \end{bmatrix} \tag{2.21}$$

The joint centre points in FF in terms of FF triangle vertices and actuator coordinates are

$$S\{s_0 : s_1 : s_2\} = S(O, A, s), \quad T\{t_0 : t_1 : t_2\} = T(A, B, t), \quad U\{u_0 : u_1 : u_2\} = U(B, O, u)$$

and the EE triangle edges in terms of its vertices are given by

$$r\{R_0 : R_1 : R_2\} = r(q_1), \quad p\{P_0 : P_1 : P_2\} = p(q_1, r_1, r_2), \quad q\{Q_0 : Q_1 : Q_2\} = q(r_1, r_2)$$

Substituting the given coordinates into Eq. 2.13 yield three quadrics in homogeneous Blaschke-Grünwald coordinates.

$$X_0X_1 + s_1X_0X_3 + X_2X_3 = 0 \tag{2.22}$$

$$(P_0 + P_1t_1 + P_2t_2)X_0^2 + 2P_2X_0X_1 - 2P_1X_0X_2 + 2(P_1t_2 - P_2t_1)X_0X_3 + 2P_1X_1X_3 + 2P_2X_2X_3 + (P_0 - P_1t_1 - P_2t_2)X_3^2 = 0 \tag{2.23}$$

$$(Q_1u_1 + Q_2u_2)X_0^2 + 2Q_2X_0X_1 - 2Q_1X_0X_2 + 2(Q_1u_2 - Q_2u_1)X_0X_3 + 2Q_1X_1X_3 + 2Q_2X_2X_3 - (Q_1u_1 + Q_2u_2)X_3^2 = 0 \tag{2.24}$$

These quadrics share a common absolute line. Intersecting the three quadrics, Eqs. 2.22-2.24 with plane $X_0 = 0$ produces the two absolute reguli of each.

$$X_2X_3 = 0 \tag{2.25}$$

$$[2P_1X_1 + 2P_2X_2 + (P_0 - P_1t_1 - P_2t_2)X_3]\,X_3 = 0 \tag{2.26}$$

$$[2Q_1X_1 + 2Q_2X_2 - (Q_1u_1 + Q_2u_2)X_3]\,X_3 = 0 \tag{2.27}$$

The intersection $X_0 \cap X_3$ represents the real absolute line shared among the three quadrics. Each has another line at infinity. It emerges upon de-homogenization by setting $X_3 = 1$. However these are all different. The common line will reduce the degree, from four to three, of the curve of intersection between any pair of such quadrics. Quadrics that contains two real absolute lines are hyperbolic paraboloids.

De-homogenizing with $X_0 = 1$ produces the three hyperbolic paraboloids.

$$X_1 + s_1X_3 + X_2X_3 = 0 \tag{2.28}$$

$$(P_0 + P_1t_1 + P_2t_2) + 2P_2X_1 - 2P_1X_2 + 2(P_1t_2 - P_2t_1)Q_3 + 2P_1X_1X_3 + 2P_2X_2X_3 + (P_0 - P_1t_1 - P_2t_2)X_3^2 = 0 \tag{2.29}$$

$$(Q_1u_1 + Q_2u_2) + 2Q_2X_1 - 2Q_1X_2 + 2(Q_1u_2 - Q_2u_1)X_3 + 2Q_1X_1X_3 + 2Q_2X_2X_3 - (Q_1u_1 + Q_2u_2)X_3^2 = 0 \tag{2.30}$$

Hence, given the maximum and minimum range of each leg yields six constraints surfaces. The solid bounded by these six *hyperbolic paraboloids* is the kinematic image of the platform workspace, where any displacement corresponds to a feasible EE position. A parameterized image of the six constraint surfaces is shown in Fig. 2.10.
Figure 2.11 illustrates different layers of the solid in image space. Each pair of parallel lines corresponds to the minimum and maximum range of the active joint of one leg at a certain orientation ϕ. The red regions represent the cross section of the solid. Now, given the inverse kinematic data of a certain motion [14, 15] that represents, e.g., a curve in image space,

- this displacement $c(t)$ is said to be singularity-free as long as it stays within this solid region, see Fig. 2.11.

On the other hand we could state:

- Given two poses within the solid region in image space, any curve going through these two points and staying within the solid represents a singularity-free motion.

This is a useful and elegant approach to determine singularity-free movements to optimize the design and the kinematic synthesis.

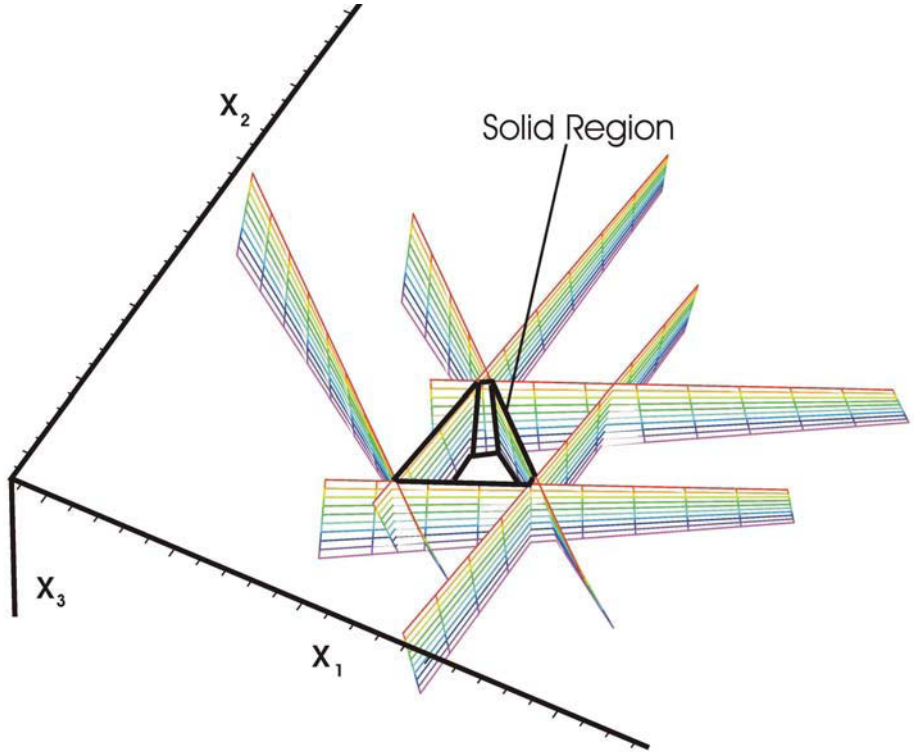

Fig. 2.10: Sectional part of the solid region wherein all movements are singularity free.

2.3.5 Singular Poses of the PDTPM

The singular configurations of planar three-legged platforms have been studied in detail by [16] and [19] where singularity analysis were based on *Jacobian* matrices.
Consider a finite movement of the platform, then the coordinates $(X_0 : X_1 : X_2 : X_3)$ in image space are functions of time. The time derivative of the three, one for each joint, constraint surface equations of the form of Eqs. 2.22-2.24 yields three equations that are linear in $\dot{X}_0, \dot{X}_1, X_2, \dot{X}_3$. From Eq. 2.9 we know another such linear relation.

$$X_0^2 + X_3^2 = 1, \rightarrow X_0\dot{X}_0 + X_3\dot{X}_3 = 0 \tag{2.31}$$

These four equations, linear in $\dot{X}_i$, can be expressed as

$$\begin{bmatrix} a_{11} & a_{12} & a_{13} & a_{14} \\ a_{21} & a_{22} & a_{23} & a_{24} \\ a_{31} & a_{32} & a_{33} & a_{34} \\ a_{41} & a_{42} & a_{43} & a_{44} \end{bmatrix} \begin{bmatrix} \dot{X}_1 \\ \dot{X}_2 \\ \dot{X}_3 \\ \dot{X}_4 \end{bmatrix} = 0, \quad \text{or} \quad \mathsf{B}\dot{\mathbf{X}} = 0 \tag{2.32}$$

Obtaining coefficients of Matrix B as set forth by [19] is tedious but easy. The platform is in a singular configuration whenever

$$\det \mathsf{B} = 0 \tag{2.33}$$

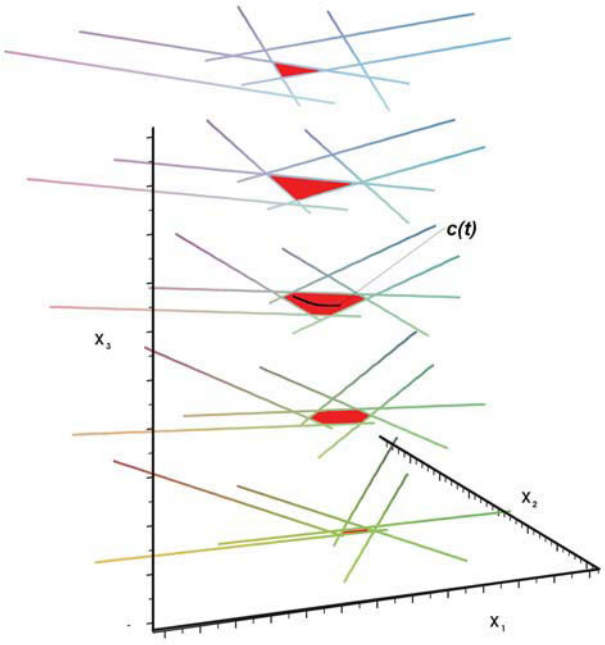

Fig. 2.11: Layers of the solid representing all possible positions at a fixed orientation ϕ.

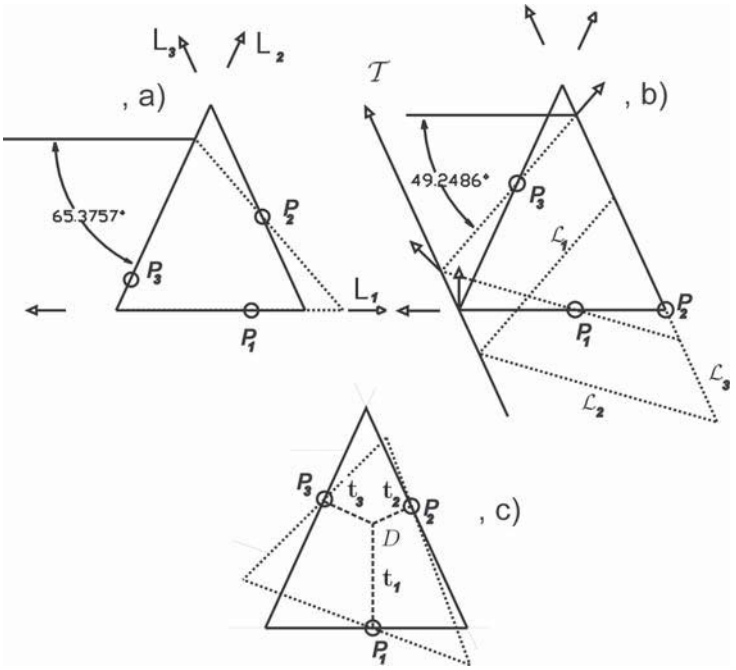

Fig. 2.12: Examples of singular poses, case a) and b) are type 1, case c) is type 2.

This is the case in the following configurations:

- The PDTDM is in a singular pose whenever L_i=$\mathcal{L}_i$, for $i = 1$ or 2 or 3 become collinear as shown in Fig. 2.12. In this configuration a displacement of the actuator P_2 does not produce any motion of EE that represents the movable triangle [16]. This type of singularity theoretically leads to six singular poses.
- The second type of singularity occurs when the three vectors $\mathbf{t}_i$, perpendicular to L_i intersect at a common point D, as shown in Fig. 2.12. In this pose the moving triangle EE can undergo a finite rotation about D when a torque is applied, even with locked actuators.
- The third type of singularity is the combination of the the two types just mentioned.

Applying the singularity analysis to this particular PDTPM design we reach the following conclusions:
This PDTPM is for example in a singular pose, according to Fig. 2.12, whenever

$$\text{(a) } \phi_1 = -49.2486^\circ \quad a, b \text{ moving along } \mathsf{L}_3 \tag{2.34}$$
$$\text{(b) } \phi_2 = +49.2486^\circ \quad a, b \text{ moving along } \mathcal{T} \tag{2.35}$$
$$\text{(c) } \phi_3 = +65.3757^\circ \quad a, b = 0 \tag{2.36}$$

However, considering the workspace analysis (see Fig. 2.11) that restricts the maximum orientation angles from -48,5° to +62° due to design-limited joint ranges only case (b) remains.
Singularity poses of type two can be avoided by using the following approach:
Let us assume that the position of the EE is given by its displacement parameters (a, b, ϕ). As the coordinates of P_i, obtained by inverse kinematics, and the *line coordinates* of $\mathcal{L}_i$ are known we may calculate $\mathbf{t}_i$. If $\mathbf{t}_i$, given in homogeneous coordinates $(t_1 : t_2 : t_3)$, intersect in one point D, it follows

$$\mathbf{t}_i \cdot D = 0 \text{ for } i = 1, 2, 3 \tag{2.37}$$

2.3.6 Conclusions

In this paper kinematic mapping has been successfully employed to analyze the reachable workspace of the PDTPM. It was shown that geometric preprocessing allows simplification and subsequent solution of the sets of polynomial constraint equations. Kinematic mapping is a useful, elegant alternative approach to determine singularity-free zones in the workspace to optimize the design and the kinematic synthesis of a manipulator.

References

[1] J-P. Merlet, "Parallel manipulators, state of the art and perspectives", 1999, [Online]. Available: http://wwwsop. inria.fr/saga/personnel/merlet/merlet.html.

[2] J-P. Merlet, *Les Robots Paralléles*, Hermés Publishers, Paris, France, 1990.

[3] M. L. Husty, "On the workspace of planar three-legged platforms", *Proc. World Automation Conf., 6th Int. Symposium on Rob. and Manuf. (ISRAM 1996)*, Montpellier, France, Vol. 3, pp. 339-344, 1996.

[4] W. Blaschke, "Euklidische Kinematik und Nichteuklidische Geometrie", *Zeitschr. Math. Phys.*, Vol. 60, pp. 61- 91 and 203-204, 1911.

[5] J. Grünwald, "Ein Abbildungsprinzip, welches die ebene Geometrie und Kinematik mit der räumlichen Geometrie verknüpft", *Sitzber. Ak. Wiss. Wien*, Vol. 120, pp. 677-741, 1911.

[6] O. Bottema and B. Roth, *Theoretical Kinematics*, Dover Publications, Inc., New York, N.Y., U.S.A., 1990.

[7] M. J. D. Hayes, M. L. Husty and P. J. Zsombor-Murray, "Kinematic mapping of planar Stewart-Gough platforms", *Proc. 17th Canadian Congress of Applied Mechanics (CANCAM 1999)*, Hamilton, On., Canada, pp. 319-320, 1999.

[8] M. J. D. Hayes and M. L. Husty, "On the kinematic constraint surfaces of general three-legged planar robot platforms", *Mechanism and Machine Theory*, Vol. 38, No.5, pp. 379–394, 2003.

[9] P. J. Zsombor-Murrary, C. Chen, and M. J. D. Hayes, "Direct kinematic mapping for general planar parallel manipulators", *Proceedings CSME Forum 2002*, Kingston, On., Canada, 2002.

[10] C. Gosselin, "Kinematic analysis, optimization and programming of parallel robotic manipulators", PhD thesis, Dept. of Mech. Eng., McGill University, Montréal, Qc., Canada, 1988.

[11] H. R. M. Daniali,, "Contribution to the kinematic synthesis of parallel manipulators", Ph.D. thesis, McGill University, pp.141-142, 1995.

[12] A. Yu, "Design and analysis of planar parallel three-legged PRP manipulators", M. Eng. thesis, McGill University, 2005.

[13] J. Shum, "Kinematic analysis of spherical double-triangular parallel manipulators", M. Eng. thesis, McGill University, 2001.

[14] N. G. Tilton, "Projective geometry and planar kinematic mapping in kinematic analysis: the kinematic analysis of a planar double-triangular parallel manipulator", B. Eng.(hons.), McGill University, 2002.

[15] R. Neumayr, "Camera-aided robot calibration of the planar double-triangular parallel manipulator", Diplomarbeit, Institute for Automation, Montanuniversität Leoben, Austria, 2004.

[16] H. R. M. Daniali, P. J. Zsombor-Murray and J. Angeles, "The kinematics of 3-DOF planar and spherical double-triangular parallel manipulators", *Computational Kinematics*, Kluwer Academic Publishers, pp. 153-164, 1993.

[17] I. A. Bonev, D. Zlatanov and C. M. Gosselin, "Singularity analysis of 3-DOF planar parallel mechanisms via screw theory", *Journal of Mechanical Design*, Vol. 125, pp.573, 2003.

[18] P. J. Zsombor-Murray, "Planar kinematic mapping fundamentals", 2009, [Online]. Available: http://www.cim.mcgill.ca/ paul/PKMF6Ac.pdf

[19] M. L. Husty, M. J. D. Hayes, H. Loibnegger," The general sigularity surface of planar three-legged platforms", *Advances in Multibody Systems and Mechatronics*, Duisburg Germany, pp. 203-214, 1999.

2.4 Precise Pose Measurement with Single Camera Calibration for Planar Parallel Manipulators

Richard Neumayr, Paul Zsombor-Murray[2], Paul O'Leary

Abstract [1]

Pose measurement is an important tool for robot calibration. This paper describes the development and implementation of a technique of camera-aided pose measurement, tested on the Planar Double Triangular Parallel Manipulator (PDTPM). A stationary camera is used to take photos of the End Effector (EE) whereon a certain array of Light Emitting Diodes (LED) is mounted. Using various image processing techniques, the coordinates of the LEDs are registered in the image in order to derive the projection matrix that maps any point of the image plane to world coordinates in the EE moving plane. This homography is computed with a method where the vanishing line is treated as the principal component. This estimate is more robust and faster than the Direct Linear Transformation (DLT) method. It was shown that poses could be quickly registered at submillimetre precision notwithstanding inexpensive, relatively low resolution optics. The measurement system is easy to set up, portable, accurate, low cost and it is believed to be a valuable tool.

2.4.1 Introduction

This paper presents a vision-based measurement method with a single camera to perform precise and direct full pose measurements on planar parallel manipulators. Manipulator accuracy is compromised by discrepancy between actual end effector (EE) pose and that obtained via direct kinematics (DK) computation using measured actuated joint coordinates. Due to random errors (e.g., finite resolution of joint encoders) and systematic errors (e.g., manufacturing tolerances, measurement errors of link lengths, joint offsets, gear transmission error) there is always a mismatch and therefore lack of accuracy. Calibration helps by benchmarking any desired number of EE poses and unequivocally relating these to the corresponding measured joint coordinates with , e.g., a kinematic error model described in Zhuang et al. [1]. The measurement method described in this paper is considered to be a valuable tool to simplify the kinematic calibration structure of planar parallel mechanisms. Robot calibration has been studied and applied for decades [2]. Determining the EE's exact and full pose by a redundant measurement device is one major

[2]Paul Zsombor-Murray is with McGill University, Centre for Intelligent Machines, Montréal, Canada.

[1]This paper originally appeared as: R. Neumayr, P. J. Zsombor-Murray, P. O'Leary, "Precise pose measurement with single camera calibration for planar parallel manipulators", *CSME TRANSACTIONS*, Vol. 35, No. 2, pp. 201–213, 2011.

issue in kinematic calibration [1]. In [3] and [4] vision-based pose measurement systems have been studied and evaluated to perform kinematic calibration on serial mechanisms. These applications are based on hand-eye camera calibration a method that needs tedious camera re-calibration at each pose. Another approach is to employ multiple camera setups to achieve full pose measuring capability which in turn entails increased equipment costs. Commercial serial robot manufacturers like FANUC [5], KUKA [6] or ABB [7] already have considered these techniques as a potential tool for calibration and employed it in some industrial applications. As far as vision based calibration of parallel manipulators is concerned research work on this particular topic has been done by Bai et al. [8] where a high cost three-camera system is used and by Renaud et al. [9,10] where in [10] a H4-robot was calibrated by means of a single camera procedure that also needs to employ a hand-eye calibration method to achieve full pose measurement capability.

However claimed novelty and superiority of the method and set up to be described are based on selection and adaptation of equipment and methodology to a particular but nevertheless broad class of robots [11], viz., three legged planar parallel manipulators. Though experiments reported herein were carried out on a peculiar, possibly bizarre, representative of this class, Chen [12] gives ample evidence that all members are essentially similar from a computational kinematics standpoint. Furthermore the design and development first described by [13] of the Planar Double Triangular Parallel Manipulator (PDPTM) used in our calibration exercises has been a subject of our research over a number of years as documented by Tilton [14] , Neumayr [15] and Yu [16]. In contrast, research on calibration techniques is often carried out on commercial equipment and design parameters used in DK calculations are taken as supplied by the manufacturer.

The main contributions of this paper are:

1. Demonstrated full pose measurement of planar parallel robots by camera requires no elaborate equipment nor environmental control;
2. Images of an EE mounted planar array of LED markers can be efficiently and accurately converted homographically to yield EE coordinates in a fixed reference frame FF without employing a hand-eye calibration method;
3. It is shown that tests of this pose measurement technique on the PDTPM give reproducable results with pose measurement tolerances lower than one millimeter.

The objective of this research was to investigate aspects involved in robot calibration methods to develop a feasible low cost vision-based measurement system with a single camera. The stationary-camera setup has distinct advantages [3]. It is non-invasive. The cameras are placed outside the robot workspace, and need not be removed after robot calibration. Particularly in this case there is no need to identify the transformation relating the camera frame to the EE-frame (hand-eye calibration, hand-mounted camera calibration). Hence, direct full pose measurement can be easily performed. Especially in

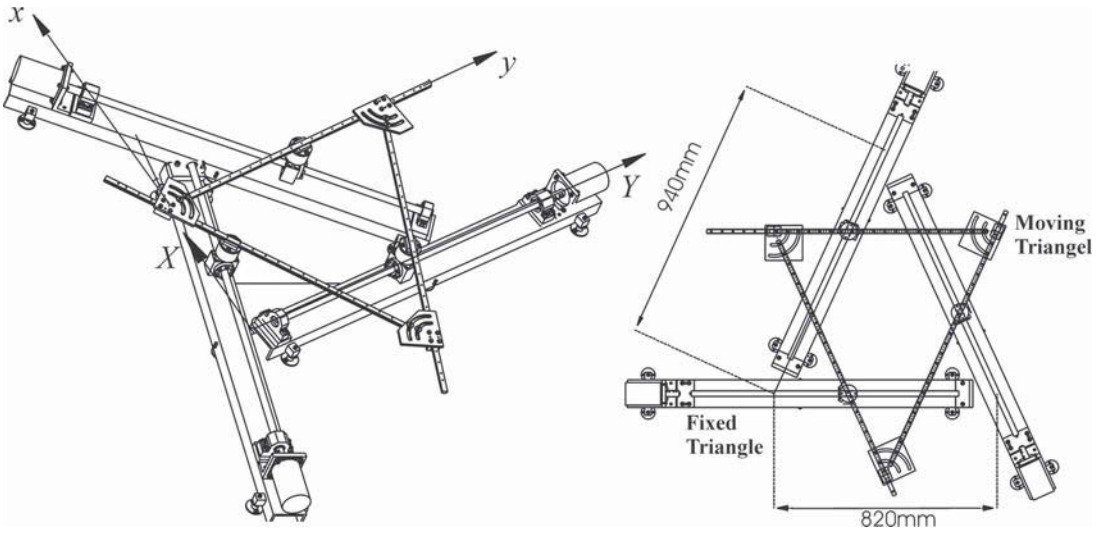

Fig. 2.13: Design of the PDTPM

the case of planar manipulators which have smaller workspace, the EE is most likely in the field of view of the camera.

2.4.2 Design of the PDPTM

Fixed Triangle – Each leg of the fixed triangle is a recirculating ball screw assembly driven by a stepper motor, all mounted on an aluminum channel as shown in Fig. 2.13. Each leg assembly may be moved independently of the other two legs of the fixed triangle.

Moving Triangle – The three edges of the movable triangle are made of steel rails designed to mount a ball trolley, like a linear bearing that runs on a rail as shown in Fig. 2.13. In operation the three rails are fixed relative to each other.

PRP-Joints – The linear bearing on a rail of the movable triangle is joined to the corresponding ball screw nut of the fixed triangle through a revolute joint formed using a pair of angular contact bearings.

Calibration Object – The calibration object is a matte, black metal plate onto which seven flat-headed LEDs V_{1-7} are fixed in a specific array, shown in Fig. 3.1. The positions of these LEDs are pre-measured precisely, i.e., the holes were machined on a jig borer. Figure 2 shows the calibration object mounted on the EE which is the moving triangle.

2.4.3 Theoretical Framework

Determination of Homography

The accuracy of camera calibration is a major issue in vision. Hence, computing an exact homography is one of the key factors to minimize resulting pose measurement er-

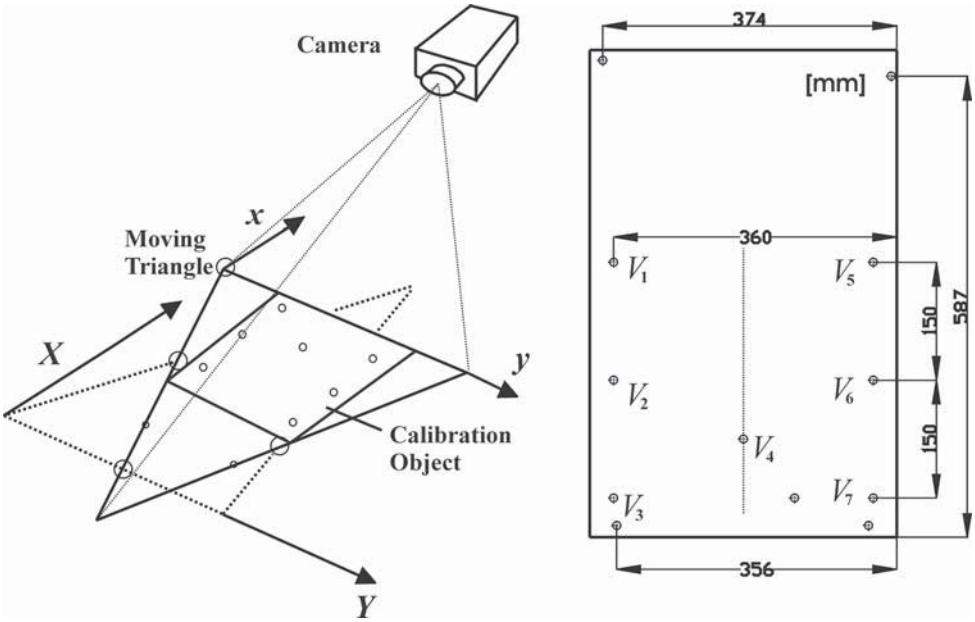

Fig. 2.14: Calibration object and measurement setup, dimensions in [mm]

rors. In this paper a method [17] that differs considerably from the classical DLT [19] for computing the homography is presented.

A projective transformation between two planes is given by

$$\mathbf{p}' = \mathbf{H}\mathbf{p} \tag{2.38}$$

where a point $\mathbf{p}$ is mapped from plane $\prod$ (image) to plane $\sum$ (workspace of the PDTPM) and is defined there as $\mathbf{p}'$. Consider that in Eq. (2.39) points are expressed in terms of the homogeneous coordinates of the projective plane $\mathbf{p}'$.

$$\begin{bmatrix} x' \\ y' \\ w' \end{bmatrix} = \begin{bmatrix} h_1 & h_2 & h_3 \\ h_4 & h_5 & h_6 \\ h_7 & h_8 & h_9 \end{bmatrix} \begin{bmatrix} x \\ y \\ w \end{bmatrix} \tag{2.39}$$

Expanding Eq. (2.39) for a given point datum, and normalizing with respect to the homogeneous component yields

$$x'_i = \frac{h_1 x_i + h_2 y_i + h_3}{h_7 x_i + h_8 y_i + h_9} \tag{2.40}$$

$$y'_i = \frac{h_4 x_i + h_5 y_i + h_6}{h_7 x_i + h_8 y_i + h_9} \tag{2.41}$$

Setting w=w'=1 and rearranging the two equations above leads to

$$\begin{bmatrix} x_i & y_i & 1 & 0 & 0 & 0 & -x'_i x_i & -x'_i y_i & -x'_i \end{bmatrix} \mathbf{h} = 0 \tag{2.42}$$

$$\begin{bmatrix} 0 & 0 & 0 & x_i & y_i & 1 & -y'_i x_i & -y'_i y_i & -y'_i \end{bmatrix} \mathbf{h} = 0 \tag{2.43}$$

or

$$\begin{bmatrix} \mathbf{P} & \mathbf{0} & \mathbf{X'P} \\ \mathbf{0} & \mathbf{P} & \mathbf{Y'P} \end{bmatrix} \begin{bmatrix} \mathbf{g}_1 \\ \mathbf{g}_2 \\ \mathbf{g}_3 \end{bmatrix} = \mathbf{r} \tag{2.44}$$

where $\mathbf{r}$ is the vector of algebraic residuals and

$$\mathbf{P} = \begin{bmatrix} x_1 & y_1 & 1 \\ \vdots & \vdots & \vdots \\ x_n & y_n & 1 \end{bmatrix} \tag{2.45}$$

$$\mathbf{g}_1 = \begin{bmatrix} h_1 \\ h_2 \\ h_3 \end{bmatrix}, \mathbf{g}_2 = \begin{bmatrix} h_4 \\ h_5 \\ h_6 \end{bmatrix}, \mathbf{g}_3 = \begin{bmatrix} h_7 \\ h_8 \\ h_9 \end{bmatrix} \tag{2.46}$$

as well as

$$\mathbf{X'} = \text{diag}(-x'_1, \cdots, -x'_m) \text{ and } \mathbf{Y'} = \text{diag}(-y'_1, \cdots, -y'_m) \tag{2.47}$$

Rearrangement of the equations leads to a block partitioned sparse matrix, Eq. (2.44). Through an orthogonalization procedure that is described in detail in [17] we rewrite this system:

$$\mathbf{r} = \begin{bmatrix} \mathbf{P} & \mathbf{0} \\ \mathbf{0} & \mathbf{P} \end{bmatrix} \begin{bmatrix} \mathbf{g}_1 \\ \mathbf{g}_2 \end{bmatrix} + \begin{bmatrix} \mathbf{X'P} \\ \mathbf{Y'P} \end{bmatrix} \mathbf{g}_3 \tag{2.48}$$

Equation (11) is now equivalent to a general system to minimize of the form $\|\mathbf{Ax}\text{-b}\|_2^2$ $\rightarrow \mathbf{x}=\mathbf{A}^+\text{b}$, where $\mathbf{A}^+$ denotes the Moore-Penrose pseudo-inverse. Consequently we may express

$$\begin{bmatrix} \mathbf{g}_1 \\ \mathbf{g}_2 \end{bmatrix} = - \begin{bmatrix} \mathbf{P} & \mathbf{0} \\ \mathbf{0} & \mathbf{P} \end{bmatrix}^+ \begin{bmatrix} \mathbf{X'P} \\ \mathbf{Y'P} \end{bmatrix} \mathbf{g}_3 \tag{2.49}$$

eliminate $\mathbf{g}_1$ and $\mathbf{g}_2$ by substituting in Eq. (2.48) and derive

$$\mathbf{r} = \begin{bmatrix} \mathbf{I} - \mathbf{PP}^+ & \mathbf{X'P} \\ \mathbf{I} - \mathbf{PP}^+ & \mathbf{Y'P} \end{bmatrix} \mathbf{g}_3 = \mathbf{D}\mathbf{g}_3 \tag{2.50}$$

and minimize $\| \mathbf{D}\mathbf{g}_3\|_2^2$ subject to $\mathbf{g}_3^T\mathbf{g}_3$=1.

We have reduced the linear system to a function of only h_7, h_8 and h_9 with backsubstitution relations for h_1 through h_6. The term ($\mathbf{I}$-$\mathbf{PP}^+$) in Eq. (2.50) is the projection

onto the orthogonal complement of $\mathbf{P}$. We take the minimizing solution subject to $\mathbf{g}_3$ corresponding to the smallest singular value. This implicitly imposes the constraint

$$h_7^2 + h_8^2 + h_9^2 = 1 \tag{2.51}$$

Looking at Eq. (2.39) where we have

$$w' = h_7 x + h_8 y + h_9 w \tag{2.52}$$

points $[x\ y\ 1]^T$ are mapped to a point with w'=0

$$h_7 x + h_8 y + h_9 w = 0 \tag{2.53}$$

which is the equation of the vanishing line of the original image. The vanishing line is therefore treated as the principal component in the analysis. This estimate is more robust, since the position of the vanishing line depends only on the relative position and orientation of the camera to the observed plane. A flop count indicates that the new method converges faster [17] than the common DLT .

Nonlinear Approximation of Homography

This approximation [18] optimizes the entries of the collineation matrix $\mathbf{H}$ so that geometric distances among corresponding points in both planes are minimized in a least squares sense. A function f that defines the relationship between these corresponding points, using the parameters of the homography, is formulated. This function is derived from the shape of the calibration spots. Given x_0, y_0 and r, which are the center coordinates and the radius of a circular light spot, the geometric distance of a datum or contour point to the circle is defined as

$$f(\mathbf{x}_{pc}, \mathbf{h}) = \sqrt{(x_0 - x_{a,i})^2 + (y_0 - y_{a,i})^2} - r \tag{2.54}$$

where $x_{a,i}$ and $y_{a,i}$ are the inhomogeneous metric-coordinates of a data point. Having the pixel-coordinates of the contour points $\mathbf{x}_{pc} = [x_{pc}\ y_{pc}\ 1]^T$, the corresponding metric-representation of a point is given by

$$x_{a,i} = \frac{x_i}{w_i} = \frac{h_1 x_{pc} + h_2 y_{pc} + h_3}{h_7 x_{pc} + h_8 y_{pc} + h_9} \tag{2.55}$$

$$y_{a,i} = \frac{y_i}{w_i} = \frac{h_4 x_{pc} + h_5 y_{pc} + h_6}{h_7 x_{pc} + h_8 y_{pc} + h_9} \tag{2.56}$$

Substituting these two equations into Eq. (2.54), yields the cost function. This function is in general not zero since the data points do not usually define any perfect circle.

$$f(\mathbf{x}_{pc}, \mathbf{h}) = e_{pc} \neq 0 \tag{2.57}$$

The Gauss-Newton method is applied to minimize the sum of the squares of the residuals $\sum e_{pc}^2$. The normalization of the matrix $\mathbf{H}$ by setting h_9=1 implies that there are only eight non-zero partial derivatives. The coefficient vector increment is

$$\Delta \mathbf{h} = -\mathbf{J}^{+}_{\mathbf{f}(\mathbf{x}_{pc},\mathbf{h}_0)} \mathbf{f}(\mathbf{x}_{pc}, \mathbf{h}_0) \tag{2.58}$$

where $-\mathbf{J}^{+}_{\mathbf{f}(\mathbf{x}_{pc},\mathbf{h}_0)}$ is the Jacobian pseudo-inverse. The increment $\Delta\mathbf{h}$ is determined using the initial guess $\mathbf{h}_0$ that is derived by the method in Section 3.1.

2.4.4 Vision-based Pose Measurement and Kinematic Calibration

This section describes the interaction between vision-based metrology and kinematic calibration and enumerates the steps to perform full pose measurement.

Calibration Pose

The *calibration pose* has two key attributes: It is the reference pose for camera calibration and it provides the basis for full-pose measurement (position and orientation) with respect to the fixed frame. Therefore this pose has to be pre-measured precisely by a redundant measurement system as this data is used to compute the projection matrix and furthermore the pose of the EE.

Camera Calibration

The problem of determining the exact pose of the EE with the help of a digital camera is solved by finding the projection matrix $\mathbf{H}$ that maps any point of the EE-plane to the camera image. Once this projection matrix is available we are able to assign physical coordinates to any image pixel. Various camera calibration techniques are explained in [3, 4, 19], however, using LED markers for calibration of planar parallel mechanisms has, to the best of the authors' knowledge, never been done. By taking a snapshot (1024x768 pixel) of the EE at a precisely pre-measured *calibration pose*, the LEDs can be identified as small illuminated ellipses, Fig. 2.15. In order to derive the ellipses mid-points we apply the Matlab contour algorithm to extract the desired contours and use the fitting algorithm discussed before to compute $\mathbf{H}$. Depending on the lighting conditions it is possible that some LEDs cannot be found, however only four points are needed for a successful calibration. The extracted midpoints are then sorted.

Pose Measurement

A planar point, given by its homogeneous coordinates $(x : y : w)$ in EE, can be mapped into FF (fixed frame) with the following homogeneous linear transformation

$$\begin{bmatrix} X \\ Y \\ W \end{bmatrix} = \begin{bmatrix} \cos\phi & -\sin\phi & a \\ \sin\phi & \cos\phi & b \\ 0 & 0 & 1 \end{bmatrix} \begin{bmatrix} x \\ y \\ w \end{bmatrix} \tag{2.59}$$

where $(X : Y : W)$ represent the homogeneous coordinates of the same point in FF. The parameters (a, b, ϕ) describe the general displacement of the origin of EE measured in the

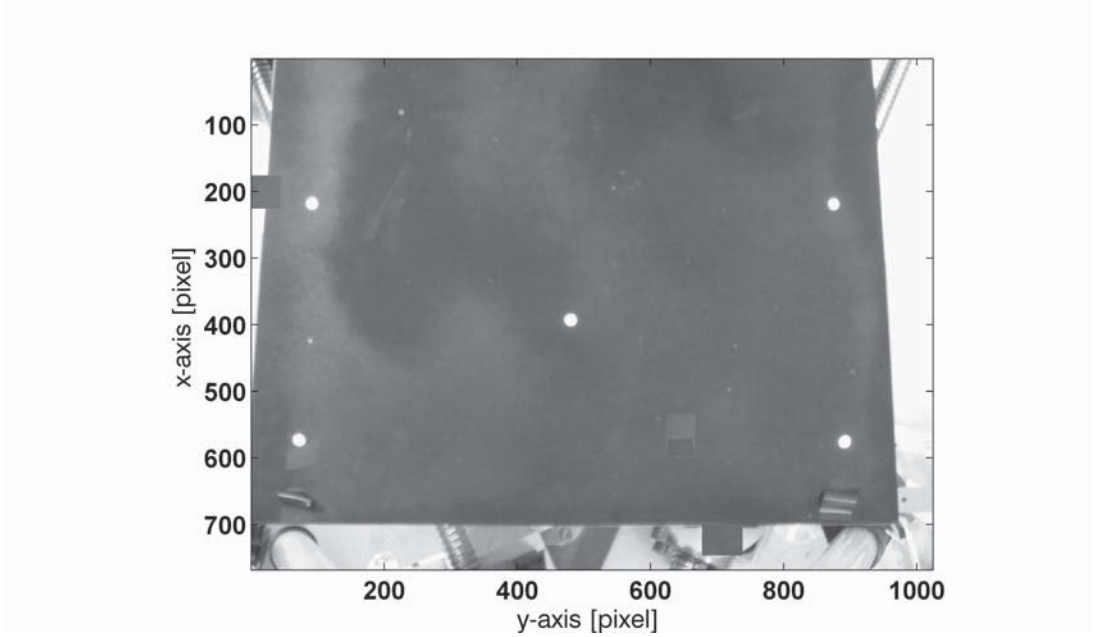

Fig. 2.15: Calibration image

fixed frame FF, where (a, b) is the translation part and $\phi \in [0, 2\pi]$ is the rotation angle describing the orientation of EE relative to FF. The coordinate frames and displacement parameters are shown in Fig. 2.16, where the EE is performing a polar rotation.

As the displacement parameters of the *calibration pose* as well as the relative position of the calibration target on the EE are known we are able to perform full-pose measurement with respect to the FF after successful camera calibration.
For a new position (a_n, b_n, ϕ_n) at least two points must be registered. The other LEDs can be used statistically to further improve calibration accuracy.

Kinematic Calibration and Vision

One method that deals with kinematic calibration of parallel mechanism is described in [1]. It is based on the inverse kinematic model that computes the joint variables $\mathbf{q}$ as a function of the end effector pose $\mathbf{T}$=($\mathbf{R}$,$\mathbf{t}$), represented by a rotation-matrix and a translation-vector, and the kinematic parameter vector $\mathbf{k}$. Hence, a pose error can be formulated as follows

$$\epsilon = \tilde{\mathbf{q}} - \mathbf{q}(\mathbf{T}, \mathbf{k}) \tag{2.60}$$

where $\tilde{\mathbf{q}}$ is the measured joint value vector, e.g., transducer readings of the electric motors, and $\mathbf{q}$ are the joint variables derived from the pose measurement by a redundant, e.g. vision-based, measurement system. The parameter vector $\mathbf{k}$ can finally be estimated by

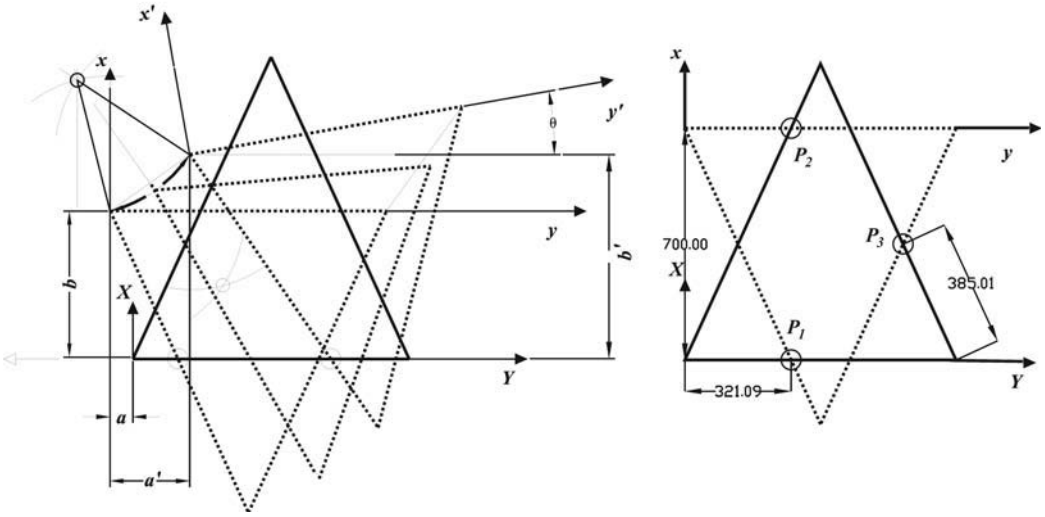

Fig. 2.16: Right: Coordinate frames of the PDTPM and displacement parameters, Left: Definition of *calibration pose*.

minimizing the following cost function

$$\min_{\mathbf{k}} \sum_{i=1}^{m} \|\tilde{\mathbf{q}}_i - \mathbf{q}_i(\mathbf{T}_i, \mathbf{k})\|^2 \tag{2.61}$$

where i denotes the number of measurements. As the measurement system described in this paper enables full pose measuring capability Zhuang's et al. [1] calibration method is a suitable approach to overcome the kinematic problem.

Another method to perform kinematic calibration is described in [20] where the implicit kinematic model is used. This model relates the joint values, the end effector pose and the kinematic parameters in one equation.

$$f(\mathbf{q}, \mathbf{T}, \mathbf{k}) = 0 \tag{2.62}$$

Hence, the implicit kinematic model can be formally stated as the the following nonlinear minimization problem

$$\min_{\mathbf{k}} \sum_{i=1}^{m} \|f(\tilde{\mathbf{q}}_i, \tilde{\mathbf{T}}_i, \mathbf{k})\|^2 \tag{2.63}$$

To solve Eq. (2.63) the exact measured pose of the EE is required. It can be provided by, e.g., this vision based measurement system.

	# Meas.	Mean Error	Max Error	STD
a	5	0.22	0.35	0.20
b	5	0.24	0.35	0.21
ϕ	5	0.04	0.06	0.04

Table 2.1: Accuracy of camera calibration (a, b) in [mm], ϕ in [rad]

	# Meas.	Mean Error	Max Error	STD
a	5	0.20	0.33	0.19
b	5	0.22	0.34	0.20
ϕ	5	0.04	0.05	0.03

Table 2.2: Accuracy of pose measurement at pre-measured position $(a_e, b_e, \phi_e) = (0, 690, 0)$, (a, b) in [mm], ϕ in [rad]

2.4.5 Test Results

The PDTPM is run by stepper motors with a resolution of 200 steps per revolution. As the ball screws that they drive have a pitch of 5 [mm], one step, that corresponds to 25 [μm], is very small.

Camera Calibration Accuracy

In order to test the reproducibility of camera calibration, the EE is moved several times to the *calibration pose* (a_c, b_c, ϕ_c) that is pre-measured precisely before with a tolerance of ± 0.1 [mm]. The accuracy of the calibration is tested by multiplying the inverse of the computed projection matrix $\mathbf{H}$ with the detected pixel coordinates of the LEDs. This should give the positions of the LEDs in fixed frame coordinates again.

Table 1 shows the results where the mean, maximum and standard deviation of $\|\mathbf{p}_m - \mathbf{p}_c\|$ are listed against the number of measurements, where $\mathbf{p}_m = (a_m, b_m, \phi_m)$ are the measured poses and $\mathbf{p}_c = (a_c, b_c, \phi_c)$ is the pre-measured *calibration pose*.

Pose Measurement Accuracy

In order to evaluate the accuracy of this vision-based system the calibration object was demounted from the EE and then moved to precisely pre-measured positions within a tolerance of ± 0.1 [mm] by using gauge blocks. Table 2 shows the the results of these measurements where the calibration object was, e.g., moved 10 [mm] in negative x-direction to $(a_e, b_e, \phi_e) = (0, 690, 0)$. The accuracy is comparable with the camera calibration measurements. The measurement error is on average around 0.2 [mm].

Pose Measurement on the PDTPM

After successful calibration the joints P_2 and P_3 are moved 45 [mm], as shown in Fig. 2.17. Then another photo (1024x768 pixel) of the calibration object is taken at the new pose. In this case it is expected that the EE-pose might significantly differ from

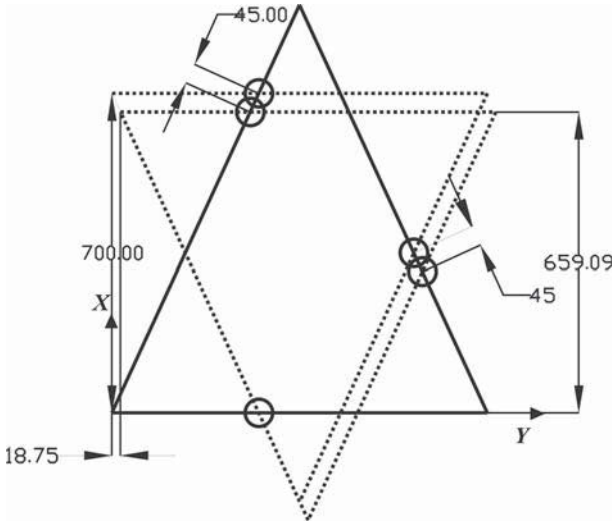

Fig. 2.17: Direct forward kinematics, dimensions in [mm]

	# Meas.	Mean Error	Max Error	STD
a'	5	0.42	0.51	0.37
b'	5	0.23	0.38	0.18
ϕ'	5	0.07	0.11	0.05

Table 2.3: Accuracy of of pose #1 (a', b') in [mm], ϕ' in [rad]

the DK calculation due to kinematic error resulting from ,e.g., measurement errors of leg lengths or joint offsets. Direct forward kinematics calculation gives us the following results for the new pose where (a', b') is given in [mm] and ϕ' in [rad].

$$(a', b', \phi') = (18.75, 659.09, 0) \tag{2.64}$$

This measurement is repeated several times to investigate the reproducibility. Table 3 illustrates the following result, where the mean, maximum and standard deviation of $\|\mathbf{p}_m - \mathbf{p}_p\|$ against the number of measurements are listed where $\mathbf{p}_m = (a_m, b_m, \phi_m)$ are the measured poses and $\mathbf{p}_p$ is the predicted EE pose. One can see a slight offset in parameter a'.

Kinematic Calibration

As this measurement setup gives direct full pose data of the end effector one can easily apply the methods discussed in Section 4.4 to perform kinematic calibration. In the case of the PDTPM the inverse kinematic problem is rather simple and involves the intersection of three line pairs between corresponding legs of the fixed and moving triangles. The kinematic parameters for the inverse kinematic model are described and identified in detail in [14].

Sources of Measurement Inaccuracy

The most probable sources of measurement error are listed below.

1. Input Parameters: The calibration positions of the LEDs given in real-world coordinates have to be measured very accurately. Measurement errors of, e.g., 0.5 [mm], have a significant effect on the computed projection matrix **H** and consequently the resulting pose measurement.

2. Kinematic errors:
   Due to, e.g., manufacturing tolerances, measurement errors of leg lengths, joint offsets, direct kinematics gives inaccurate predicted results. Kinematic calibration methods using this measurement setup to overcome this problem are discussed in Section 4.4.

3. Resolution:
   Pixel resolution usually dominates the effects of deterministic errors due to imperfect calibration of the camera perspective transformation matrix **H**.

4. Stepper motors:
   The motors, due to inertia, might lose steps if too much acceleration is induced.

5. Vibration:
   Camera shake leads to images with more noise and therefore inaccurate camera calibration.

2.4.6 Conclusion

This technique of camera-aided pose measurement has been successfully tested on the *PDTPM*. The pose-measurement results are within the expected tolerance of ± 1 [mm]. The advantages of this technique are:

- Compared with laser interferometers, the vision system does not require a critically controlled environment and expensive equipment. Full pose measurement of the EE is performed;

- Vision allows monitoring the pose of the end effector in motion provided that the image processing is fast enough;

- If two stationary cameras are used no calibration object is needed.

Outlook

Reduced motion robots, as witnessed implicitly by their very existence, carry out manipulation tasks, requiring fewer than 6 dof, more economically, efficiently and accurately than can general 6 dof robots. Similarly, it is claimed, a calibration set up and procedure specifically suited to, say, planar manipulators will yield the same advantages. This is particularly important because calibration, though often necessary, is inherently expensive

and time consuming. Moreover simplification of procedure and set up will, in the same way, inevitably improve accuracy of the calibration itself. Although restricted to a specific robot architecture, this article documents a case in point.

References

[1] Zhuang, H., Yan, J. and Masory, O.,"Calibration of Stewart platforms and other parallel manipulators by minimizing inverse kinematic residuals", *Robototic Systems*, Vol. 15, No. 7, pp. 395–405, 1998.

[2] Hollerbach, J., Khalil, W., Gautier, M., "Model Identification", *Springer Handbook of Robotics*, Chapter 14, Springer-Verlag Berlin Heidelberg, 2008.

[3] Zhuang, H., Roth, Z. S., *Camera-Aided Robot Calibration*, CRC Press, Inc., 1996.

[4] Motta, J., de Carvalho, G., McMaster, R. S., "Robot Calibration using a 3D vision-based measurement system with a single camera", *Robotics and Computer Integrated Manufacturing 17*, pp. 487–497, 2001.

[5] Connolly, C., "A new integrated robot vision system from FANUC Robotics", *Industrial Robot: An International Journal* , Emerald Group Publishing Limited, Vol. 34, No. 2, pp. 103-106, 2007.

[6] Connolly, C., "Vision enabled robotics", *Industrial Robot: An International Journal*, Emerald Group Publishing Limited, Vol. 32, No. 6, pp.456-459, 2005.

[7] Connolly, C., "Machine vision advances and applications", *Assembly Automation*, Emerald Group Publishing Limited, Vol. 29, No. 2, pp. 106-111, 2009.

[8] Bai, S. and Teo, M. Y., "Kinematic calibration and pose measurement of a medical parallel manipulator by optical position sensors", *Journal Robotic Systems*, Vol. 20, No. 4, pp. 201–209, 2003.

[9] Renaud, P., Andreff, N., Martinet, P., Gogu, G., "Kinematic calibration of parallel mechanisms: a novel approach using legs observation ", in *IEEE Transactions on Robotics*, Vol. 21, No. 4, pp. 529–538, 2005.

[10] Renaud, P., Andreff, N., Lavest, J. M., Dhome, M., "Simplifying the Kinematic Calibration of Parallel Mechanisms Using Vision-Based Metrology", in *IEEE Transactions on Robotics*, Vol. 22, No. 1, 2006.

[11] Zou, H., Notash, M., "Discussions on the camera-aided calibration of parallel manipulators", in *Proceedings of the 2001 CCToMM symposium on mechanisms, machines and mechatronic*, Saint Hubert, 2001.

[12] Chen, C., Zsombor-Murray, P. J., *"Direct Kinematic Mapping for All Planar Three-Legged Parallel Platforms"*, VDM Verlag Dr. Müller, ISBN 978–3–639–15037–7, pp.63, 2009.

[13] Daniali, H. R. M., Zsombor-Murray, P. J. and Angeles, J., "The Kinematics of 3-DOF Planar and Spherical Double-Triangular Parallel Manipulators", *Computational Kinematics*, J. Angeles et al., eds., Kluwer Academic Publishers, pp. 153-164., 1993.

[14] Tilton, N. G., "Projective Geometry and Planar Kinematic Mapping in Kinematic Analysis: The Kinematic Analysis of a Planar Double-Triangular Parallel Manipulator", B. Eng.(hons.), McGill University, 02–12, 2002.

[15] Neumayr, R., "Camera-Aided Robot Calibration of the Planar Double-Triangular Parallel Manipulator", Diplomarbeit, Institute for Automation, Montanuniversität Leoben, Austria, 2004.

[16] Yu, A., "Design and Analysis of Planar Parallel Three-Legged PRP Manipulators", M. Eng., McGill University, 09–05, 2005.

[17] Harker, M., O'Leary, P., "Computation of Homographies", *British Machine Vision Conference*, Vol. 1, pp. 310–319, 2005.

[18] Koller, N., "Fully Automated Repair of Surface Flaws using an Artificial Vision Guided Robotic Grinder", Doctoral Thesis, Institute for Automation, Montanuniversität Leoben, Austria, 2002.

[19] Hartley, R., Zisserman, *Multiple View Geometry in Computer Vision*, 2nd Edition, Cambridge University Press, 2003.

[20] Wampler, C., Hollerbach J. M. and Arai, T., "An Implicit Loop Method for Kinematic Calibration and its Application to closed-chain Mechanisms", *Transactions on Robotics and Automation*, Vol. 11, No. 5, pp.710-724, 1995.

2.5 Results and Conclusion

The combination of the proposed optical components with the employed image processing and mapping techniques have enabled the implementation of an accurate measurement system. This measurement instrument has been successfully tested for planar displacements on a planar parallel manipulator. It was demonstrated that such systems are easy to install and require no elaborate equipment nor environmental control. Furthermore, it was shown that a planar array of LED markers is an optimal calibration object to perform camera calibration yielding an accurate mapping. Sub-millimetre precision was achieved by employing image processing and rectification techniques with sub-pixel accuracy, 2.4.5. However, the employed camera calibration method assumes linearity in mapping and thus requires camera optics with negligible distortion. Systematic errors in the image caused by lens error or mechanical construction cannot be compensated with the homography. The accuracy of the system is determined by the individual accuracy of the optical component. Therefore, a new technique is presented in Chapter 3 that compensates such distortion effects and enables to use of, e.g., lenses of short focal length to design more compact systems at the same or higher accuracy.

Chapter 3

Product Development of an Active Laser Target Measurement Unit

This chapter deals with the design and production of optical components; calibration and evaluation procedures; thermally stable housings; all of which are required for the implementation of accurate optical displacement and orientation sensors.
The company GEODATA [11] initiated the idea to develop a vision based measurement unit that determines position (x, y, z) and orientation (roll (ϕ_1), pitch (ϕ_2) and yaw (ϕ_3)) of an object using an off-vehicle reference laser beam. This unit should be rigidly fixed on a tunnel boring machine (TBM) to enable active guidance control to minimize deviations on the desired path. As the environmental conditions in mining and tunnelling are very extreme this measurement device should be resistant against water, dust, high temperature gradients [26] and strong vibrations.
A brief overview of this chapter is given below describing the development steps from brainstorming to a finished prototype:

1. State of the art, specification and requirement analysis;
2. Develop a concept, choose the most suitable and define principle of operation;
3. Selection, evaluation and testing of the following optical components in a laboratory setup:
   - Semi-reflective target;
   - Camera and lens;
   - Test results of evaluation to determine most suitable components to fullfill accuracy and reproducibility;
4. Housing;
5. System calibration;
6. Testing the complete device on accuracy and reproducibility.

As a vision based approach was chosen the focus of development lies especially on the optimum configuration of the optical components and on the efficiency and accuracy of the image processing algorithms.

Fig. 3.1: Front of a Tunnel Boring Machine (TBM), [27].

3.1 State of the Art

Tunnel boring machine guidance control with an active laser target (ALT) unit has existed for decades [14], see Fig. 3.2. In the early stages the laser spots on the targets are measured with another external system or are simply monitored by the operators human eye. In many cases the machine had to stop to obtain accurate measurement results. This is a significant cost factor.
The advantage of a vision based active laser target (ALT) unit is that it delivers accurate position and orientation measurements of the machine in real time to compensate and minimize deviations on the desired path while the machine is in operation. Vision based ALT units are already provided by [12], however, in this system only the yaw angle is obtained by vision based components. The company "tacs" [13] developed a unit that is based on the same principle but providing systems of larger size compared to the instrument presented herein. Both available systems are based on the traditional pinhole camera model [17] and thus require high quality camera optics.
Objectives in this prototype development were to keep the dimensions of this measurement unit as compact as possible to employ such units in machines where installation space is scarce while maintaining the required accuracy. This implies the use of micro-lenses with short focal length that enable a larger field of view but usually produce significant image distortion; specifically fisheye effects. Therefore a new mathematical approach for calibration is introduced called bivariate polynomial tensor approximation that models the nonlinear distortion effects yielding an accurate mapping.

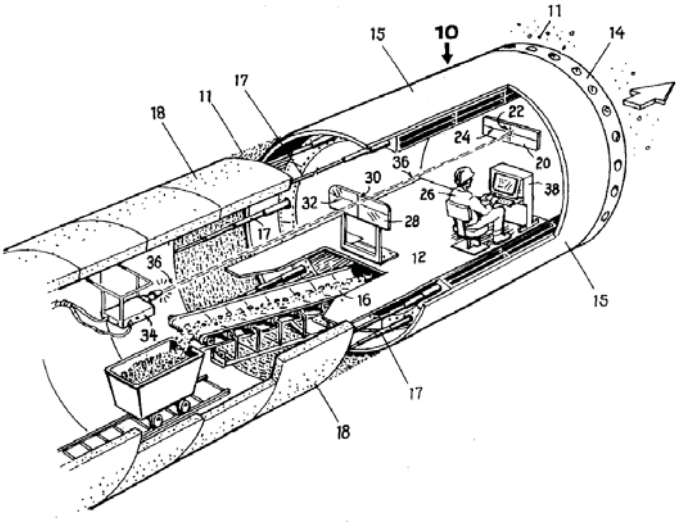

Fig. 3.2: Figure from a patent [14] showing principle of operation of optical active laser target guidance control. A programmable off-vehicle theodolite (34) projects its reference laser beam on to parallel targets (28) and (20) that are rigidly fixed on the TBM (15) whereby the first target is semi-transparent. The positions of the laser spots (30), (22) on the targets are monitored by the operator to control the desired path.

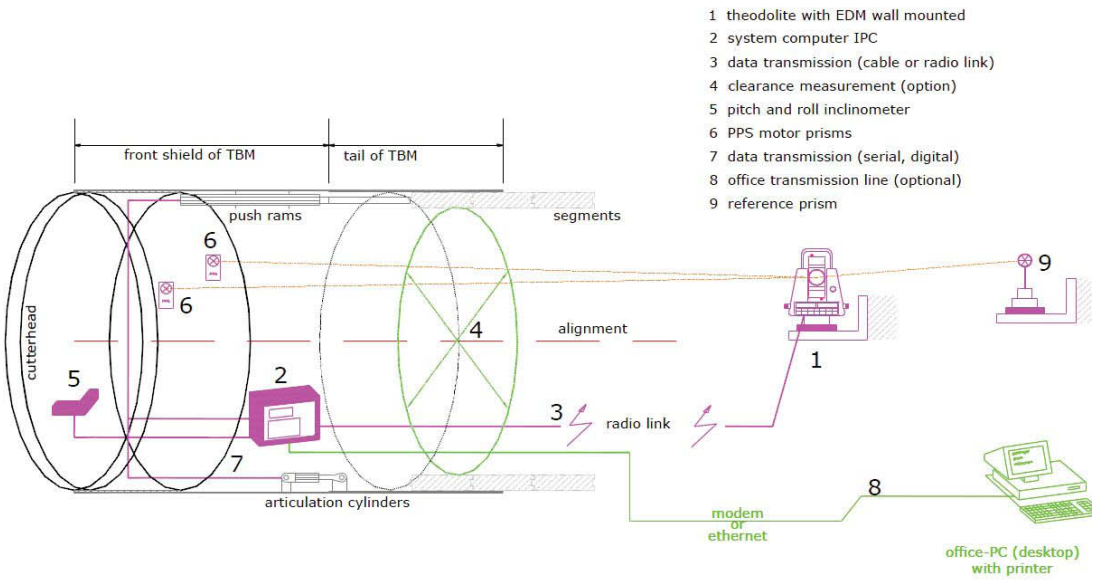

Fig. 3.3: Alternative principle of operation [15] of TBM guidance control. A programmable off-vehicle theodolite (1) is aligned to two prisms (6) that are installed on the machine to measure the position. Inclinometers (5) provide pitch and yaw data.

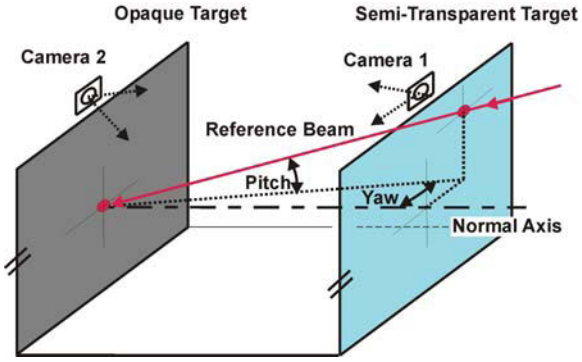

Figure 3.4: Principle of operation of ALT: A reference laser beam penetrates a semi-transparent window, and illuminates a spot on a second target. Pitch, yaw and displacement is computed from the positions of the two points of penetration.

3.2 Principle of Operation

The following configuration of the optical components shown in Fig. 3.4 has been determined to be the most suitable.
A reference beam is projected from a programmable theodolite total station [6]. The beam enters the housing at a semi-transparent window. The pattern printed on the inside of the window scatters a portion of the light making the point of penetration visible. The transmission portion of the beam illuminates a spot on the opaque target within the housing. The spots on the windows and the inner target are imaged by two CMOS cameras within the housing. An optical interference filter, matched to the wavelength of the laser, is mounted in front of the lens of the cameras. This suppresses the predominant portion of the ambient light. The position of the laser points in pixel coordinates are mapped to real world coordinates using a bivariate tensor polynomial for both x and y-coordinates. This performs inversion of the projections associated with the relative positions of the cameras to the targets, while simultaneously correcting for distortions in the optical path; and errors in the mechanical construction.

3.2.1 Estimation of Required Accuracy for Displacement Measurement

From the preliminary specification data, see Appendix A.1, an estimation subject to the required accuracy of displacement and position of the laser spot is computed using the Monte Carlo method. The target distance is 280 [mm], the specified accuracy of angle measurement (pitch, yaw) is ± 0.05 [degree]. It is assumed that the displacement measurements are perturbed with independently and identically distributed Gaussian noise of $\sigma_d = 0.1$ [mm]. The resulting distribution of angle accuracy employing Monte Carlo simulation with 10 000 iterations is shown in Fig. 3.5. The computed angle accuracy of pitch and yaw is $\sigma_a = 0.0288$ [degree], i.e., $\approx 95\%$ of the measurements are within the required accuracy. This estimation of displacement accuracy is considered a sufficient base for evaluation and selection of the optical components.

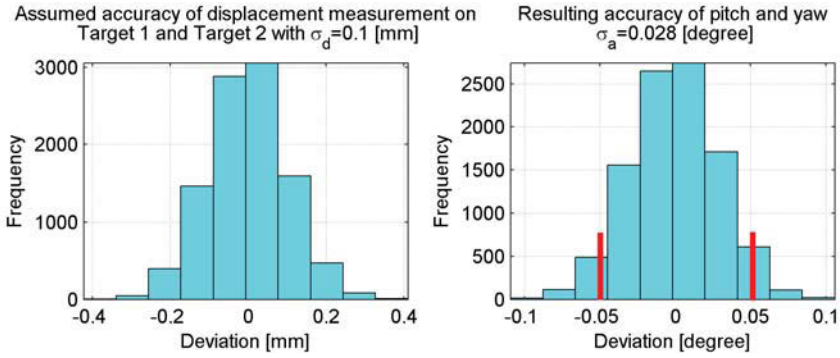

Fig. 3.5: Estimated accuracy of pitch and yaw assuming a measured displacement accuracy of the the laser spot of $\sigma_d = 0.1$ [mm]. Required angle accuracy ± 0.05 [degree].

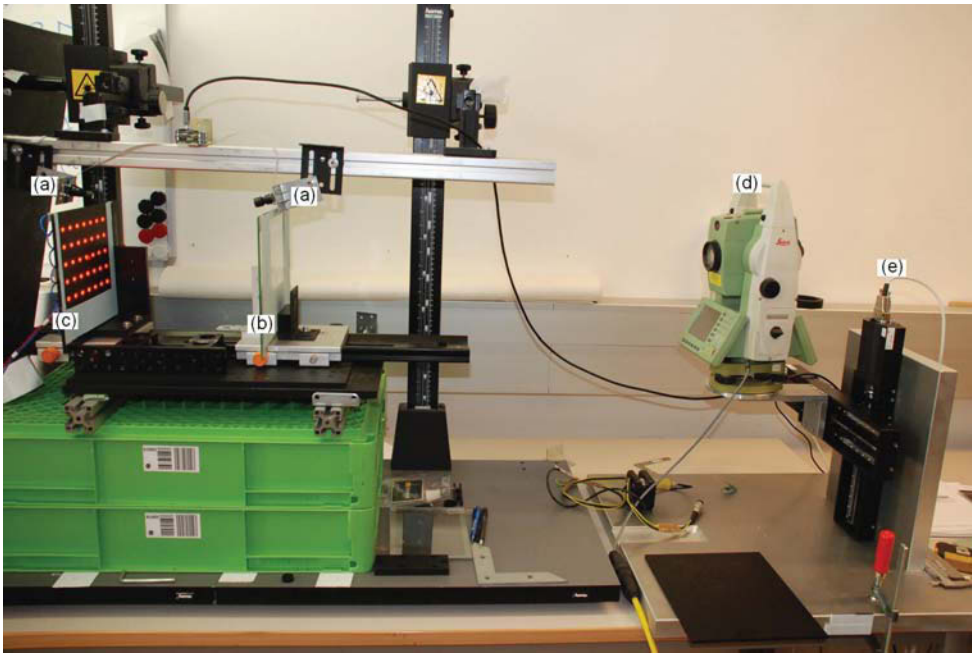

Figure 3.6: Laboratory setup, (a) VR-Magic camera [20], (b) semi-reflective target, (c) solid target with array of flat headed LEDs, (d) theodolite, (e) xy-table with linear drives.

3.3 Optical Components

The optical components were evaluated in a laboratory setup that enables quick exchange of different component samples, see Appendix A.2 and Fig. 3.6.

3.3.1 Semi-Transparent Target

The semi-transparent window is manufactured by printing a dot-pattern onto a glass plate. Because tunneling conditions are harsh different printing technologies were investigated to fulfill the following requirements: Resistance to mechanical loads; resistance to

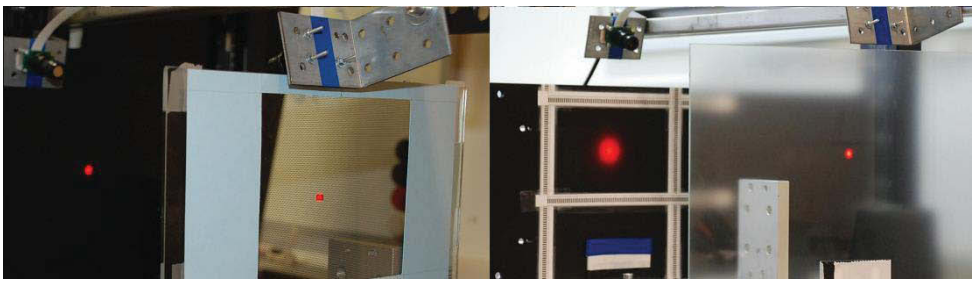

Figure 3.7: Testing semi-reflective target with hexagonal dot-pattern (left) and surface processed “milky” (Appendix A.2) glass (right). Note the diffusion of the laser beam resulting in a larger, blurry laser spot on the second target.

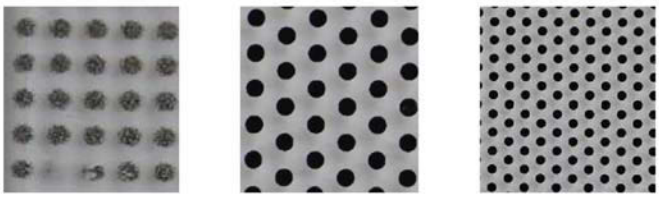

Figure 3.8: Digital print (left) vs. screen printing (middle) dot-diameter= 0.8 [mm] and screen printing dot-diameter= 0.5 [mm] (right); ink of digital print chipped off the glass when subjected to small mechanical load. Note the degradation of the direct digital printing on the left.

Dot-Pattern	Dot-Diameter	Dot-Distance	STD Displacement Accuracy	STD Positional Reproducibility
Orthogonal (digital print)	1.0 [mm]	2.0 [mm]	$\sigma_{d1} = 0.5081$ [mm]	$\sigma_{x1} = 0.2129$ [mm] $\sigma_{y1} = 0.2024$ [mm]
Hexagonal (screen printing)	0.8 [mm]	1.6 [mm]	$\sigma_{d2} = 0.1045$ [mm]	$\sigma_{x2} = 0.0268$ [mm] $\sigma_{y2} = 0.0395$ [mm]
Hexagonal (screen printing)	0.5 [mm]	1.0 [mm]	$\sigma_{d3} = 0.0493$ [mm]	$\sigma_{x3} = 0.0041$ [mm] $\sigma_{y3} = 0.0039$ [mm]
Opaque Target	-	-	$\sigma_{d,r}$ =0.01899 [mm]	-

Table 3.1: Evaluation of dot-pattern on semi-reflective target performing 50 independent displacements with laser beam over whole target. Displacement accuracy on opaque, rear target when using hexagonal dot-pattern with dot-diameter= 0.5 [mm].

temperature-gradients; good adhesion to glass; high printing resolution. The dot-pattern needs to balance the percentage of light scattered and transmitted, since this determines the visibility of the laser spots on both targets. The pattern should enable an optimal statistical estimation of the position of the point of the reference laser beam. Rectangular and hexagonal patterns were investigated, see Fig. 3.9 and Fig. 3.10. The hexagonal pattern demonstrated a more regular and almost omni-directional scattering of the laser beam, see Fig. 3.11; this was considered to be statistically more desirable. The printing technique used also has a strong influence on the quality of the pattern and its mechanical properties. Direct digital printing was compared with screen printing, see Fig. 3.8. Even under laboratory conditions the direct digital printing pattern was subject to serious degradation. Furthermore, a higher contrast is achieved with screen printing. Finally a hexagonal pattern with dots of radius 0.5 [mm] and a spacing of 1 [mm] was selected, Fig. 3.11.

Alternatives such as special coatings on glass or surface processed glass yield diffusion of the laser beam resulting in a larger, blurry laser spot on the second target, see Fig. 3.7.

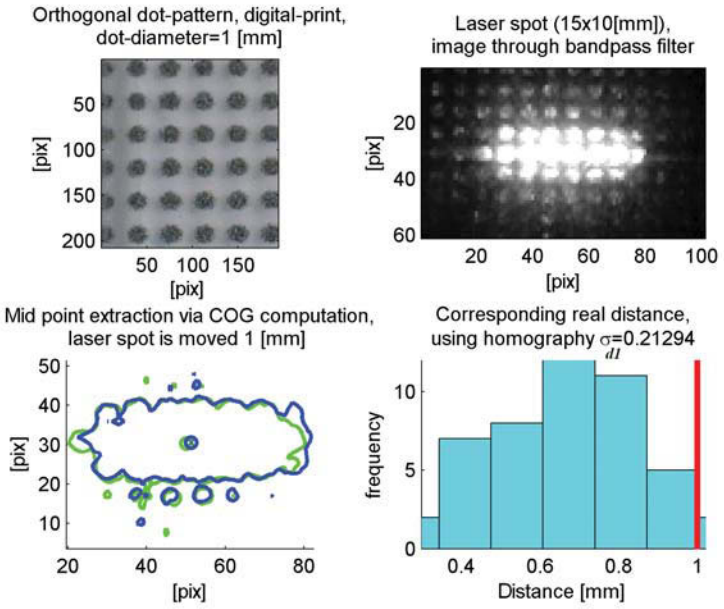

Figure 3.9: Orthogonal dot-pattern with dot-diameter= 1 [mm]; image of the laser spot; extracted contour of the spot and the estimated position; histogram of the computed displacement errors for 50 independent measurements.

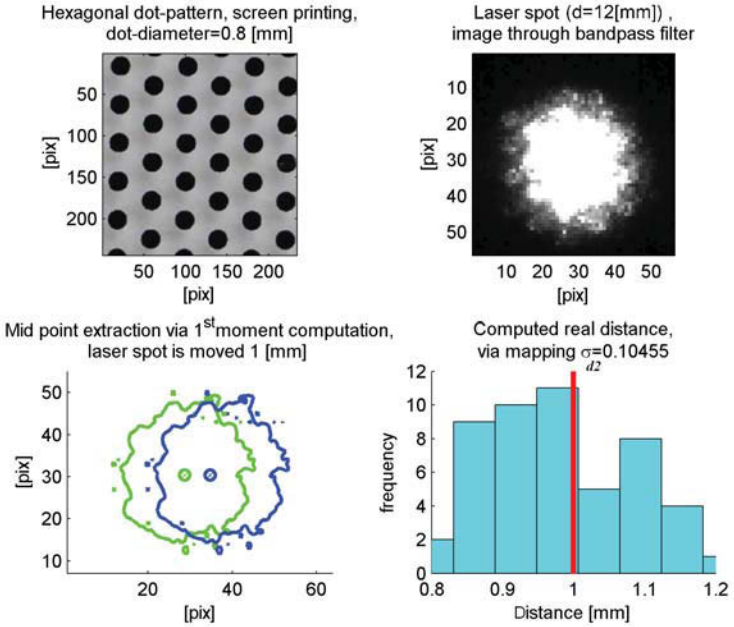

Figure 3.10: Hexagonal dot-pattern with dot-diameter= 0.8 [mm]; image of the laser spot; extracted contour of the spot and the estimated position; histogram of the computed displacement errors for 50 independent measurements.

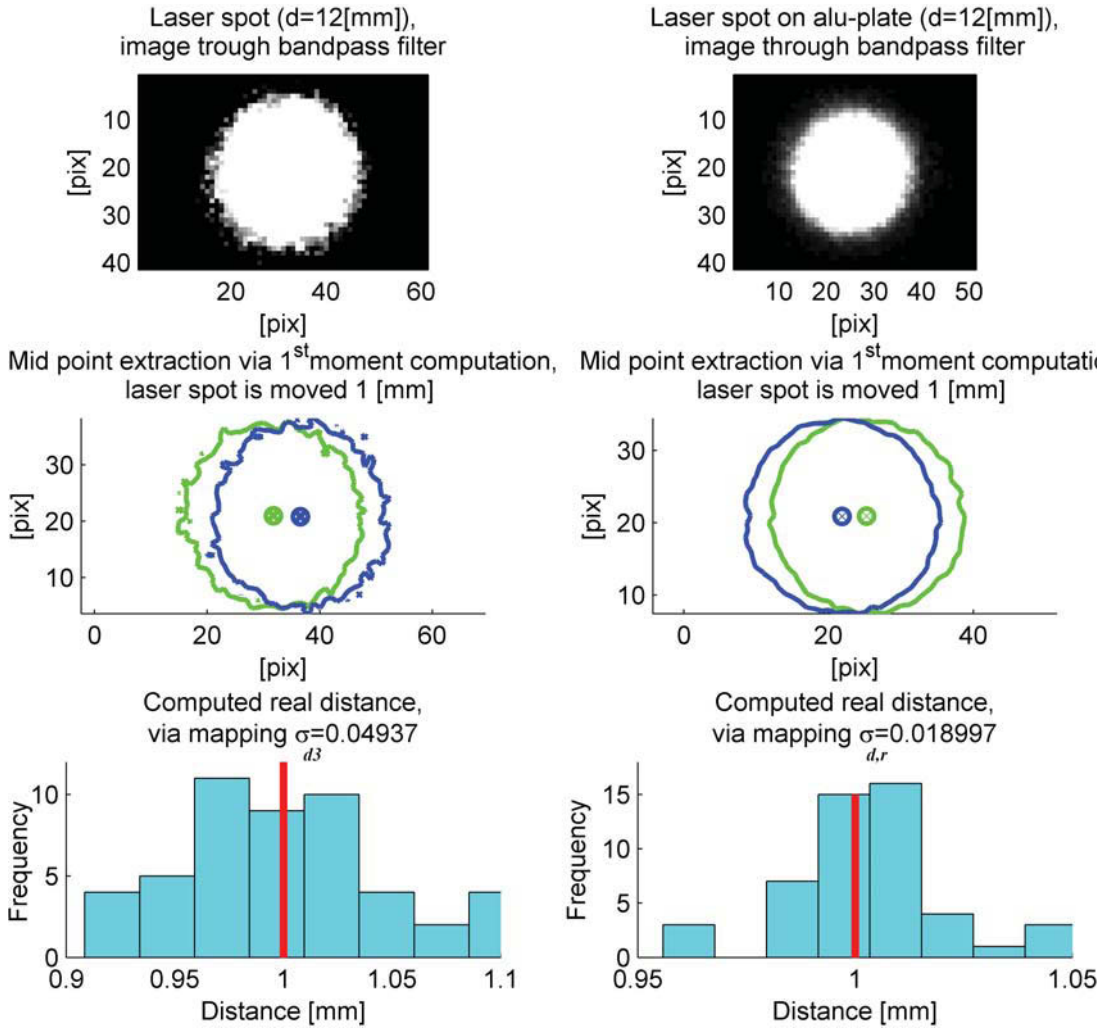

Figure 3.11: Image of the laser spot; extracted contour of the spot and the estimated position; histogram of the computed displacement errors for 50 independent measurements. These results are obtained with the hexagonal dot pattern (dot-diameter= 0.5 [mm], Fig. 3.8, right) on the semi-transparent window. The results for the front target are shown on the left, and for the rear target on the right. Note the better quality of the image on the rear target.

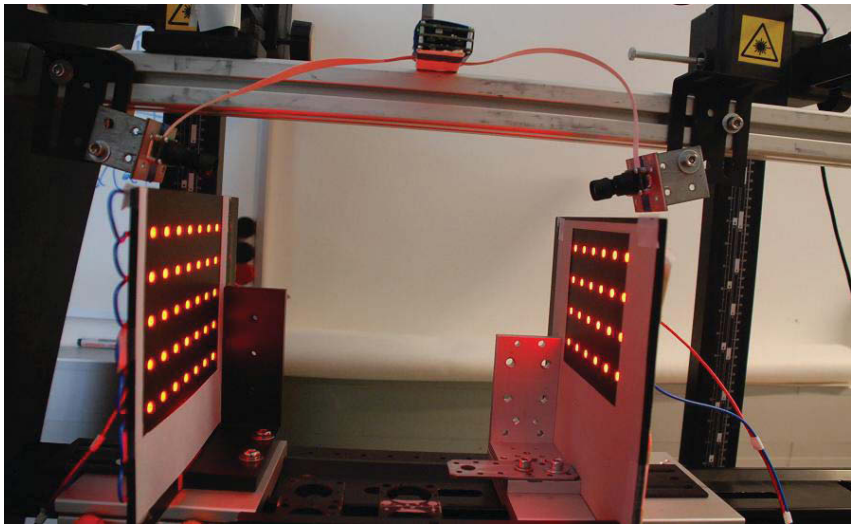

Figure 3.12: Lens evaluation by imaging a flat aluminium target with a precisely pre-known regular grid of LEDs.

This effect makes a robust position estimation of the spot more difficult. Furthermore, the larger diameter of the spot restricts the maximum ranges of angle measurements.

3.3.2 Camera and Lens Selection

Conventionally, a homography [17] is used to map the pixel coordinates to real world coordinates. In such approaches the accuracy of the measurement system is limited by the errors in the optical components. In particular the distortion associated with the lens has had a dominant effect on the obtainable accuracy. In the design of this device a tensor polynomial input-output model is used which can also correct for distortion in the optical components. Consequently, a micro-lens with focal length 5.7 [mm] can be used despite the strong fish-eye distortion. The suitability of the lens, combined with the new bivariate tensor polynomial model was tested by imaging a flat aluminium target with a regular grid of 7×5 LEDs. The image was taken with a micro lens f=5.7 [mm] at a distance 250 [mm].
A low resolution CMOS camera (764×480 [pix]) with a digital interface [20] was employed yielding a physical resolution of 0.2 [mm]/[pix]. Consequently, this configuration requires sub-pixel image processing- and mapping techniques. The acquired image, with visible fish-eye distortion, is shown in Fig. 3.13, together with the comparison of the positional errors obtained using a conventional homography and the new modelling approach. The positional error in this case is defined as the Euclidean error,

$$e_i = |\boldsymbol{p}_i - \boldsymbol{q}_i| = \sqrt{(P_{x,i} - Q_{x,i})^2 + (P_{y,i} - Q_{y,i})^2} \triangleq \sqrt{\Delta x_i^2 + \Delta y_i^2} \tag{3.1}$$

where $\boldsymbol{p}_i$ are the pre-known real-world positions of the LEDs and $\boldsymbol{q}_i$ are the computed real world positions obtained by conventional homography or the new modelling approach. The average positional error obtained with the bivariate tensor polynomial was $\bar{e}_{p3} = 0.0218$

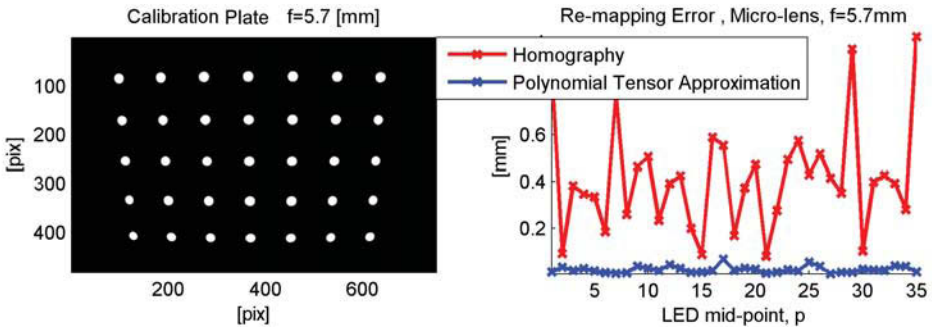

Figure 3.13: Test image (left) and associated calibration errors (right). A flat aluminium target with a regular grid of 7×5 LEDs was used during this test. The image (left) is taken with a micro lens f=5.7 [mm] at a distance 250 [mm]. The errors e_i (Eq. 3.1) after re-mapping the imaged points to the known positions are shown on the right. The results of re-mapping with a homography are compared with those from the bivariate tensor polynomial approximation with Gram bases functions of degree $d_x = d_y = 3$.

[mm], as shown in Fig. 3.13 and Table 3.2. This is an order of magnitude better than the specification and is therefore quite accetable. For completeness: The new mapping method is applied to another two calibration images that are acquired with a high quality lens (f = 12 [mm], distance=450 [mm]), Fig. 3.14, and a micro lens (f = 3.6 [mm], distance=180 [mm]). In both cases significant improvement of the mapping accuracy compared to the homography method is achieved. Even at significant distortion (f = 3.6 [mm], Fig. 3.15) the new method provides precise mapping. The results are summarized in Table 3.2.

3.3.3 Spot Position Evaluation

Sufficient camera resolution and image quality of the laser spot were established statistically by performing translational movements of a laser spot with a calibrated xy-table (resolution: 6 [μm]/[inc]), see Fig. 3.6. The first moment of intensity [7] is computed as an estimate of the position of the laser spot. Fig. 3.9 shows a typical image of the laser spot on the front target with the orthogonal pattern; the contours of the laser spots and the positions of the first moment of intensity computed in the x and y directions; together with the histograms of the computed displacement errors for 50 independent measurements. As expected, the orthogonal dot-pattern provides very inaccurate measurements whereas the hexagonal dot-pattern with 0.8 [mm] dot-diameter, as shown in Fig. 3.10, yields a significant improvement of displacement accuracy with $\sigma_{d2} = 0.10455$ [mm]. Figure 3.11 shows a typical image of the laser spot on the front and rear targets obtained by the hexagonal dot-pattern with 0.5 [mm] dot-diameter. The standard deviation of the computed displacement errors for 50 independent measurements is $\sigma_{d3} = 0.04937$ [mm] and on the rear target $\sigma_{d,r} = 0.018997$ [mm]. This measurement indicates that there may be some room for improvement by optimizing the dot-pattern, some degradation of the rear image can be tolerated if the computation statistics for the front target can be improved. The results of the displacement measurements dependent on the dot-pattern are

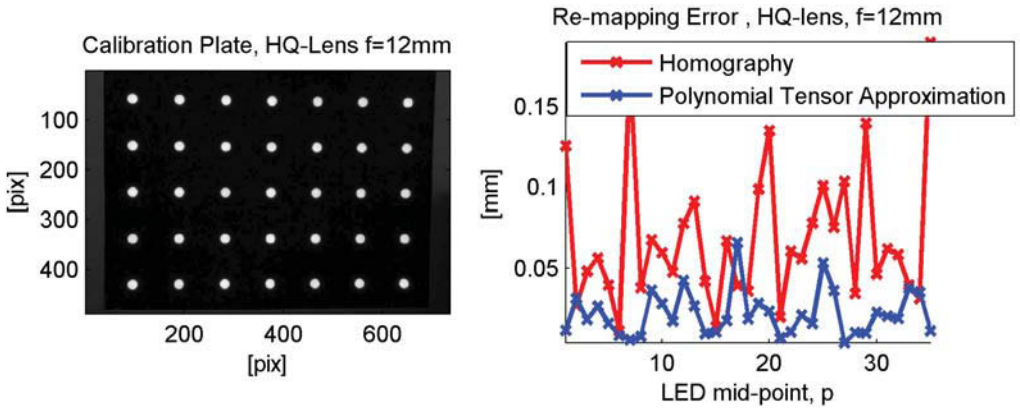

Figure 3.14: Test image (left) and associated calibration errors (right). The image (left) is taken with a high quality lens, Appendix A.2, f=12 [mm] at a distance 450 [mm]. The errors e_i (Eq. 3.1) after re-mapping the imaged points to the known positions are shown on the right. The results of re-mapping with a homography are compared with those from the bivariate tensor polynomial approximation with Gram bases functions of degree $d_x = d_y = 3$.

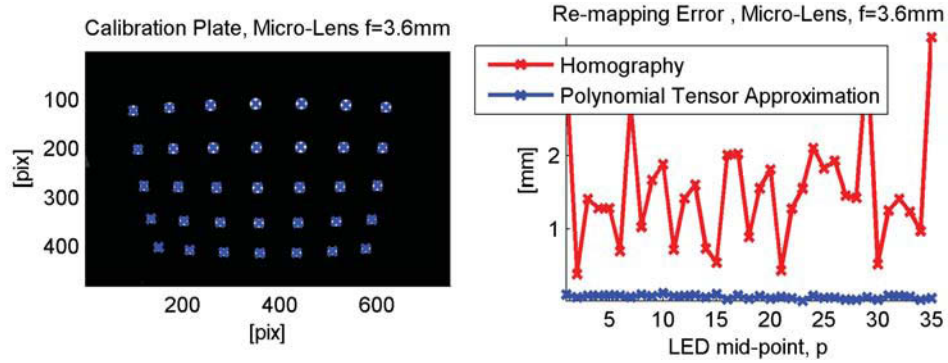

Figure 3.15: Test image (left) and associated calibration errors (right). The image is taken with a micro lens f=3.6 [mm] at a distance 180 [mm], note the significant fisheye effect. Tensor polynomial approximation with Gram bases functions of degree $d_x = d_y = 3$.

Lens	Focal Length	Average ($\bar{e}_i$) Positional Error Homography	Average ($\bar{e}_i$) Positional Error Bivariate Tensor Polynomial
High Quality Cosmicar	$f = 12.0$ [mm]	$\bar{e}_{h1} = 0.0682$ [mm]	$\bar{e}_{p1} = 0.0212$ [mm]
Micro-Lens VR-Magic	$f = 8.0$ [mm]	$\bar{e}_{h2} = 0.1921$ [mm]	$\bar{e}_{p2} = 0.0217$ [mm]
Micro-Lens VR-Magic	$f = 5.7$ [mm]	$\bar{e}_{h3} = 0.4130$ [mm]	$\bar{e}_{p3} = 0.0218$ [mm]
Micro-Lens VR-Magic	$f = 3.6$ [mm]	$\bar{e}_{h4} = 1.5197$ [mm]	$\bar{e}_{p4} = 0.0665$ [mm]

Lens	Focal Length	STD (e_i) Positional Error Homography	STD (e_i) Positional Error Bivariate Tensor Polynomial
High Quality Cosmicar	$f = 12.0$ [mm]	$\sigma_{h1} = 0.0428$ [mm]	$\sigma_{p1} = 0.0139$ [mm]
Micro-Lens VR-Magic	$f = 8.0$ [mm]	$\sigma_{h2} = 0.1067$ [mm]	$\sigma_{p2} = 0.0146$ [mm]
Micro-Lens VR-Magic	$f = 5.7$ [mm]	$\sigma_{h3} = 0.2327$ [mm]	$\sigma_{p3} = 0.0140$ [mm]
Micro-Lens VR-Magic	$f = 3.6$ [mm]	$\sigma_{h4} = 0.7827$ [mm]	$\sigma_{p4} = 0.0250$ [mm]

Table 3.2: Evaluation of accuracy of mapping method subject to lenses of increasing shorter focal length (Appendix A.3) by imaging a flat aluminum target with a regular grid of LEDs, see Fig. 3.13 (left). The extracted positions of the LEDs in the image are re-mapped to their real world coordinates to compute the positional error e_i (Eq. 3.1) subject to the pre-known positions of LEDs, Fig. 3.13 (right). The results of re-mapping with a homography are compared with those from the bivariate tensor polynomial approximation with Gram bases functions of degree $d_x = d_y = 3$.

summarized in Table 3.1.

3.3.4 Opaque Target

The second target is a simple anodized black aluminum plate. For calibration reasons the plate is equipped with a grid of precisely located flat-headed LEDs. This so called calibration object is used to:

- Evaluate lens distortion and fish-eye effects of camera lenses, see Fig. 3.13;
- Perform camera calibration to evaluate accuracy of transformation methods, see Section 3.3.2;
- Evaluate the accuracy of the homography or alternative transformation methods, see Section 3.3.2;
- Perform reference measurements to check the laser spots position, as positions of LEDs are pre-known.

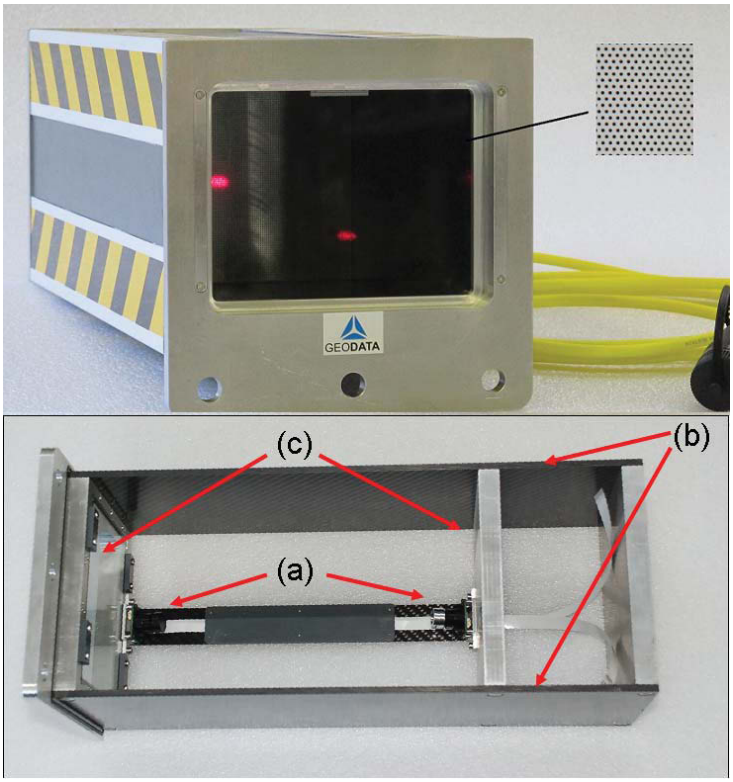

Figure 3.16: Top: ALT Prototype with zoomed dot-pattern on semi-transparent target. (Photograph by Geodata GmbH [11]). Bottom: A Kevlar49® (b) fixes the positions of the cameras (a) and the targets (c).

3.4 Housing and Prototype

The influence of thermal expansion on the accuracy of this unit was estimated with respect to the target distance. The results show that an aluminum frame would undergo a significant thermal expansion under a temperature change of the order of 50 [C], see Fig. 3.17. Consequently, a double housing was designed where a Kevlar49® [22] frame is used internally to fix the positions of the cameras and the targets. Kevlar with a weaving pattern which exhibits a very low thermal coefficient of expansion was chosen. Additionally a series of 6 LEDs with known positions are located in the frame surrounding each target. These LEDs can be activated and their positions measured, prior to a laser measurement, the measured positions should be invariant. The LED calibration arrays are checked regularly to verify dimensional stability of camera and target positions.

The overall compact dimensions of this box are $(l \times w \times h)$ 430×160×140 [mm] where the target measurement area is 140×110 [mm] at a target distance of 280 [mm], Fig. 3.16. A prototype software has been programmed providing a stand alone application to operate on windows based PC, see Appendix A.4.

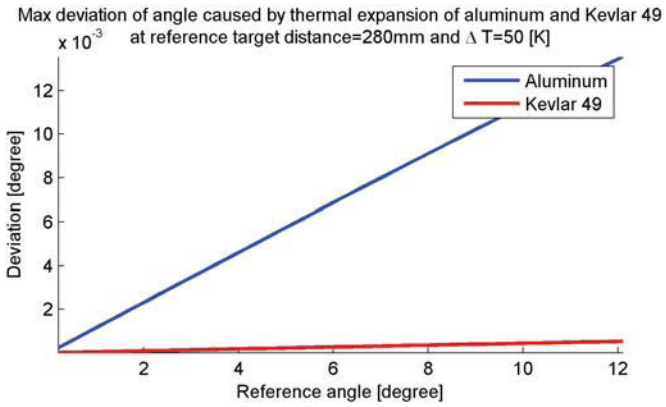

Figure 3.17: Influence of thermal expansion of aluminum and Kevlar49® [22] on the accuracy at target distance 280 [mm] and △T=50 [C]. Required angle accuracy in this application: ±0.05 [degree].

3.5 System Calibration

As lenses with significant image distortion are used a coordinate transformation method based on polynomial basis functions [10] is employed to model the nonlinear distortion.

Theoretical Framework

3.5.1 Polynomial Regression - Univariate Polynomial Basis

Polynomial Regression is a good starting point to understand approximation via basis functions. Given a set of n data points $\boldsymbol{p}_i = [x_i, y_i]$ that is perturbed by independent identically distributed Gaussian noise, these points can be approximated by a sum of monomials of degree d, i.e.,

$$\tilde{y} = a_0 + a_1 x + a_2 x^2 \ldots + a_d x^d = \sum_{i=0}^{d} a_i x^i. \tag{3.2}$$

The remaining residual r_i of this approximation subject to the data points y_i is consequently

$$r_i = y_i - \tilde{y} = y_i - \sum_{i=0}^{d} a_i x^i. \tag{3.3}$$

These equations assume no x-coordinate data errors. Translating these equations into matrix form yields,

$$\begin{bmatrix} r_1 \\ \vdots \\ r_n \end{bmatrix} = \begin{bmatrix} y_1 \\ \vdots \\ y_n \end{bmatrix} - \begin{bmatrix} 1 & x_1 & x_1^2 & \ldots & x_1^d \\ \vdots & \vdots & \vdots & \vdots & \vdots \\ 1 & x_n & x_n^2 & \ldots & x_n^d \end{bmatrix} = \begin{bmatrix} a_0 \\ a_1 \\ \vdots \\ a_n \end{bmatrix} \quad \text{or} \quad \boldsymbol{r} = \boldsymbol{y} - \mathsf{B}\boldsymbol{s}, \tag{3.4}$$

where B is called the design matrix and $\boldsymbol{s}$, known as the spectrum, contains the corresponding coefficients.
The error function E can now be formulated as:

$$E = \sum_{i=1}^{n} r_i^2, \tag{3.5}$$

$$= \boldsymbol{r}^T \boldsymbol{r}, \tag{3.6}$$

$$= (\boldsymbol{y} - \mathsf{B}\boldsymbol{s})^T (\boldsymbol{y} - \mathsf{B}\,\boldsymbol{s}). \tag{3.7}$$

The minimum is found by setting the first partial derivative of E with respect to $\boldsymbol{s}$ equal to zero,

$$\min_{\boldsymbol{v}} E \Rightarrow \frac{\partial E}{\partial \boldsymbol{s}} = 0. \tag{3.8}$$

Expanding the Eq. 3.7,

$$E = (\boldsymbol{y} - \mathsf{B}\,\boldsymbol{s})^T\,(\boldsymbol{y} - \mathsf{B}\,\boldsymbol{s}), \tag{3.9}$$
$$= \boldsymbol{y}^T\,\boldsymbol{y} - \boldsymbol{s}^T\,\mathsf{B}^T\,\boldsymbol{y} - \boldsymbol{y}^T\,\mathsf{B}\,\boldsymbol{s} + \boldsymbol{s}^T\,\mathsf{B}^T\,\mathsf{B}\,\boldsymbol{s}, \tag{3.10}$$
$$= \boldsymbol{y}^T\,\boldsymbol{y} - 2\,\boldsymbol{s}^T\,\mathsf{B}^T\,\boldsymbol{y} + \boldsymbol{s}^T\,\mathsf{B}^T\,\mathsf{B}\,\boldsymbol{s}. \tag{3.11}$$

Evaluating the differential

$$-2\,\mathsf{B}^T\,\boldsymbol{y} + 2\,\mathsf{B}^T\,\mathsf{B}\,\boldsymbol{s} = 0 \tag{3.12}$$
$$\mathsf{B}^T\,\mathsf{B}\,\boldsymbol{s} = \mathsf{B}^T\,\boldsymbol{y}. \tag{3.13}$$

Solving for $\boldsymbol{s}$ delivers the desired minimum. Pre-multiplying by $(\mathsf{B}^T\,\mathsf{B})^{-1}$

$$(\mathsf{B}^T\,\mathsf{B})^{-1}\,\mathsf{B}^T\,\mathsf{B}\,\boldsymbol{s} = (\mathsf{B}^T\,\mathsf{B})^{-1}\,\mathsf{B}^T\,\boldsymbol{y}. \tag{3.14}$$

This simplifies to

$$\boldsymbol{s} = (\mathsf{B}^T\,\mathsf{B})^{-1}\,\mathsf{B}^T\,\boldsymbol{y} \tag{3.15}$$
$$= \mathsf{B}^+\,\boldsymbol{y}. \tag{3.16}$$

The term $\mathsf{B}^+ \triangleq (\mathsf{B}^T\,\mathsf{B})^{-1}\,\mathsf{B}^T$ is called the pseudo-inverse. It is the inverse of a rectangular matrix in a least mean square sense.
The estimated values $\tilde{\boldsymbol{y}}$ can now be simply computed

$$\tilde{\boldsymbol{y}} = \mathsf{B}\mathsf{B}^+\boldsymbol{s}. \tag{3.17}$$

This simple algebraic approach shows some of the fundamental algebraic structure associated with approximation with basis functions.
In this case the design matrix B is called the Vandermonde matrix that unfortunately becomes numerically degenerate as the degree of the polynomial increases. Consequently the Vandermonde polynomials are not suitable basis functions when solving large scale problems. However, this problem can be solved by employing unitary respectively orthonormal basis function, e.g., Gram polynomials where $\mathsf{B}^+ = \mathsf{B}^T$. Hence, Eq. 3.17 simplifies to

$$\tilde{\boldsymbol{y}} = \mathsf{B}\mathsf{B}^T\boldsymbol{s}. \tag{3.18}$$

3.5.2 Discrete Orthonormal Polynomials

Gram Basis

Gram [18] introduced the concept of a unitary polynomial basis and their application to least squares approximation. The polynomials were synthesized via a three term relationship in a process which is called a Gram-Schmidt orthogonalization.

$$g_n(x) = 2\;\alpha_{n-1}\;x\;g_{n-1}(x) - \frac{\alpha_{n-1}}{\alpha_{n-2}}\;g_{n-2}(x) \tag{3.19}$$

whereby,

$$\alpha_{n-1} = \frac{m}{n} \, (\frac{n^2 - \frac{1}{2}}{m^2 - n^2})^{\frac{1}{2}} \tag{3.20}$$

and

$$g_0(x) = 1, \quad g_{-1}(x) = 0 \quad \text{and} \quad \alpha_{-1} = 1, \tag{3.21}$$

x is computed on equidistance points,

$$x = -1 + \frac{2k-1}{m}, \quad 1 \leq k \leq m, \tag{3.22}$$

Note, that these points do not span the full range $[-1, 1]$. The bases functions are scaled by $\sqrt{m}$ yielding a unitary bases set.

3.5.3 Bivariate Polynomial Basis

Given a data set Z with its entries $z(i, j)$ that lie on a invariant Cartesian grid $\mathsf{G}(i, j)$, also called a "uniform" lattice, the spectrum can be computed

$$\mathsf{S} = \mathsf{B}_y^+ \mathsf{Z} (\mathsf{B}_x^+)^T. \tag{3.23}$$

The matrices B_x and B_y contain the basis function of degree d_x and d_y in the x and y-directions respectively. Two dimensional synthesis is computed as,

$$\tilde{\mathsf{Z}} = \mathsf{B}_y \mathsf{S} \mathsf{B}_x^T. \tag{3.24}$$

Given a spectra S the approximation errors over the Cartesian grid are

$$\mathsf{R} = \mathsf{Z} - \mathsf{B}_y \mathsf{S} \mathsf{B}_x^T. \tag{3.25}$$

As we wish to determine the spectrum we employ least-squares approximation and formulate the cost function

$$E = \sum_{i=1}^{n_x} \sum_{j=1}^{n_y} \mathsf{R}(i, j)^2 = \|\mathsf{B}_y \mathsf{S} \mathsf{B}_x^T - \mathsf{Z}\|_F^2. \tag{3.26}$$

Evaluating the Frobenius norm yields,

$$E = \text{trace}\{(\mathsf{B}_y \mathsf{S} \mathsf{B}_x^T - \mathsf{Z})(\mathsf{B}_y \mathsf{S} \mathsf{B}_x^T - \mathsf{Z})^T\}. \tag{3.27}$$

Differentiating the cost-function with respect to S and setting it equal to zero gives the equation,

$$\frac{\partial E}{\partial \mathsf{S}} = 2(\mathsf{B}_y^T \mathsf{B}_y \mathsf{S} \mathsf{B}_x^T \mathsf{B}_x - \mathsf{B}_y^T \mathsf{Z} \mathsf{B}_x) = 0 \tag{3.28}$$

and it follows that

$$\mathsf{S} = (\mathsf{B}_y^T \mathsf{B}_y)^{-1} \mathsf{B}_y^T \mathsf{Z} \mathsf{B}_x (\mathsf{B}_x^T \mathsf{B}_x)^{-1}. \tag{3.29}$$

As the Moore-Penrose pseudo-inverse of an Matrix A is defined as $\mathsf{A}^+ = (\mathsf{A}^T \mathsf{A})^{-1}) \mathsf{A}^T$, Eq. 3.29 simplifies to

$$\mathsf{S} = (\mathsf{B}_y)^+ \mathsf{Z} (\mathsf{B}_x^+)^T. \tag{3.30}$$

Therefore, the surface approximation can be synthesized, i.e., the values of the approximating surface at all points on the Cartesian Grid are

$$\tilde{\mathsf{Z}} = \mathsf{B}_y \mathsf{B}_y^{+} \mathsf{Z} (\mathsf{B}_x \mathsf{B}_x^{+})^T. \tag{3.31}$$

In the case of a unitary polynomial basis, $\mathsf{B}^{+} = \mathsf{B}^{\mathsf{T}}$, the reconstruction process becomes,

$$\tilde{\mathsf{Z}} = \mathsf{B}_y \mathsf{B}_y^T \mathsf{Z} \mathsf{B}_x \mathsf{B}_x^T. \tag{3.32}$$

This is a very efficient numerical solution and is a further justification for using the unitary polynomial basis, e.g., the Gram polynomial basis functions.

3.5.4 Discrete 2D Coordinate Transformations

The calibration of an image which is subject to nonlinear distortion can be accomplished by means of a general coordinate transformation, of the form,

$$\tilde{x} = \tilde{x}\,(x, y) \quad \text{and} \quad \tilde{y} = \tilde{y}\,(x, y)\,. \tag{3.33}$$

In the discrete case, the transformation can be modelled as a sum of discrete basis functions (e.g., polynomials, cosines, etc.). The main assumption is that we are mapping the rectangular grid of points X and Y onto a rectangular grid $\tilde{\mathsf{X}}$ and $\tilde{\mathsf{Y}}$, and hence can take advantage of matrix algebra. Thus, if B_x and B_y are respectively matrices of discrete orthonormal basis functions for the x- and y-directions, then the transformed coordinates can be modelled as,

$$\tilde{\mathsf{X}} = \mathsf{B}_y \mathsf{S}_{\tilde{x}} \mathsf{B}_x^{\mathrm{T}} \quad \text{and} \quad \tilde{\mathsf{Y}} = \mathsf{B}_y \mathsf{S}_{\tilde{y}} \mathsf{B}_x^{\mathrm{T}}. \tag{3.34}$$

where $\mathsf{S}_{\tilde{x}}$ and $\mathsf{S}_{\tilde{y}}$ are the respective spectra of the image coordinates with respect to the particular basis functions. Since the image coordinate are corrupted by noise, we use a truncated set of basis functions (e.g., polynomials up to degree d_x and d_y). The approximated (i.e., calibrated) image coordinates are then obtained by a least-squares minimization, yielding,

$$\tilde{\mathsf{X}}_c = \mathsf{B}_y \mathsf{B}_y^{\mathrm{T}} \tilde{\mathsf{X}} \mathsf{B}_x \mathsf{B}_x^{\mathrm{T}} \tag{3.35}$$

$$\tilde{\mathsf{Y}}_c = \mathsf{B}_y \mathsf{B}_y^{\mathrm{T}} \tilde{\mathsf{Y}} \mathsf{B}_x \mathsf{B}_x^{\mathrm{T}}. \tag{3.36}$$

For example, by using only polynomials up to degree two in each direction, we would then be calibrating the transformation in Eq. (3.33) such that it is purely biquadratic. The correspondence between the real-world coordinates X and Y and the calibrated image coordinates $\tilde{\mathsf{X}}_c$ and $\tilde{\mathsf{Y}}_c$, i.e.,

$$\mathsf{X} \leftrightarrow \tilde{\mathsf{X}}_c \tag{3.37}$$

$$\mathsf{Y} \leftrightarrow \tilde{\mathsf{Y}}_c \tag{3.38}$$

is then a correspondence of matrix indices. That is the real world point $(x_{ij}, y_{ij}) = (\mathsf{X}(i,j), \mathsf{Y}(i,j))$ corresponds to the calibrated point $(\tilde{\mathsf{X}}_c(i,j), \tilde{\mathsf{Y}}_c(i,j))$, see Fig. 3.18.

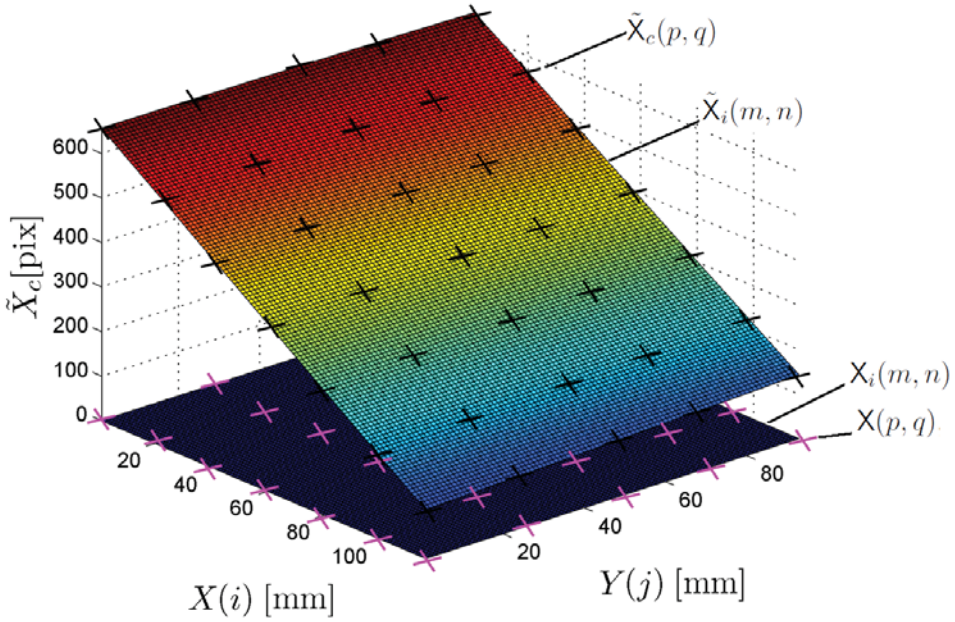

Fig. 3.18: Coordinate transformation $\mathsf{X}(p,q) \leftrightarrow \tilde{\mathsf{X}}_c(p,q)$ of the calibration points (LEDs) in Fig. 3.13. The calibrated and known 7×5 sub-grid of LED positions $\tilde{\mathsf{X}}_c(p,q)$ is interpolated over the complete grid $\tilde{\mathsf{X}}_i(m,n)$

3.5.5 Grid Interpolation

The laser point must be identified in the image, in general, at points which don't correspond to calibration points. We must therefore interpolate the calibrated grid to a higher resolution to identify points between the calibration points. Assuming that we have $p \times q$ matrices of calibrated points, the interpolated calibration matrices are $m \times n$ matrices, where $m > p$, and $n > q$. Thus let $\mathsf{B}_{\tilde{x}}$ and $\mathsf{B}_{\tilde{y}}$ be respectively $m \times (d_x + 1)$ and $n \times (d_y + 1)$ matrices of basis functions, of the same type(s) as B_x and B_y. The interpolated calibration grid is then,

$$\tilde{\mathsf{X}}_i = \mathsf{B}_{\tilde{y}} \hat{\mathsf{B}}_{\tilde{y}}^{+} \tilde{\mathsf{X}}_c \left(\hat{\mathsf{B}}_{\tilde{x}}^{+} \right)^{\mathrm{T}} \mathsf{B}_{\tilde{x}}^{\mathrm{T}} \tag{3.39}$$

$$\tilde{\mathsf{Y}}_i = \mathsf{B}_{\tilde{y}} \hat{\mathsf{B}}_{\tilde{y}}^{+} \tilde{\mathsf{Y}}_c \left(\hat{\mathsf{B}}_{\tilde{x}}^{+} \right)^{\mathrm{T}} \mathsf{B}_{\tilde{x}}^{\mathrm{T}}. \tag{3.40}$$

where the matrices,

$$\hat{\mathsf{B}}_{\tilde{x}} = \mathsf{B}_{\tilde{x}} \left(\boldsymbol{u}, 1 : d_y + 1 \right) \tag{3.41}$$

$$\hat{\mathsf{B}}_{\tilde{y}} = \mathsf{B}_{\tilde{x}} \left(\boldsymbol{v}, 1 : d_y + 1 \right) \tag{3.42}$$

are sub-matrices of $\mathsf{B}_{\tilde{x}}$ and $\mathsf{B}_{\tilde{y}}$ indexed at the set of indices $\boldsymbol{u}$ and $\boldsymbol{v}$ which are to correspond to the original calibration points.

3.5.6 Covariance Propagation

Given a perturbed signal $\boldsymbol{y}$ with independent and identically distributed (i.i.d.) Gaussian noise the covariance of $\boldsymbol{y}$ is,

$$\Lambda_{\boldsymbol{y}} = \mathrm{diag}\{\sigma^2, \ldots, \sigma^2\} \tag{3.43}$$
$$= \sigma^2 \mathsf{I}_m \tag{3.44}$$

where I_m is a $m \times m$ identity matrix. Applying the linear transformation L to $\boldsymbol{y}$

$$\boldsymbol{z} = \mathsf{L}\boldsymbol{y} \tag{3.45}$$

yields the vector $\boldsymbol{z}$. The noise in $\boldsymbol{z}$ is also Gaussian since it is generated from a linear combination of $\boldsymbol{y}$. The covariance of $\boldsymbol{z}$ is consequently,

$$\Lambda_{\boldsymbol{z}} = \frac{\partial \boldsymbol{z}}{\partial \boldsymbol{y}} \Lambda_{\boldsymbol{y}} \left(\frac{\partial \boldsymbol{z}}{\partial \boldsymbol{y}} \right)^T \tag{3.46}$$

where $\frac{\partial \boldsymbol{z}}{\partial \boldsymbol{y}}$ is the Jacobian of $\boldsymbol{z}$ with respect to $\boldsymbol{y}$ and therefore can be expressed as

$$\frac{\partial \boldsymbol{z}}{\partial \boldsymbol{y}} = \mathsf{L}. \tag{3.47}$$

Substituting this result int Eq. 3.46 yields

$$\Lambda_{\boldsymbol{z}} = \mathsf{L}\Lambda_{\boldsymbol{y}}\mathsf{L}^T = \sigma^2 \mathsf{L}\mathsf{L}^T. \tag{3.48}$$

To compute the covariance of the calibration points, we vectorize Eq. (3.34), yielding,

$$\mathrm{vec}\left(\tilde{\mathsf{X}}\right) = \left(\mathsf{B}_x \otimes \mathsf{B}_y\right) \mathrm{vec}\left(\mathsf{S}_x\right), \tag{3.49}$$

where $\otimes$ is the Kronecker [31] product describing now a linear transformation of the form $\boldsymbol{z} = \mathsf{L}\boldsymbol{y}$. Since, the basis functions are orthonormal, the corresponding vectorized spectrum is,

$$\mathrm{vec}\left(\mathsf{S}_x\right) = \left(\mathsf{B}_x^{\mathrm{T}} \otimes \mathsf{B}_y^{\mathrm{T}}\right) \mathrm{vec}\left(\tilde{\mathsf{X}}\right) \tag{3.50}$$

Therefore, the covariance of the vectorized spectrum, by Eq. (3.48), is given as,

$$\Lambda_{\mathrm{vec}(\mathsf{S}_x)} = \left(\mathsf{B}_x^{\mathrm{T}} \otimes \mathsf{B}_y^{\mathrm{T}}\right) \Lambda_{\mathrm{vec}\left(\tilde{\mathsf{X}}\right)} \left(\mathsf{B}_x \otimes \mathsf{B}_y\right) \tag{3.51}$$

If we assume that the identified calibration points are corrupted by i.i.d. Gaussian noise, i.e., $\Lambda_{\mathrm{vec}\left(\tilde{\mathsf{X}}\right)} = \sigma^2 \mathsf{I}_{pq}$, then the covariance of the vectorized spectrum is,

$$\begin{aligned} \Lambda_{\mathrm{vec}(\mathsf{S}_x)} &= \sigma^2 \left(\mathsf{B}_x^{\mathrm{T}} \otimes \mathsf{B}_y^{\mathrm{T}}\right) \mathsf{I}_{pq} \left(\mathsf{B}_x \otimes \mathsf{B}_y\right) \\ &= \sigma^2 \left(\mathsf{B}_x^{\mathrm{T}}\mathsf{B}_x \otimes \mathsf{B}_y^{\mathrm{T}}\mathsf{B}_y\right) = \sigma^2 \mathsf{I}_{pq} \end{aligned} \tag{3.52}$$

That is, the corresponding noise in the spectrum is also i.i.d. Gaussian, due to the fact that the basis functions are orthonormal. By a derivation along the same lines, we vectorize Eq.(3.35) and yield the covariance of the calibrated coordinates as,

$$\Lambda_{\mathrm{vec}\left(\tilde{\mathsf{x}}_c\right)} = \left(\mathsf{B}_x\mathsf{B}_x^{\mathrm{T}} \otimes \mathsf{B}_y\mathsf{B}_y^{\mathrm{T}}\right) \Lambda_{\mathrm{vec}\left(\tilde{\mathsf{x}}\right)} \left(\mathsf{B}_x\mathsf{B}_x^{\mathrm{T}} \otimes \mathsf{B}_y\mathsf{B}_y^{\mathrm{T}}\right). \tag{3.53}$$

The derivation of $\Lambda_{\mathrm{vec}(\tilde{\mathsf{Y}}_c)}$ is identical, whereby this assumes that the noise in $\tilde{\mathsf{X}}$ and $\tilde{\mathsf{Y}}$ are independent. If the noise is not independent, the overall covariance can be obtained by stacking the vectorized equations. A higher degree yields a lower systematic error but a higher statistical error. The covariance propagation is used to determine which degree polynomial approximation yields the best balance between statistical and systematic errors. The covariance propagation has been verified via Monte Carlo simulations. Figure 3.20 shows the covariance propagation matrix $\Lambda_{\mathrm{vec}(\tilde{\mathsf{X}}_c)}$ applied to calibration points lying on a 5×7 regular grid similar to the LED grid of the calibration image. The x-coordinate of the calibration points are perturbed with $\sigma = 1$. A higher degree yields a higher "noise gain" and, therefore, yields a covariance matrix with higher magnitude entries. The diagonal element entries of the matrix denote the variances of each node of the grid. The nodes are stacked column-wise as we vectorized the equations.

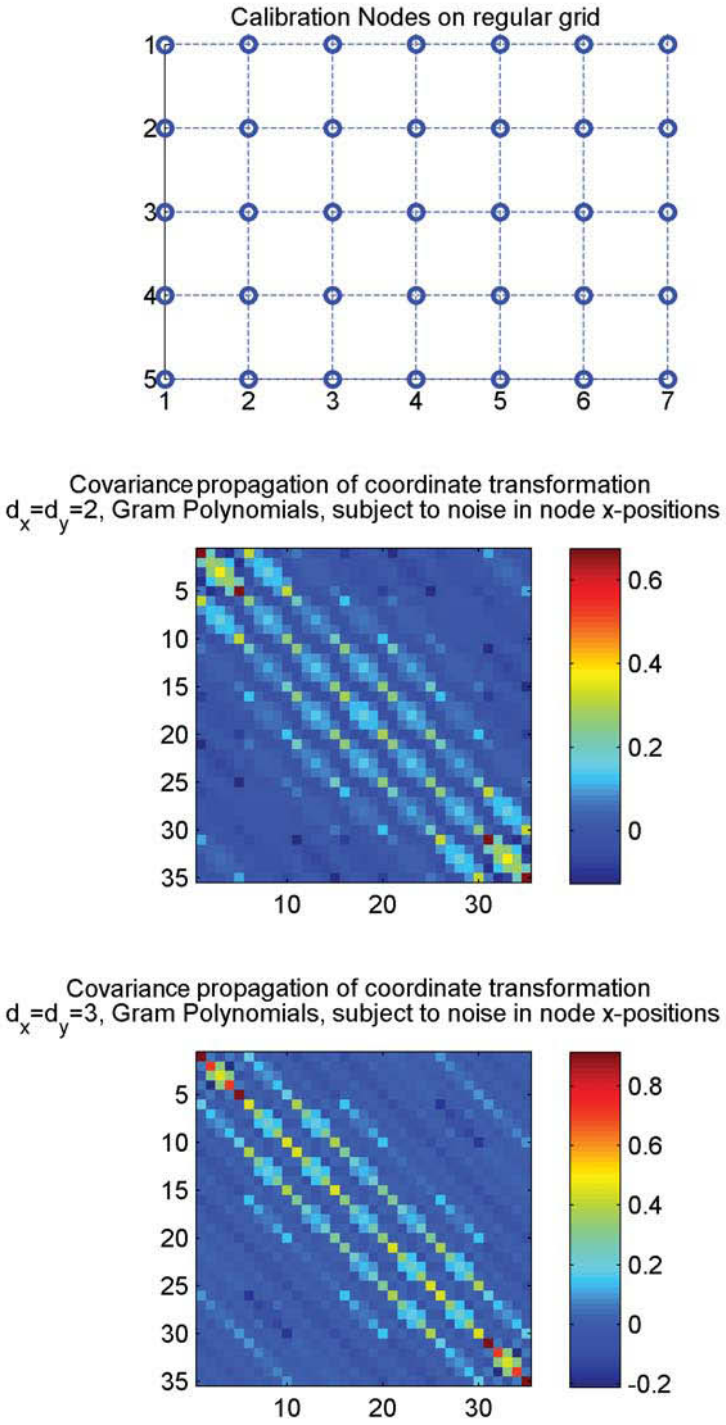

Fig. 3.19: Example of the covariance matrix $\Lambda_{\mathrm{vec}(\tilde{\mathsf{X}}_c)}$ associated with a degree, $d_x = d_y = 2$ (middle) and $d_x = d_y = 3$ (bottom), Gram polynomial approximation of calibration points $\tilde{\mathsf{X}}_c$ lying on a 5×7 regular grid that are perturbed with $\sigma = 1$. The diagonal element entries of the matrix denote the variances of each node of the grid where the nodes are stacked column-wise due to vectorization.

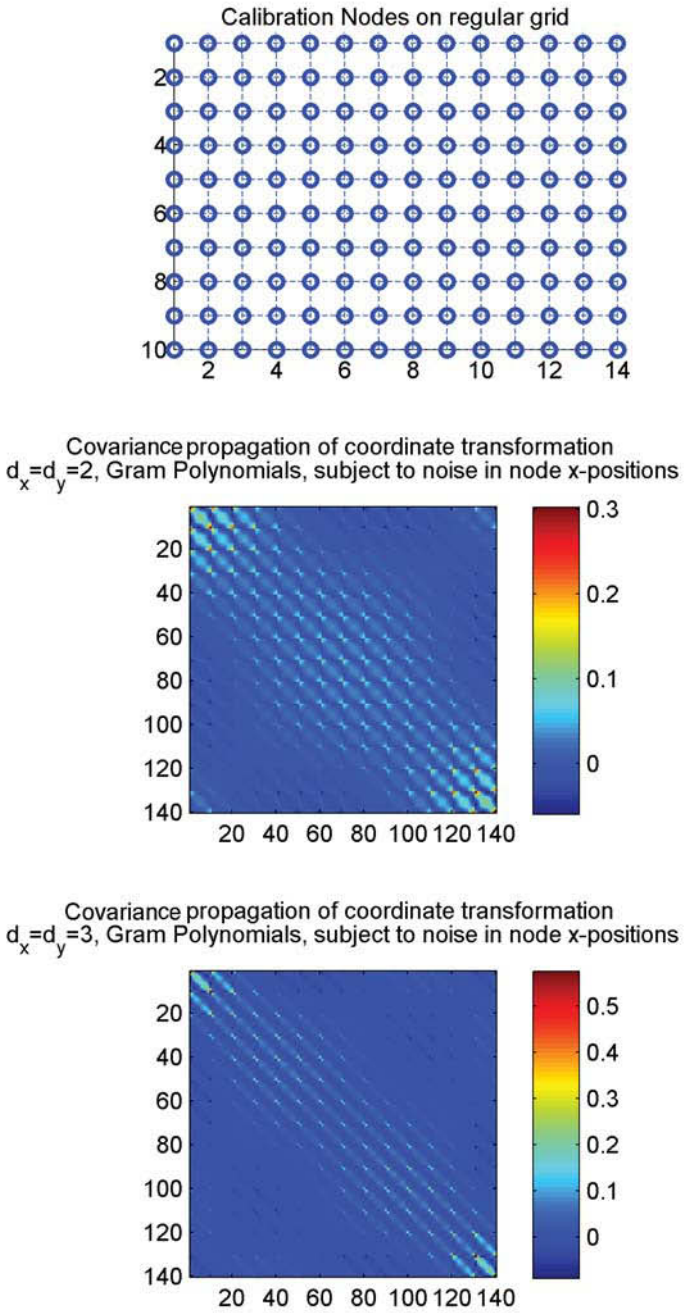

Fig. 3.20: Example of the covariance matrix $\Lambda_{\mathrm{vec}(\tilde{\mathsf{X}}_c)}$ associated with a degree, $d_x = d_y = 2$ (middle) and $d_x = d_y = 3$ (bottom), Gram polynomial approximation of calibration points $\tilde{\mathsf{X}}_c$ lying on a 10×14 regular grid that are perturbed with $\sigma = 1$. The diagonal element entries of the matrix denote the variances of each node of the grid where the nodes are stacked column-wise due to vectorization.

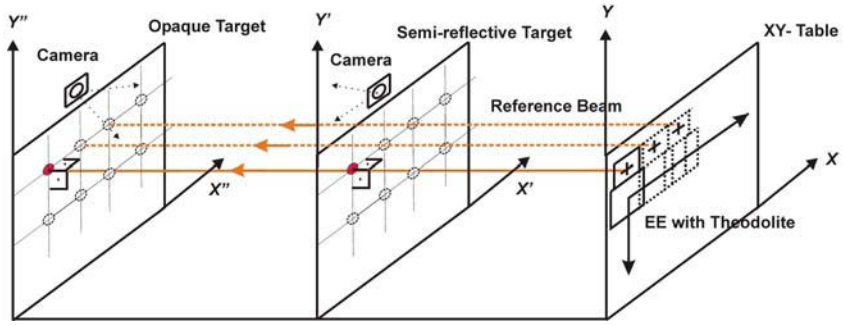

Fig. 3.21: Principle of operation of complete input-output system calibration: Scanning the targets where the targets and xy-table are plane-parallel and the laser beam following on orthogonal is perpendicular to the targets.

3.5.7 System Calibration Procedure of the ALT unit

The principle of calibration of this unit is to use the reference laser (theodolite) which is mounted on a xy-table, see Fig. 3.6. The laser beam is normal to the target plane whereas the xy-table motion is parallel to the targets. Hence, the position of the laser source on the End Effector EE (position read from the actuators input data) is the position of the laser spots on the targets in real world coordinates. The EE follows then an orthogonal grid of positions (scanning) where at each position snapshots of the laser spots are taken. The result of this scan is an orthogonal array of laser spots, similar to the LED array on the calibration plate, to compute the transformation. The advantage of this method is obvious as the whole chain of measurement components is calibrated. The results of the scans are shown in Fig. 3.22 and Fig. 3.23 where the laser was moved to follow an orthogonal grid of 25 [mm] in x and y-directions. Note that when using band-pass filters the laser spot's intensity in the image is dependent on the angle of incidence to the camera. This effect can be significantly noticeable in the scan of the semi-reflective target. This measurement indicates that there may be some room for improvement by optimizing the dot-pattern to achieve a higher reflective portion. Nevertheless reproducibility tests show that extraction of the positions of the laser midpoint is very robust with only sub-pixel deviation providing a data set of calibration points of high confidence for coordinate transformation, see Fig. 3.24 and Fig. 3.24. The average positional re-mapping error of the laser spots is $\bar{e}_s < 0.08$ [mm]. The results are summarized in Table 3.4.

Target	Grid	STD of Positional Reproducibility laser spot mid-points	Average (e_i) Positional Error of re-mapped laser spots	STD (e_i) Positional Error of re-mapped laser spots
Semi-Transparent	6×5	$\sigma_{x,s} = 0.0747$ [pix] $\sigma_{y,s} = 0.0678$ [pix]	$\bar{e}_s = 0.0714$ [mm]	$\sigma_s = 0.0359$ [mm]
Opaque	6×5	$\sigma_{x,o} = 0.0595$ [pix] $\sigma_{y,o} = 0.0697$ [pix]	$\bar{e}_s = 0.0458$ [mm]	$\sigma_o = 0.0254$ [mm]

Table 3.3: Reproducibility tests of extracted positions of laser spots and evaluation of accuracy of the coordinate transformation method employing bivariate polynomial tensor approximation. The extracted positions of the spots in the image are re-mapped to their real world coordinates to compute the positional error e_i subject to the pre-known positions of laser spots $e_i = \sqrt{\Delta x^2 + \Delta y^2}$. (Bivariate tensor polynomial approximation with Gram basis functions of degree $d_x = d_y = 3$), see Fig. 3.24.

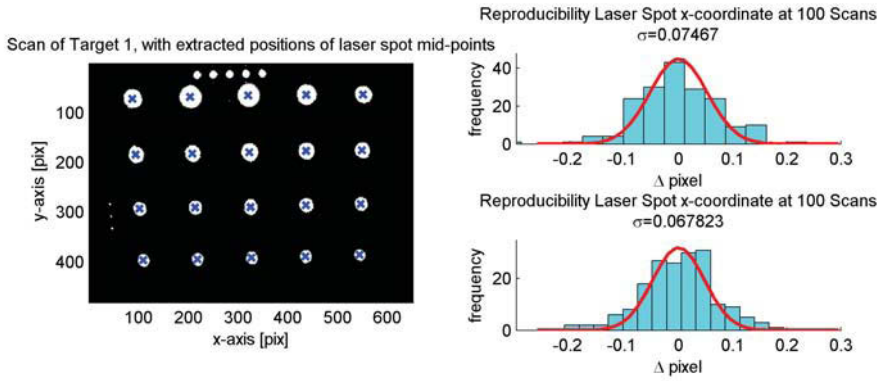

Figure 3.22: Scan on semi-reflective target and distribution of reproducibility measurements estimating the positions of laser spots in image.

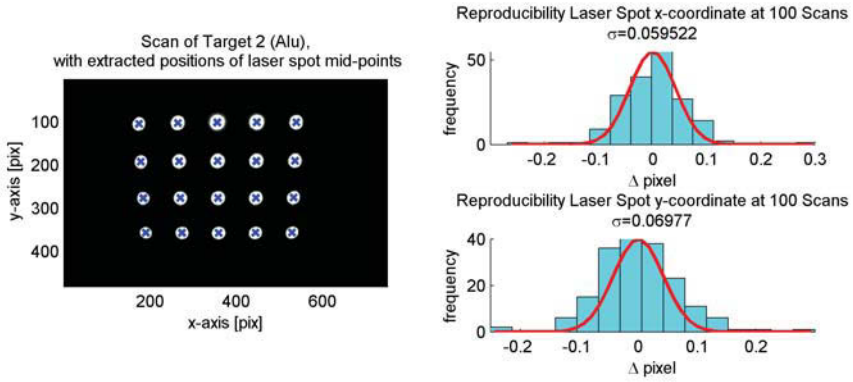

Figure 3.23: Scan on opaque target and distribution of reproducibility measurements estimating the positions of laser spots in image.

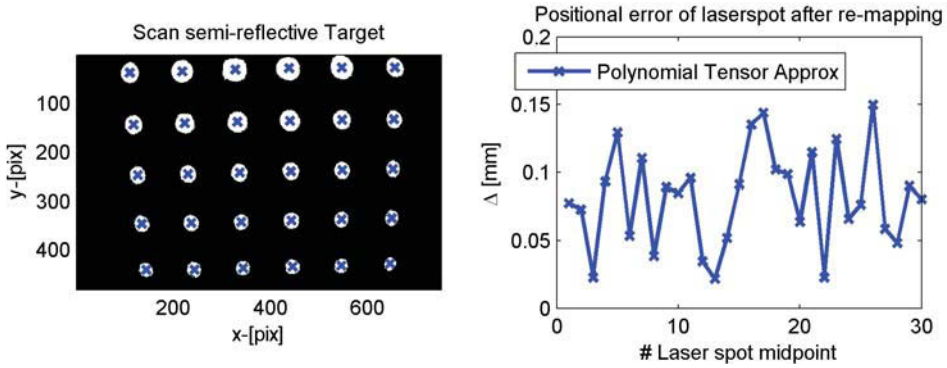

Figure 3.24: Scan on semi-reflective target showing a regular grid of 6×5 laser spots. The image (left) is taken with a micro lens $f = 8$ [mm] at a distance of 280 [mm]. The extracted positions of the spots in the image are re-mapped to their real world coordinates to compute the positional error e_i subject to the pre-known positions of laser spots $e_i = \sqrt{\Delta x^2 + \Delta y^2}$, (right). (Bivariate tensor polynomial approximation with Gram basis functions of degree $d_x = d_y = 3$.)

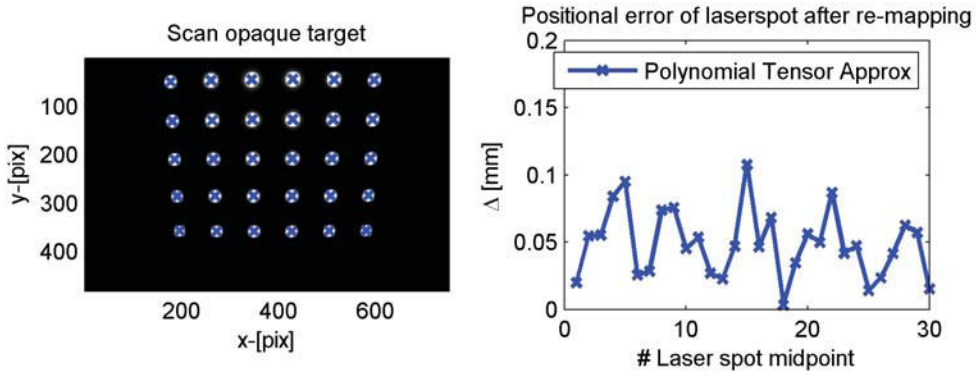

Figure 3.25: Scan on opaque target showing a regular grid of 6×5 laser spots. The image (left) is taken with a micro lens f=5.7 [mm] at a distance of 280 [mm]. The extracted positions of the spots in the image are re-mapped to their real world coordinates to compute the positional error e_i subject to the pre-known positions of laser spots $e_i = \sqrt{\Delta x^2 + \Delta y^2}$, (right). (Bivariate tensor polynomial approximation with Gram basis functions of degree $d_x = d_y = 3$).

3.6 Testing the Complete Device

A series of 70 measurements was performed over a grid of points which span the full area of the target (Fig. 3.26), the reference laser was given a different yaw and pitch for each measurement. An angle reproducibility of $\sigma_{(Y,r)} \approx 0.001$ [degree] and an accuracy of $\sigma_{(Y,a)} \approx 0.02$ [degree] was achieved. Principle Component Analysis (PCA) was performed for each of pitch and yaw to determine if the results are truly independent. The PCA for yaw and pitch are shown in Fig. 3.28 and Fig. 3.29 there is a minor correlation between the axes. It is below the required measurement accuracy, but justifies further investigation. The results are summarized in Table 3.4.

Angle	STD Angle Reproducibility	STD Angle Accuracy
Yaw	$\sigma_{(Y,r)} = 0.00113$ [degree]	$\sigma_{(Y,a)} = 0.0226$ [degree]
Pitch	$\sigma_{(P,r)} = 0.00084$ [degree]	$\sigma_{(P,a)} = 0.0183$ [degree]

Table 3.4: Reproducibility tests of extracted positions of laser spots.

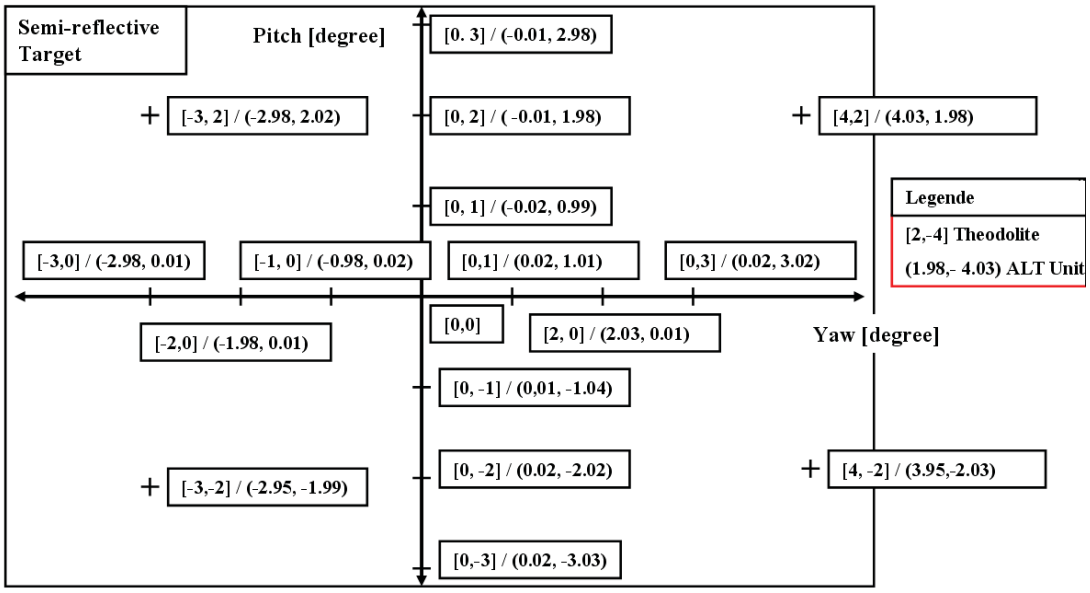

Figure 3.26: Raw data sample [degree], angle accuracy measurements over a grid of points which span the full area of the semi-reflective target.

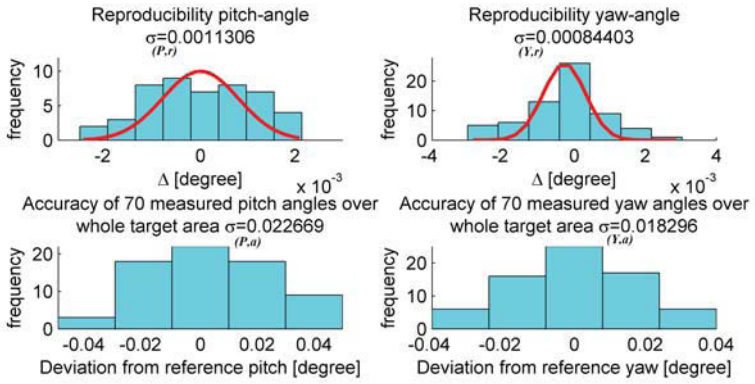

Figure 3.27: Accuracy and Reproducibility of pitch and yaw of 70 measurements performed over a grid of points which span the full area of the target.

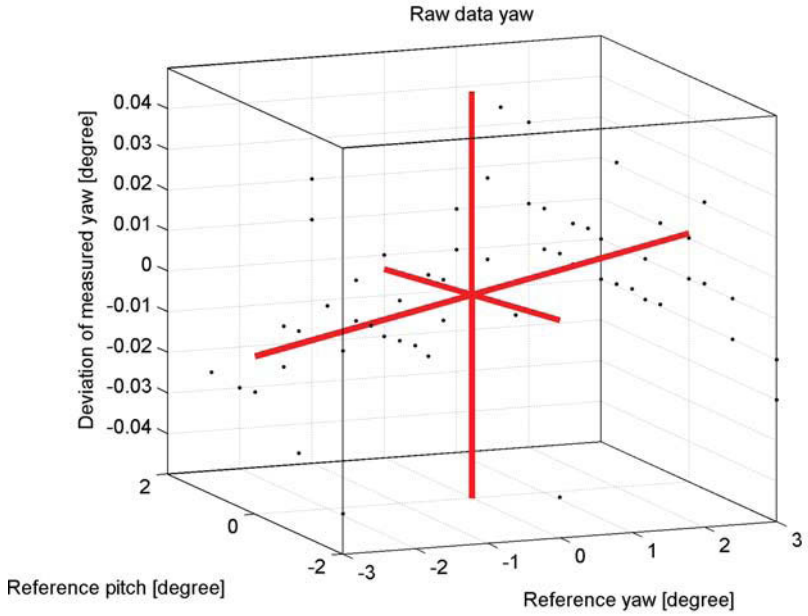

Figure 3.28: Principle component analysis of the error in yaw with respect to yaw and pitch. Note the axes are not exactly perpendicular.

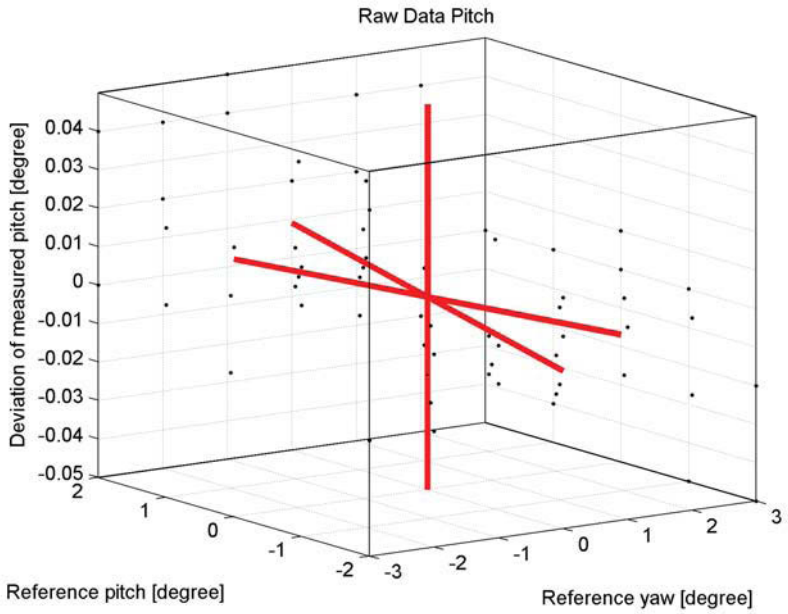

Figure 3.29: Principle component analysis of the error in pitch with respect to yaw and pitch. Note the axes are not exactly perpendicular.

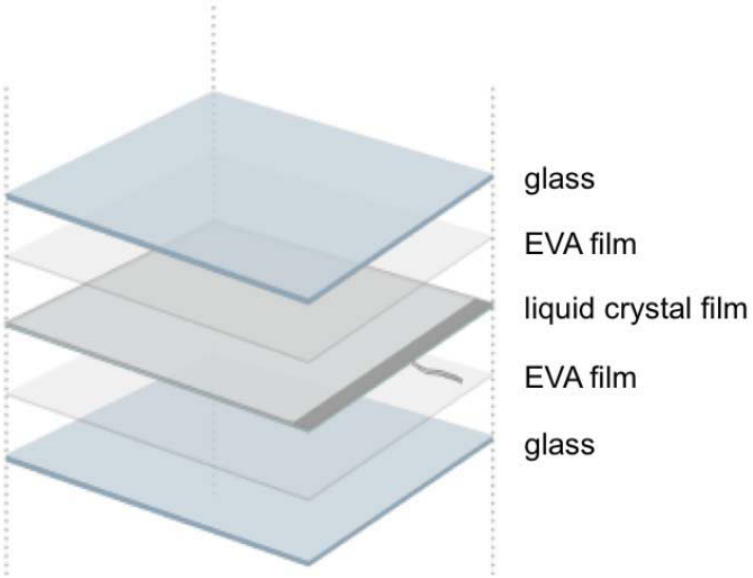

Figure 4.1: Layer design of the Saint Gobain *SGG PrivaLite4* electro-active glass.

Chapter 4

Electro-Active Glass Target

Electro-active glass has gained popularity in architecture applications, e.g., glass facades to control sunlight transmission. During the investigation for a suitable target with semi-reflective/transparent properties for the ALT unit it was found that this technology has interesting features as regards camera based metrology. As the transmission property can be controlled from transparent to opaque it allows placement of several targets in a row to measure displacements at different locations with a single reference beam without significant loss of the laser's intensity. The principle of operation of electro-active glass is shown in Fig. 2.3.1. The product [21] consists of two sheets of optical glass encapsulating a liquid crystal film sandwiched between two ethylene vinyl acetate (EVA) interlayer films. This layer consists of two sheets of polyethylene terephtalate (PET) films coated with a transparent metallic deposit and laminated together with a very fine layer of liquid crystal gel. Applying alternating current of 100 [V] by lateral copper electrodes, the liquid crystals orient themselves in the same direction; the initially milky film is instantly transparent.

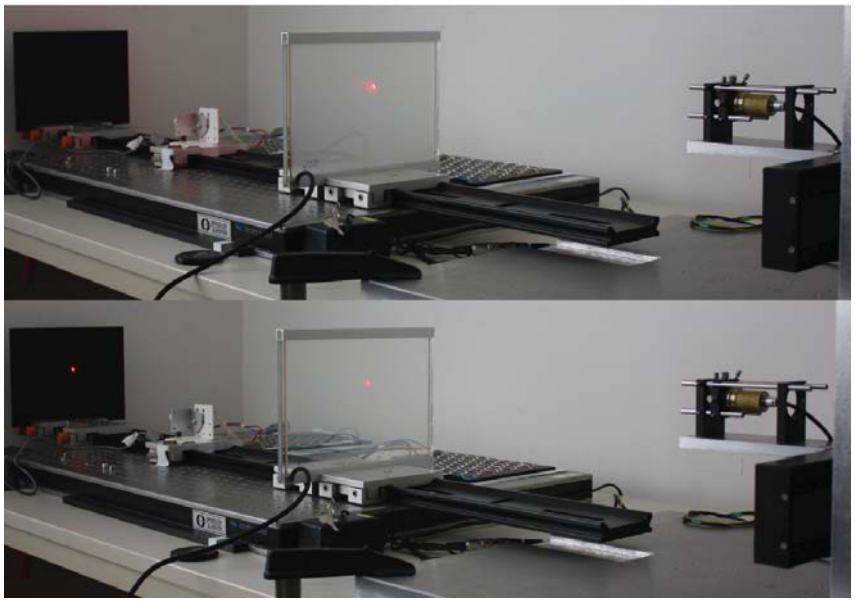

Figure 4.2: Laboratory setup using *SGG PrivaLite4* [21] glass in opaque mode and transparent mode. Note the laser spots on the targets mapped by the reference laser beam.

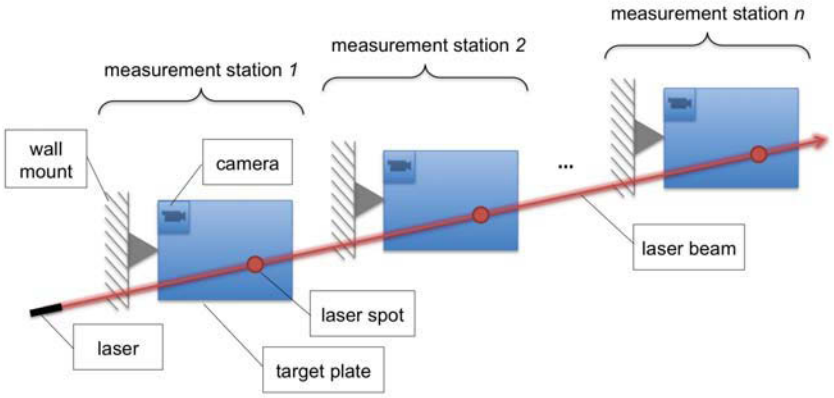

Figure 4.3: Feasible application of electro-active glass to monitor creeping rock-movement displacements at different locations in, e.g., a tunnel.

An attractive potential application for these targets might be, e.g., in mine surveying to monitor creeping rock-movements. The principle of operation of this application is shown in Fig. 4.2 and Fig. 4.3 where several targets are installed in a row at different location and rigidly fixed to the rock. There is a camera for each target to monitor the laser spot of the reference beam. Displacement analysis becomes therefore selective regarding location. Such systems are a viable alternative to plummet-based measurements as described and applied in [16].

Chapter 5

Conclusions and Future Work

The combination of the proposed optical components with a new mathematical model and calibration procedure have enabled the implementation of a robust optical measurement device. The standard deviation of the displacement error is $\sigma_{d3} = 0.04937$ [mm] and for yaw and pitch $\sigma_{(\phi,a)} < 0.023$ [degree]. The use of a bivariate polynomial tensor as an input-output model enables the computation of covariance propagation of the transformation. This has been used to optimize the parameterization of the system. The new calibration procedure compensates for the projection associated with relative positioning of the camera and also corrects the distortion of the optical components. In this manner the accuracy of the measurement system is no longer limited by the accuracy of the individual optical components. This enables the use of optical components with a higher degree of distortion, as long as they are stable. The advantages associated with the use of the short focal lenses, despite their high distortion, are two fold: the shorter focal length permits a more compact construction of the device for a given field of view; lenses with a higher distortion are in general cheaper, this gives a commercial advantage without sacrificing measurement accuracy.
The algorithm and methods for calibration and measurement were programmed entirely in Matlab®. Stand-alone software has been implemented to be field portable.

Future Work

1. There is still some room for improvement to optimize the semi-transparent target subject to visibility of the laser spot and statistical estimation of the position of the laser spot. Reproducibility tests showed that the displacements measurements on the corresponding opaque target are twice as accurate as on the employed semi-transparent target. Optimizing the dot-pattern by decreasing the dot-diameter and dot-distance might provide improvement. An alternative, that should be investigated, is the implementation of electro-active glass as a new target component. The target is switched in opaque mode to estimate the position on the front target and then switched in transparent mode to measure the position on the rear target.

2. The system calibration is performed on a provisional laboratory setup. The calibration results depend strongly on the adjustment accuracy of the laser beam and

xy-table relative to the measurement unit. A customized calibration table where xy-table with theodolite and the measurement unit might be installed precisely for better alignment is planned. The theodolite might be adjusted with corner cube prism reflectors.

3. The measurement results of position of the laser spots and the resulting pitch and yaw angles are obtained in a laboratory environment. Tests under vibrations have not been performed yet. However, estimation of the laser spots positions is computed by processing up to 20 frames per seconds where the average value is taken. It is believed that this is sufficient to filter vibration influences.

4. Laser spots' intensity and quality were evaluated in laboratory environment and at distances up to 20 metres. Influences on the laser beam subject to dust and long range have to be investigated.

References

[1] S. Matsui, C. Zhang, "Alignment method for 50m distance using laser and CCD camera", *Proceedings of the 7th International Workshop*, Japan, 2002

[2] A. Soetegjo, E. Nurcahyo, "Developing of low cost vision-based shooting range simulator", *International Journal of Computer Science and Network Security*, Vol.11, 2011.

[3] G. Retscher, "Multi-sensor systems for machine guidance and control", *International Federation of Surveyors, (FIG) International Congress XXII*, Washington DC, USA, 2002.

[4] J. Allen, "Laser beam rider guidance system", Patent: US 4 111 385, 1978.

[5] M. Herrenknecht, "Laser-controlled machines for microtunneling", *Proceedings of the 8th ISARC*, Germany, pp. 789-800, 1991.

[6] Leica Geosystems, "Product: TPS1200+, Technical Specification", 2011, [Online]. Available: http://www.leica-geosystems.com

[7] K. Hu, "Visual pattern recognition by moment invariants", *IRE Trans. Info. Theory*, Vol. IT-8, pp.179-187, 1962

[8] R. Neumayr, "Camera-aided robot calibration of the planar double-triangular parallel manipulator", Diplomarbeit, Institute for Automation, Montanuniversität Leoben, Austria, 2004.

[9] M. Tratnig, "Calibration and registration approaches for light-sectioning setups featuring small fields of view", Doctoral Thesis, Institute for Automation, Montanuniversität Leoben, Austria, 2005.

[10] P. O'Leary, M. Harker, "Surface modeling using discrete basis functions for real-time automatic inspection", Manuscript, Institute for Automation, Montanuniversität Leoben, Austria, 2010.

[11] Geodata Group GmbH, "Prototype Active Laser Target Unit", http://www. geodata.com, 2011

[12] VMT GmbH Gesellschaft für Vermessungstechnik, "Datenblatt, Altu System", 2011, [Online]. Available: http:// vmt-gmbh.de/fileadmin/be _user/Downloads /VMT_LD_DT_A4.pdf.

[13] tacs gmbh, “acs guidance system, Datenbaltt”, 2011, [Online]. Available: http://www.tacsgmbh.de/en/tacs_prod_videotargets.htm, acs guidance system.

[14] M. Filipowski, S. R. Wardwell and M.L. Shank, “Guidance system and method for keeping a tunnel boring machine continously on a plan line”, Patent: US 5 529 437, 1996

[15] Palfinger Precision Systems, “PPS TBM Guidance System, Data Sheet”, Simbacherstr. 127, D-944405 Landau.

[16] Huggenberger AG, “Datenblatt GL Gewichtslot”, 2011, [Online]. Available: http://www.huggenberger .com/uploads/media/ Huggenberger_GL_de.pdf.

[17] Hartley, R., Zisserman, *Multiple View Geometry in Computer Vision*, 2nd Edition, Cambridge University Press, 2003.

[18] J. Gram, “Über die Entwicklung realler Funktionen in Reihen mittelst der Methode der kleinsten Quadrate”, *Journal für die reine und angewandte Mathematik*, pp. 150–157, 1883

[19] M. Eden, M. Unser and L. Leonardi, “Polynomial representaion of pictures“, *Signal Processing*, Vol. 10, pp. 385-393, 1986.

[20] VR-Magic Holding AG, “Multi-Sensor-Cameras Datenblatt”, 2011, [Online]. Available: http://www.vrmagic.com/fileadmin/downloads/imaging/ Brochures/VR-magic_Multisensor_Cameras.pdf.

[21] Saint-Gobain Glass, “Priva-Lite Datenblatt”, 2011, [Online]. Available: http://www.quantumglass.com/de/ download-solutions2.php? type=quantumglass&leaflet=1.

[22] Du Pont Advanced Fiber Systems, “KEVLAR, technical data sheet”, 2011, [Online]. Available: http:// www2.dupont.com/Kevlar/

[23] M. Sonka, V. Hlavac, R. Boyle, *Image Processing Analysis and Machine Vision*, 2nd edition, PWS Publishing, 1999.

[24] M. Harker, P. O’Leary, “Computation of Homographies”, *British Machine Vision Conference*, Vol. 1, pp. 310–319, 2005.

[25] H. C. van Assen, M. Egmont-Petersen and J. H. C. Reiber, “Accurate object localization in gray level images using the center of gravity measure: accuracy versus precision”, *IEEE Transactions on Image Processing*,Vol. 11, pp. 1379–1384, 2002.

[26] *International Electrotechnical Commission Standard IEC*, , IEC 60529, Ingress Protection Rating - IP67.

[27] Herrenknecht AG,“TBM S-210”, 2011, [Online], Available: http://en. wikipedia. org/wiki/File: TBM _S-210 _Alptransit_Faido_East.jpg

[28] J. Golser and F. Reiss, "Produktentwicklung einer Active Laser Target Einheit", Technical Report, Institute for Automation, Montanuniversität Leoben, 2011.

[29] Leica Geosystems, "Product: TPS1200+, Technical Specification", 2011, [Online]. Available: http://www.leica-geosystems.com/ de/Leica-TPS1200_4547.htm

[30] P. Schalk, "Metric vision methods for material and product inspection", PhD Thesis, Institute for Automation, Montanuniversität Leoben, 2007.

[31] C. F. Van Loan, "The ubiquitous Kronecker product", *Journal of Computational and Applied Mathematics*, Vol.123, pp. 85-100, 2000.

[32] A. Goshtasby, "Image registration by local approximation methods", *Image and Vision Computing*, Vol. 6, pp. 255-261, 1988.

Author's Publications

Refereed Journal Articles

[33] R. Neumayr, P. J. Zsombor-Murray, P. O'Leary, "Precise pose measurement with single camera calibration for planar parallel manipulators", *CSME TRANSACTIONS*, Vol. 35, No. 2, pp. 201–213, 2011.

Conference Proceedings

[34] M. Harker, P. O'Leary, R. Neumayr,"Profile Measurement via Circle-Line Spline Fitting", *IEEE Instrumentation Measurement Technology Conference 2009*, Singapore, pp. 1490-1496, 2009.

[35] P. O'Leary, M. Harker, R. Neumayr, "Savitzky-Golay smoothing for multivariate cyclic measurement data", *IEEE Instrumentation Measurement Technology Conference 2010*, pp. 1585–1590, 2010.

Submitted Conference Papers

R. Neumayr, M. Harker, P. O'Leary,"New Approaches to Machine Vision Based Displacement Analysis", submitted to *I2MTC 2012*, Graz, Austria, 2011.

Unpublished Manuscripts

[36] R. Neumayr, P. J. Zsombor-Murray, "Workspace and singularity analysis of the planar double triangular parallel manipulator using kinematic mapping", Institute for Automation, Montanuniversität Leoben, Austria, 2011.

Appendix A

ALT Unit

A.1 Preliminary Specification

1.1) **Measurement Accuracy** • ± 1[mm] at an active measurement area of 140x110[mm] • Resolution: 0.1[mm] • Pitch: ±1[mm]/1000[mm] • Yaw: ±1[mm]/1000[mm] • Roll: ±1[mm]/1000[mm]
1.2) **Stray Light Resistance** • up to 1000[lux]
1.3) **Reference Laser** • Power: 1-5[mW] • Wave Length: 600-700[nm] • Contour of Spot: Ellipse, Circle, max Ø=15[mm]
1.4) **Status Indicators** • Data Transfer, Error, Power Source, OK

1.5) **Range of Operation**

- Storage Temperature: -30 to +70[°C]
- Operating Temperature: -10 to +60[°C]
- min Operating Target Area: 110x140[mm]
- max Range Yaw: ±110[mm/m]
- max Range Pitch: ±250 [mm/m]
- max Range Roll: ±250[mm/m]
- max Range Laser Beam: up to 100[m]
- min Operating Hours: 6000[h]

1.6) **Interface, Port Communication**

- RS232/RS484 and Ethernet

1.7) **Vibration**

- Shock-proof: 100[g] for max 500[ms]

1.8) **Dimensions, Weight**

- Housing (w/h/d): 160x120x350[mm], anodised Aluminum, Easy-Install-Mechanism
- Weight: max 10kg

1.9) **Power Source**

- 12-30[VDC], max 1[A]

1.10) **Protection Class**

- IP67 (DIN 40050)

A.2 Laboratory Setup I

.

Laboratory Setup I

(a) **2x Industry Cameras**

- Pulnix TM-6CN series
- Resolution: 768x576[pixel], 8-bit monochrome
- Cosmicar lenses, f=12.5[mm]
- Interference Filters
  - CW: 635[nm]
  - HW: 11[nm]
  - from Eureca Messtechnik, Prod.Nr: IF-635-11/80-50

(b) **Target 1**

- optical glass plate 200x250[mm], Edmund Optics, Prod.Nr: NT43-974
- glass printed with an orthogonal point matrix with point diameter 0.8[mm]
- printed by Fa. Heidenbauer, Graz using the screen printing technology

(c) **Target 2**

- anodized aluminum plate 200x250[mm]
- 6 flat-headed LED mounted on for camera calibration
  - CW: 640[nm]
  - HW: 20[nm]
  - from Kingbright, Prod.Nr: L-483

(d) **Laser on Linear Drive**

- Manufacturer: Schaefter, Kirchhoff, 13 LR-series
- CW: 635[nm], ±10[nm]
- Laserspot: 13x5[mm] at 1[mm] distance
- Linear Drive: Bernecker und Rainer, Acopos-series, Resolution: 6[μm]/revolution

A.3 Laboratory Setup II

Laboratory Setup II

(a) **2x VR-Magic Multisensor Cameras**

- Pixel-Synchronous Sensors, 1/3" Chip
- Resolution: 752 x 480 [pixel], RGB 32
- VR-Magic Micro lenses, f=8[mm] for target 1, f=5.7[mm] for target 2
- Interference Filters
  - CW: 650[nm]
  - HW: 15[nm]
  - Diameter: 11[mm]
  - from Eureca Messtechnik, IF-650-15/80-11

(b) **Target 1**

- optical glass plate, 110x130[mm], Edmund Optics, Prod.Nr: NT43-974
- glass printed with an hexagonal point matrix with point diameter 0.5[mm]
- printed by Fa. Heidenbauer, Graz using the screen-printing technology
- Distance to Target 2: 280[mm]

(c) **Target 2**

- anodized aluminum plate, 130x160[mm], with pattern of flat-headed LEDs (LED-distance=25[mm], LED-diameter=5[mm]) for camera calibration and reference measurements
  - CW: 650[nm]
  - HW: 20[nm]
  - from Kingbright, Prod.Nr: L-483

(d) **Laser**

- Leica Theodolite, TPS 1200 series
- Laser Modul CW: 650[nm], ±10[nm], 5[W]
- Laserspot: Diameter 12[mm] at 10[m] distance

(e) **XY-Table**

- Costumized xy-table, manufactured and installed by GEODATA to calibrate the system
- 2 x Linear Drives, Range: 0-300[mm], Stepper Motor, Company: ITK
- Resolution: 6 [μm] per step

(f) **Software**

- Matlab© 2009b
- VR-Magic SDK CamLab Ver: 3.13f

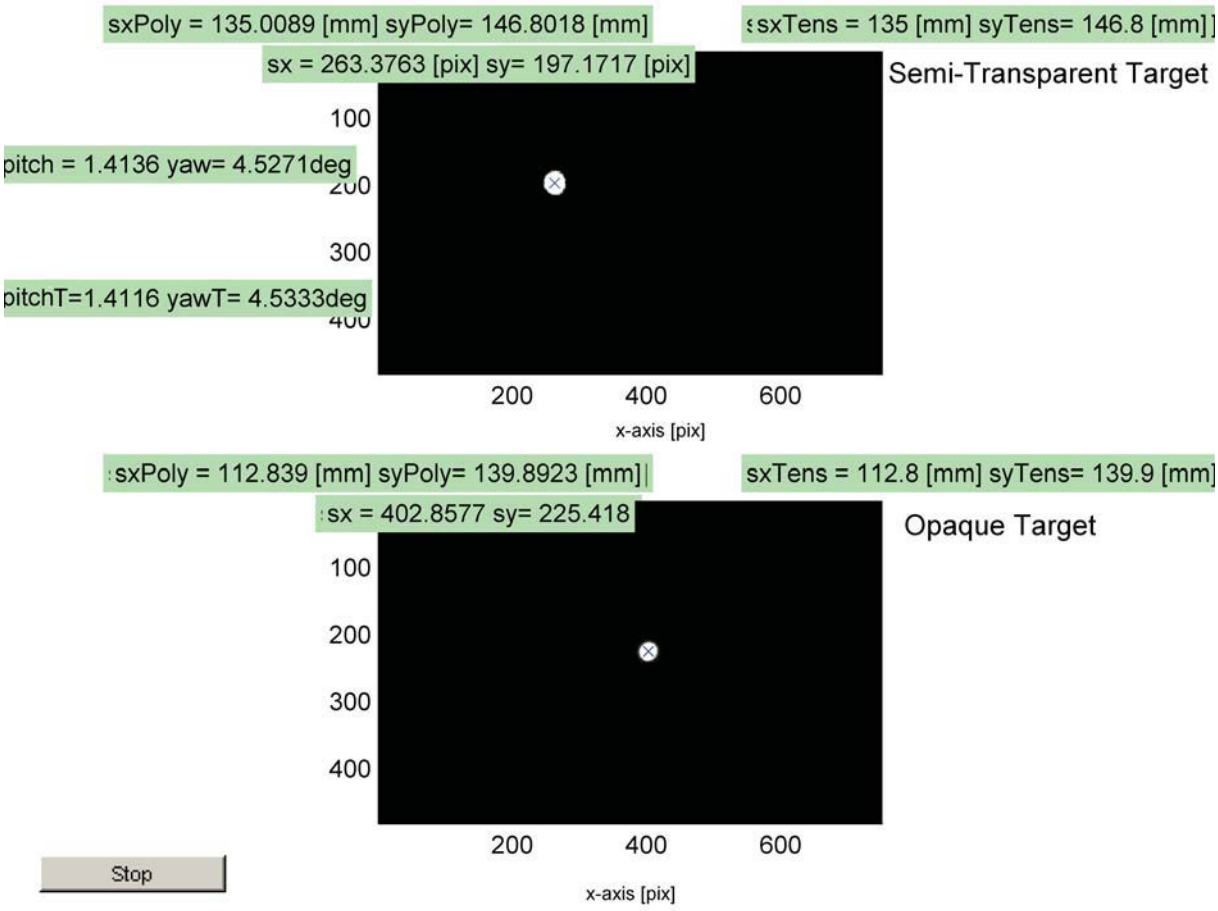

Figure A.1: Graphical User Interface of measurement software. Top: Acquired image of the semi-transparent target. Bottom: Acquired image of the opaque target. The position of the laser spot (sx, sy) is estimated in the image by first moment computation of intensities. The bivariate polynomial tensor approximation is employed to derive the real world coordinates of the spots, pitch and yaw (sxTens, syTens, pitchT, yawT). Note, a plausibility check for coordinate transformation was implemented using Matlab's mapping command "cp2tform". (sxPoly, syPoly, pitch, yaw).

A.4 Software Structure

The measurement software is entirely programmed in Matlab. The VR-Magic camera application software provides Matlab drivers so that:

1. Image acquisition (camera control, camera settings);
2. Image processing (feature extraction, laser spot position estimation, angle computation);
3. Display measurement results and save them in a data file;

can be performed with Matlab®. A screen shot of the GUI is shown in Fig. A.1 where the variables have the following meaning: The position estimation of the laser spot (sx, sy) is optional and can be computed in the image by first moment computation of intensities or ellipse fitting, see Section 2.1.1. As the image quality of the laser spots are, in this application, of high quality both methods yield the same results with position deviations of $\sigma \approx 0.01$ [pix]. The variables sxTens, syTens, pitchT, yawT denote the computed real world positions of the spots and the resulting orientation angles using the bivariate polynomial tensor approximation approach. Note, a plausibility check for coordinate transformation was implemented using Matlab's mapping command `cp2tform` for computing sxPoly, syPoly, pitch, yaw. This transformation method is based on the algorithm described in [32] where least square approximation of polynomial functions of x and y determine the mapping. However, Matlab® uses the Vandermonde matrix up to degree 4, $\sum_{i=1}^{n} c_n x^n$ that is poorly conditioned and quickly becomes degenerate as the degree of the polynomial increases. This method is sufficient when processing images acquired with a micro-lens with $f > 5.7$ [mm]. However, tests with images acquired with lenses of $f < 5.7$ [mm] show significant degradation in mapping whereas the bivariate polynomial tensor approximation approach still fulfills the required accuracy.
Up to 20 frames per second and per camera can be acquired to suppress vibrations influences caused by the machine.
A stand alone application of this software was compiled using the Matlab® command `deploytool`.